INTEGRATED NONLINEAR OPTICS IN SILICON NITRIDE WAVEGUIDES AND RESONATORS

A Dissertation

Presented to the Faculty of the Graduate School

of Cornell University

in Partial Fulfillment of the Requirements for the Degree of

Doctor of Philosophy

by

Jacob Samuel Levy

August 2011

INTEGRATED NONLINEAR OPTICS IN SILICON NITRIDE WAVEGUIDES AND RESONATORS

Jacob Samuel Levy, Ph.D.

Cornell University 2011

The emerging field of silicon photonics enables the fabrication of on-chip, ultra-high bandwidth optical networks which are critical for the future of microelectronics. One of the bottlenecks for multi-core, multi-processor electronics is the on-chip copper wire interconnect network. Integrated photonics seek to transfer the data transmission from the electrical domain to the optical domain just as fiber has done for long haul communications. Nonlinear optics has a role to play in providing some of the necessary components for such a network. Silicon has emerged as a key material for integrated photonics due to the CMOS processing capabilities, its high index contrast, electro-optic properties and strong nonlinearity. However, silicon experiences severe nonlinear losses which limit the efficiency of processes such as four-wave mixing and Raman amplification.

This dissertation examines a new material platform for integrated nonlinear photonics by developing silicon nitride waveguides and resonators. We start with background information on the field and motivation for integrated photonics and nonlinear optics. We then develop a theoretical foundation for optical waveguides and ring resonator devices by deriving the key governing equations and parameters. The material properties and fabrication techniques are described in detail and we are able to measure the nonlinear refractive index of silicon nitride through the nonlinear self-phase modulation. We explore the process of four-wave mixing in waveguides to demonstrate efficient wave-

length conversion and parametric gain. By leveraging the parametric gain and high quality factor resonators, we demonstrate the first fully integrated optical parametric oscillation and frequency comb generation. We go on to show one of the potential applications of this device as a multiple wavelength source for wavelength division multiplexed optical networks. We also discuss harmonic generation in which infrared light is converted to visible wavelengths. We exploit an interface effect to induce the second order nonlinearity in the material which could enable a host of other nonlinear process previously inaccessible to CMOS-compatible photonics. In the summary we discuss a wide array of future work that could build on the material presented here.

BIOGRAPHICAL SKETCH

Jacob Samuel Levy was born on Monday, June 4, 1984 in St. Louis, MO. This was no doubt a joyous occasion for his parents, Joe and Gayle, and grandparents, Paul, Helga, David and Sylvia, as he was the first child of his generation. The very same day Bruce Springsteen released his album "Born in the USA" which drives home themes of positive spin in the face of struggle and hardship. Jacob likes to believe in the pragmatic realist view of life whereby he accepts the difficult twists and turns but perseveres by applying a simple mantra of "Stay Calm, Don't Panic!" After struggling through an awkward teenage phase in which his hair was several inches too long and his sense of style was severely lacking, Jacob graduated from Ladue Horton Watkins High School in 2002. He matriculated the following fall at Duke University where he majored in electrical and computer engineering, and painted his body a handful of times in support of the university's men's basketball team. Among other formative experiences during his undergraduate years, he studied abroad at Queen Mary College, University of London in the fall of 2004 and was an NSF sponsored REU fellow for Professor Richard Osgood's group at Columbia University in the summer of 2005. In the fall of 2005 he joined the Duke Nanophotonics Lab of Professor Tomo Yoshie and decided to pursue graduate studies after the completion of his B.S. in December 2005. In the fall of 2006 he enrolled in Cornell University's M.S./Ph.D. program and joined the school of electrical and computer engineering. His doctoral work was under the direction of Professor Michal Lipson and as a member of the Cornell Nanophotonics Group he has explored nonlinear optics in silicon and silicon nitride waveguides.

To my parents, Melissa and Duke

ACKNOWLEDGEMENTS

I would like to begin by thanking my advisor, Professor Michal Lipson. I am extremely grateful and honored to have worked with her for my doctoral research. She is an incredibly brilliant, energetic and genial scientist and person. I have learned from her how to tackle research problems, expand the scope of potential solutions, recognize the big picture and cogently present ideas. The research group she has grown at Cornell is truly awe inspiring in the breadth of topics it covers, the quality of work it performs, and the caliber of student and researchers it attracts. Anything I have accomplished as a scientist I owe to her. Her tireless efforts in securing research grants and promoting the work have never left me needing something in the lab or unsure about beginning yet another costly fabrication run.

I would also like to acknowledge the other members of my committee: Professors Clifford Pollock and Alexander Gaeta. Alex especially has been a critical influence on the direction of my research. The fruitful collaborations I have had with many members from his group have led to me testing for more in his labs than Michal's in the past two years.

My research was funded in part by the Defense Advanced Research Projects Agency POPS program and Optical Arbitrary Waveform Generation Program. Some of my earlier research was funded by the DARPA Slow Light program. I would also like to thank the Center for Nanoscale Systems at Cornell. This work was performed in part at the Cornell NanoScale Facility, a member of the National Nanotechnology Infrastructure Network, which is supported by the National Science Foundation.

I am also indebted to the numerous members, past and present, of the Cornell Nanophotonics Group. Dr. Carl Poitras has always provided help with

anything I have asked from how to run a simulation to finding/fixing a piece of equipment. I would like to thank Dr. Qianfan Xu for introducing me to the concept of a ring resonator and giving me my first photonic chip to test, Dr. Stefen Preble for assisting me with my nascent adventures in slow light and Dr. Brad Schmidt for his welcoming me into the group and refreshing anecdotes covering an eclectic range of topics. Brad represents the amalgamation of knowledge to which I aspire. I would like to thank Dr. Christina Manolatou for her finite difference mode solver. Dr. Po Dong was a great help with some of my early fabrication efforts and brought a great energy to the group. Dr. Jacob T. Robinson, the self-monickered number 1, was not only a brilliant scientist but took it upon himself to ensure the spirit of the entire group was always at a high and to throw a party or two as needed. Dr. Long Chen awed me with his technical knowledge and was always willing to assist with problems ranging from the theoretical to fabrication. Dr. Danilo Spadoti and Bernardo Kyotoku were part of the Brazillian wave that overtook CNG for a little while and both brought with them fresh ideas and outside perspecitives to nanophotonics. Dr. Sasikanth Manipatruni and I had many fruitful discussions ranging from the topic of our research to important things like the finer points of cricket. Sasi's brilliance and breadth of knowledge always impressed me and he taught me that everything I need to know I probably learned in high school (or at least Sasi learned it in high school). Thank you to Dr. Gustavo Wiederhecker for his development of the customized finite element method mode solver. Gustavo seems to have an in-depth knowledge of every physics topic and was a useful resource for any technical question that arose. I am also thankful he is a vegetarian so I was never a lone voice when the group was deciding where to eat.

To Dr. Arthur Nitkowski, Dr. Nicolás Sherwood Droz and Dr. Kyle Preston, it was a great pleasure to overlap with you guys for my entire graduate career (the past few weeks in the office just haven't felt right without you here). I consider all of you close friends and you certainly made my experience at Cornell a lot more fun. I was glad to be able to finally collaborate with Nick and Kyle on a little side project over the past year. I would also like to acknowledge the master, not yet doctor, Hugo Lira; if I were not driven to finish before him I might never graduate. In seriousness, Hugo is an incredibly talented engineer who's hard work and MathCAD skills are inspiring. I have greatly enjoyed working next to him for the past four years. Dr. Mohammad Soltani has provided me with some helpful insights into ring resonators and the field of integrated optics in general. I would like to thank him for his constant encouragement, positive attitude, and assistance with simulations. Dr. Michael Menard has been another member of the "fabricate nonlinear optical devices at the bequest of a dozen other people before you can do your own research" group along with me. I thank him for his camaraderie in that regards. To Lian-Wee Luo, thank you for introducing me to the term "auntie" and the many fruitful discussions we have had about optical devices, life in Singapore and soccer. I would like to take this space to remind you that Man. U. sucks. Lucas Gabrielli, thank you for developing the gdspy code and demonstrating the power of open source and Linux. I will never forget how Debo Olaosebikan outlined how all one's doctoral research could be completed in seven days. I am glad to count many of the newer students to the group Biswajeet Guha, Mian Zhang, Vishal Chandrasekar, Daniel Lee, Shreyes Shah, Lawrence Tzuang, Kevin Luke and Austin Griffith as friends and collaborators. I am confident the group is in good hands and bright minds moving forward. To Austin, Kevin and Lawrence, I hope you find much success

continuing the research I have presented here and hopefully I have passed on sufficient knowledge for you to excel in such endeavors. I hereby pass the torch.

I would like to single out a few other individuals who have had particular impact on my career. Dr. Alexander Gondarenko, thank you for helping me develop a process for silicon nitride from scratch. You truly pioneered this undertaking for the group and much of the fabrication work presented here owes a credit to your "unique" clean room techniques. I am also indebted to Dr. Jaime Cardenas for his development of fabrication process flow and his wide knowledge of both fabrication and optical devices. It has been a pleasure working with him over the past four years and have greatly enjoyed our collaborations. Dr. Amy Foster provided an immense amount of guidance in my first years as a graduate student. Without her tremendous amount of help in understanding the nonlinear processes I discuss in this thesis I am not sure what direction my graduate work would have taken. Dr. Mark Foster from Alex Gaeta's group also had a tremendous influence on my research. I am extremely grateful for his willingness to share with me his exhaustive knowledge of integrated nonlinear optics and ingenious ideas for new experiments. I feel lucky to count Mark and Amy as my friends and am indebted to them for dog-sitting in addition to many other things.

I would also like to thank Dr. Yoshitomo Okawachi, Kasturi Saha, Dr. Pablo Londero, Dr. Stephane Clemmen, Alessandro Farsi and Henry Wen from the Gaeta group with whom I have collaborated on numerous projects both successful and failed. To Yoshi and Kasturi especially I am indebted for their help on some of the more recent work probing the properties of the silicon nitride freqeuncy combs. The other members past and present of the Gaeta group have always welcomed me into their labs and assisted me with tracking down equip-

ment during my many collaborations. I have also been fortunate enough to collaborate with Dr. Keren Bergman's research group at Columbia University. My thanks go to Dr. Aleksandr Biberman, Noam Ophir, Johnnie Chan, and Gilbert Hendry for their fruitful collaborations.

A great deal of thanks are due to Kim Cotton, Shawna Fulkerson, Robert Roy and Sue Bulkley for their tremendous administrative work. I am not envious of the task of maintaining Michal's schedule and am indebted to their efforts in scheduling meetings and keeping us apprised of her whereabouts.

Last but not least I would like to thank my family and friends who have encouraged me and kept me sane during my time at Cornell. First my parents for their continuous support for everything I undertake. I could not dream of having a better upbringing and consider myself very fortunate to have parents like you. Thanks also goes to my siblings, Adam, Jenny and Ben whom I wish I got to see more and when our paths do cross fill me with constant joy. To Duke, you are a good dog and I'm sure will get more out of this dissertation than most. Finally to Melissa, you have been a constant source of joy, support and encouragement during my time in Ithaca. I know you sometimes struggled to see the necessity of many late nights in the clean room or lab, but am thankful for your steadfast loyalty and trust that I knew what I was doing. We have already had many adventures together and I look forward to a future filled with many more, one that I am proud to share with you.

TABLE OF CONTENTS

LIST OF TABLES

LIST OF FIGURES

CHAPTER 1

INTRODUCTION

We have recently seen enormous growth in the field of optical communications. The wide deployment of optical fiber and the development of low-cost amplifiers enabled the transmission of data rates exceeding $1\,\mathrm{Tb\,s^{-1}}$ over many kilometers on a single fiber. In fact optics have now taken over for electronics for most long-haul communication. Concurrently, the continuation of Moore's law [1] has seen computing capacity grow exponentially. The ability to generate and consume massive amounts of data with applications ranging from popular consumption to medical diagnostics have placed humanity squarely within the information age. However copper wire interconnects have degraded performance at the high data rates processors are now approaching [2]. Integrated photonics has been suggested as a possible solution to overcome this data bottleneck [3, 4]. Already optics have become standard in data centers and high-performance computing applications connecting rack to rack across distances of only a few meters.

1.1 Integrated CMOS-Compatible Photonics

The emerging field of silicon photonics seeks to unify the high bandwidth of optical communications with complimentary metal-oxide-semiconductor (CMOS) microelectronic circuits. One of the limiting factors for optical communications has been the high costs associated with both integration and exotic materials (III-V). By using CMOS-compatible materials, which are abundant and cheap, we can leverage the mature processing technology of the microelectronics in-

dustry to significantly reduce the cost of integrated photonics. The use of these materials could also enable the close integration of electronics with photonics in a monolithic approach and avoid the parasitics of bonding or multi-chip solutions.

A key benefit of optical communication systems is wavelength-division multiplexing (WDM) which enables a single waveguide to carry multiple data streams and is essential to reach the full bandwidth potential of photonic integrated circuits. Many components have recently been developed in silicon to enable such a network including electro-optic modulators [5, 6, 7], integrated germanium photodetectors [8, 9, 10], switches [11, 12, 13], and filters [14, 15], among other devices. Some of the key components that enable high-bandwidth optical communication networks rely on nonlinear phenomena. Additionally, with any multi-wavelength or high power architecture, nonlinear effects cannot be ignored in design and performance evaluation.

1.2 Nonlinear Optics

With the advent of the laser just over fifty years ago [16] strong optical fields were accessible for the first time. The large field strength enabled the discovery of second-harmonic generation (SHG) [17] and the field of nonlinear optics was born. Over the past fifty years the field has grown immensely and ranges from fundamental studies of light matter interaction to practical applications in optical communication systems. Some of the most exciting applications are parametric, in which the optical energy in the process is conserved.

Since nonlinear interactions depend on the field intensity, the tighter the fo-

cus of an optical beam, i.e. the smaller the effective area, the stronger the nonlinear response. The interaction length, another important factor in determining the strength of nonlinear processes, is traditionally determined by the diffraction limit of the focused beam. Since beams with a smaller focal area have a shorter diffraction length, there is an intractable trade-off between intensity and length.

By using an optical waveguide, we can increase the interaction length beyond the diffraction limit. Much work has been done exploiting the low-loss of optical fibers to show a rich array of potential nonlinear processes. More recently, work has been done on integrated photonic devices, which confine light to an even smaller scale. Silicon-based nonlinear devices have already enabled high-speed data processing [18], parametric amplification [19], signal regeneration [20], demultiplexing [21], and utlra-fast signal detection [22]. However, nonlinear loss mechanisms limit the efficiency of many processes in silicon. This dissertation explores the interactions of strong fields in silicon nitride waveguides in hopes of overcoming the limitations of silicon.

1.3 Organization

This dissertation focuses on the applications of silicon nitride waveguides and ring resonators for parametric nonlinear processes. In chapter 2, we examine the waveguide solution to Maxwell's equations in dielectric materials for both linear and nonlinear regimes. We also introduce the concepts of effective index, group index and group velocity dispersion which arise from the solutions to the wave equation. The ring resonator is also described and the pertinent proper-

ties for the device are analyzed. We move on to discuss the relevant CMOS-compatible photonic materials and fabrication techniques in chapter 3. We conclude that for nonlinear optics silicon nitride has the potential to outperform the current state of the art. In chapter 4, the measurements on the losses for silicon nitride waveguides as well as the intrinsic nonlinear parameters for the device are described. We introduce four-wave mixing and demonstrate both parametric gain and high-efficiency wavelength conversion in chapter 5, and by utilizing the parametric gain we are able to achieve optical parametric oscillation on-chip as discussed in chapter 6. In that chapter we also introduce a fully integrated frequency comb generation. In chapter 7, we describe one of the potential uses for such a device: as an integrated multi-wavelength source. We measure the performance of the individual comb lines and test their linewidth, temporal stability and capacity for high-speed data transmission. The final topic we discuss is harmonic generation in silicon nitride rings. In chapter 8, we explore the expected third harmonic generation which arises from the bulk nonlinearity and also the unexpected second harmonic generation which comes from interface effects. We conclude with a summary in chapter 9 which also includes many potential research directions to build on the work presented in this dissertation.

CHAPTER 2

NONLINEAR OPTICS IN WAVEGUIDES

2.1 Introduction

In this chapter we will work from first principles to examine electromagnetic fields in dielectric waveguides. We will work from Maxwell's equations for dielectrics in section 2.2, where we show how the polarization field can be dependent on the strength of the electric field when higher order terms are included giving rise to nonlinearities. In section 2.3, we derive the wave equation for a single optical frequency in an isotropic material for both linear and nonlinear cases. We then show the solutions for a rectangular waveguide in section 2.4 and discuss simulation methods to solve for the optical modes of the equations. In section 2.5, we describe the effective index, group index and group velocity dispersion for nano-waveguides.

Optical resonators have long been used to enhance the intensity of light for nonlinear interactions. By forming a ring, essentially a bent waveguide that connects to itself, we can form an integrated resonator with strong electric field enhancement. In section 2.6, we develop the theoretical foundation for a ring resonator: resonance conditions, the photon lifetime, field enhancement, and free-spectral range.

2.2 Maxwell's Equations and Constitutive Relations

Maxwell's equations as formulated in the macroscopic case in terms of free charge and current presented in differential form are as follows:

$$\nabla \cdot \mathbf{D} = \rho \tag{2.1a}$$

$$\nabla \times \mathbf{E} = \frac{-\partial \mathbf{B}}{\partial t} \tag{2.1b}$$

$$\nabla \cdot \mathbf{B} = 0 \tag{2.1c}$$

$$\nabla \times \mathbf{H} = \mathbf{J} + \frac{\partial \mathbf{D}}{\partial t} \tag{2.1d}$$

Where $\mathbf{E}$ is the electric field, $\mathbf{H}$ is the magnetic field $\mathbf{D}$ is the electric flux density and $\mathbf{B}$ is the magnetic flux density. For the purposes of this dissertation, we will assume the current density, $\mathbf{J}$, and the charge density, ρ, are 0 since we will be examining source free mixed dielectric structures.

We can also define the constitutive equations relating the flux densities to the field amplitudes as follows:

$$\mathbf{D} = \epsilon_0 \mathbf{E} + \mathbf{P} \tag{2.2a}$$

$$\mathbf{B} = \mu_0 \mathbf{H} + \mathbf{M} \tag{2.2b}$$

where $\epsilon_0 = 8.85 \times 10^{-12}\,\mathrm{F\,m^{-1}}$ and is the permittivity of free-space and the vacuum permeability $\mu_0 = 4\pi \times 10^{-7}\,\mathrm{H\,m^{-1}}$. For the remainder of the dissertation we will deal solely with nonmagnetic materials so that the magnetic polarization, $\mathbf{M}$, is zero.

The polarization field, $\mathbf{P}$, will be examined from two perspectives. The first is the simplest case in which the polarization is assumed to depend linearly on the strength of the electric field:

$$\mathbf{P} = \epsilon_0 \chi^{(1)} \mathbf{E} \tag{2.3}$$

where $\chi^{(1)}$ is the linear susceptibility of the material and is related to the relative permittivity of a material, ϵ, with the relationship $\chi^{(1)} = \epsilon - 1$. The material permittivity and permeability have so far been represented as scalar quantities for simplicity. Strictly speaking these are tensor values, but for the isotropic mediums we will be examining here, we can view them as scalar quantities for homogeneous medium and vector quantities when we work with multiple materials.

For nonlinear optics, the polarization can be written as a power series of the electric field amplitude [23], and Equation 2.3 can be expanded:

$$\mathbf{P} = \epsilon_0 \left[\chi^{(1)}\mathbf{E} + \chi^{(2)}\mathbf{E}^2 + \chi^{(3)}\mathbf{E}^3 + \cdots \right] \tag{2.4}$$

where $\chi^{(2)}$ is the second order susceptibility and $\chi^{(3)}$ is the third order susceptibility. In centrosymmetric materials the bulk $\chi^{(2)}$ vanishes making $\chi^{(3)}$ the lowest nonlinear term of the polarization. However, as will be discussed in Chapter 8, an effective $\chi^{(2)}$can arise in waveguides from the interface between the core and the cladding. The first term of the power series is equivalent to the polarization defined in equation 2.3. The higher order terms can be lumped together and defined as the nonlinear polarization $\mathbf{P}^{\mathrm{NL}}$. For most materials, the relative difference in strength for $\frac{\chi^{(n)}}{\chi^{(n+1)}}$ is about seven orders of magnitude. Therefore, we can usually ignore all but the lowest order nonlinearity.

2.3 Wave Equation

To solve the equations for light propagating in a dielectric medium we employ a separation of variables to isolate the spatial and temporal components of the

fields involved in Maxwell's equations. Taking these considerations into account, we rewrite the **E**, **H** and **P** as follows:

$$\mathbf{E}(\mathbf{r},t) = \mathbf{E}(\mathbf{r})\, e^{j\omega t} + \text{c.c.} \tag{2.5a}$$

$$\mathbf{H}(\mathbf{r},t) = \mathbf{H}(\mathbf{r})\, e^{j\omega t} + \text{c.c.} \tag{2.5b}$$

$$\mathbf{P}(\mathbf{r},t) = \mathbf{P}(\mathbf{r})\, e^{j\omega t} + \text{c.c.} \tag{2.5c}$$

Here ω is defined as the angular frequency of the wave. We also need to take into account material dispersion which accounts for the change in permittivity as a function of frequency so ϵ becomes $\epsilon(\omega)$. In the simplest case, we will use equation 2.3 to define the relation between **D** and **E**, with the result from combining equations 2.2a and 2.3 being $\mathbf{D} = \epsilon_0 \epsilon \mathbf{E}$. In the assumption of linear and isotropic materials, the scalar value of ϵ is the square of the familiar parameter n, the material refractive index. For a propagation in a single dielectric medium, we can take the curl of equation 2.1b and substitute equation 2.1d to get [24]:

$$\nabla \times \nabla \times \mathbf{E}(\mathbf{r},t) = -\mu_0 \epsilon_0 \epsilon(\omega) \frac{\partial^2 \mathbf{E}(\mathbf{r},t)}{\partial t^2} \tag{2.6}$$

Here we can define the speed of light in vacuum, $c = 1/\sqrt{\mu_0 \epsilon_0} = 2.998 \times 10^8\,\mathrm{m\,s^{-1}}$. With a little manipulation and the assumption that the gradient of the refractive index is zero, by substituting equation 2.5 into equation 2.6 we arrive at the familiar wave equation[25, 26]:

$$\nabla^2 \mathbf{E}(\mathbf{r}) - n^2(\omega) \frac{\omega^2}{c^2} \mathbf{E}(\mathbf{r}) = 0 \tag{2.7}$$

and a similar solution can be shown for the magnetic field amplitude, **H**.

By substituting equations 2.5a and 2.5b into the divergence equations 2.1a and 2.1c we find the solution to equation 2.7 must be plane waves. We can

further define the electric and magnetic spatial field components as treated in [24, 26] so we have:

$$\mathbf{E}(\mathbf{r}) = E_0 e^{j\mathbf{k}\cdot\mathbf{r}} \tag{2.8a}$$

$$\mathbf{H}(\mathbf{r}) = H_0 e^{j\mathbf{k}\cdot\mathbf{r}} \tag{2.8b}$$

where E_0 and H_0 are the scalar electric and magnetic field amplitudes, $\mathbf{k}$ is the wavevector and from solving equation 2.7 is related to the angular frequency, refractive index and speed of light:

$$|\mathbf{k}| = n(\omega)\frac{\omega}{c} = \frac{2\pi}{\lambda} \tag{2.9}$$

where we also relate the wavevector to the wavelength of light, λ.

Taking into account the higher order terms of the polarization by using equation 2.4 we can derive a variant of equation 2.7 to include the nonlinear effects of $\mathbf{P}^{\mathrm{NL}}$ [23, 25]:

$$\nabla^2\mathbf{E}(\mathbf{r}) - n^2(\omega)\frac{\omega^2}{c^2}\mathbf{E}(\mathbf{r}) = -\frac{\omega^2}{\epsilon_0 c^2}\mathbf{P}^{\mathrm{NL}}(\mathbf{r}) \tag{2.10}$$

Using this equation will enable us to build up the various nonlinear phenomena observed in waveguides in the following chapters.

2.4 Waveguide Solution

The guided waves of interest in this dissertation are derived from plane wave solutions to the Helmholtz form of equation 2.7 as applied to a channel waveguide. The principle of guiding for the structure is total internal reflection (TIR). In this section, we present a ray picture of TIR as derived from Snell's law and the law of reflection, then we examine the wave description of the phenomena. Next, we examine the solution for an infinite slab showing the formation

of transverse electric (TE) and transverse magnetic (TM) modes. Finally, we show that a solution for a rectangular waveguide can be analytically solved and discuss numerical simulations or "mode solvers".

2.4.1 Total Internal Reflection

The physical process which enables an electromagnetic wave to be guided in a core of higher index material surrounded by a lower index cladding is TIR.

Ray Tracing

The simplest way to visualize TIR is by the ray picture. We will consider the case for a high index material surrounded on both sides by the same lower index material as shown in figure 2.1. The two basic laws covering this geometric optic picture are given as follows:

$$n_1 \sin\theta_1 = n_2 \sin\theta_2 \tag{2.11a}$$

$$\phi_i = \phi_r \tag{2.11b}$$

From Snell's law, equation 2.11a, we can calculate the angle of refraction at an interface of two materials with different indices and from the reflection law, equation 2.11b, we know the angle of reflection is equal to the angle of incidence.

At a critical angle, θ_c, no light will be refracted into the lower index material and using Snell's law we can solve this angle to be:

$$\theta_c = \sin^{-1}\left(\frac{n_1}{n_2}\right) \tag{2.12}$$

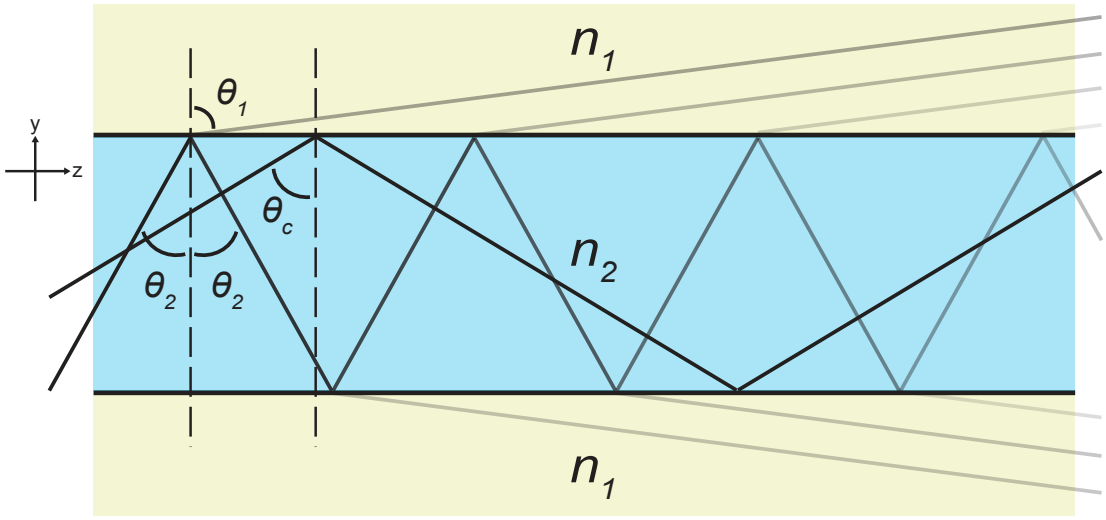

Figure 2.1: **An illustration of ray optics with a high index material, n_2, surrounded by a lower index material, n_1.** At a shallow angle of incidence, θ_2, the light is refracted into the lower index material at the corresponding angle, θ_1 and reflected in the high index material at angle θ_2. For angles larger than the critical angle such as θ_c, no light is refracted into the cladding material and there is total internal reflection in the guiding layer.

As shown in figure 2.1 angles of incidence at the critical angle or greater will be confined to the larger index material and angles shallower will leak into the lower index materials.

Wave Description

Let's now consider instead of light rays, figure 2.1 consists of plane waves propagating with each ray constituting the wavevector, **k**. Let's also examine the case for the Transverse Electric (TE) polarized wave, so that the E-field is along the x-axis or out of plane. We will consider the case in which the waves are refracted into the low index material and then generalize for the TIR case. This derivation follows [24] and the transverse components of **E** in the respective

materials follow the form:

$$\mathbf{E}_1(y,z) = \tau E_0 e^{jk_0 n_1 (y\cos\theta_1 - z\sin\theta_1)} + \text{c.c.} \tag{2.13a}$$

$$\mathbf{E}_2(y,z) = E_0 e^{jk_0 n_2 (y\cos\theta_2 - z\sin\theta_2)} + \text{c.c.} \tag{2.13b}$$

where τ is the transmission coefficient of the wave at the interface and k_0 is the free-space wavenumber. For an arbitrary angle of incidence, we use Snell's law to solve for θ_1. Substituting into equation 2.13a, we can examine the resulting wave in the low index material:

$$\mathbf{E}_1(y,z) = \tau E_0 e^{jk_0\left(yn_1\sqrt{1-\left(n_2^2/n_1^2\right)\sin^2\theta_2} - zn_2\sin\theta_2\right)} + \text{c.c.} \tag{2.14}$$

We notice the propagation coefficient in the z-direction becomes the same as for $\mathbf{E}_2$ from equation 2.13b. We will define the propagation coefficient as β such that:

$$\beta = k_0 n_2 \sin\theta_2 \tag{2.15}$$

also note β is the z-component of $\mathbf{k}$. The second consequence of equation 2.14 is when θ_2 exceeds the critical angle, the radical becomes imaginary. Therefore, the y-component of $\mathbf{E}_1$ will decay exponentially meaning the wave is confined to the high-index region.

2.4.2 The Infinite Slab

From the discussion of the wave picture of TIR we can begin to form a conceptual picture of a waveguide. In figure 2.2a, a drawing of the symmetric infinite slab waveguide is presented. In this picture, we will assume propagation in the z-direction and we will imagine that the high index slab extends out indefinitely in the x-direction. By taking a slice in the yz-plane, the infinite slab waveguide is transformed to the two dimensional picture in figure 2.1.

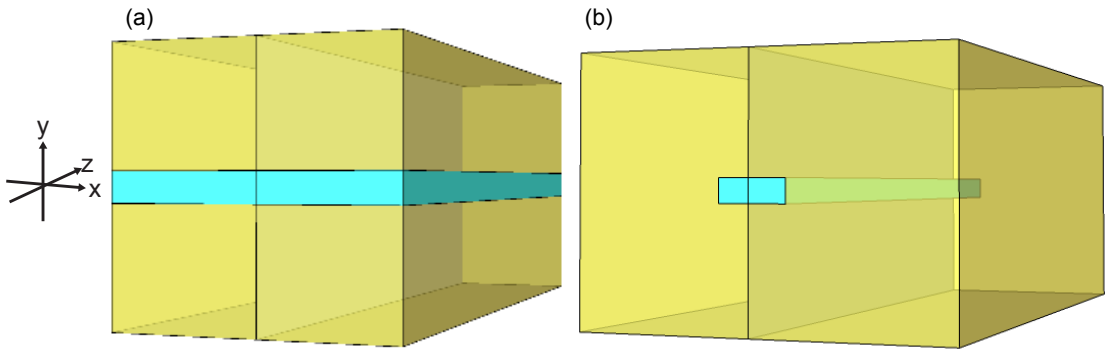

Figure 2.2: **Three dimensional waveguide depictions. a.** An infinite slab waveguide, in which the blue guiding core should extend infinitely in the x-direction, and **b.** A buried channel waveguide with propagation along the z-axis. The slab in the center of both pictures will give the same 2-D cross-section and look the same as figure 2.1 for the TIR example.

Although it is not made clear in the previous section, the solution to equation 2.13 cannot have any arbitrary β that satisfies the critical angle condition. Rather, discrete modes are formed as solutions to the guided wave equation because there is a phase-shift (the Goos-Hänchen shift) at the interface of the core and cladding materials. Therefore, to avoid destructive interference as the wave propagates, the total phase-shift (from the propagating wave and the two-shifts at the guide boundaries) must be an integer multiple of 2π.

From the wave picture, we will now show the formation of guided modes in the waveguide building from equations 2.7 and 2.8. We will examine the TE case in which the electric field is polarized in the x-direction and equation 2.8a becomes [24, 27]:

$$E_x(y,z) = E_0 E_x(y) e^{-j\beta z} \tag{2.16}$$

and we can solve equation 2.7 for all space:

$$\frac{\partial^2 E_x}{\partial y^2} + \left(k_0^2 n_i^2 - \beta^2\right) E_x = 0 \tag{2.17}$$

where $k_0 = \omega_0/c$ is the free-space wavevector and n_i is the refractive index in the

core or cladding. If we examine only solutions of β that experience TIR and can therefore be confined to the core we find the general solution to equation 2.17 for the TE mode assuming the core region from figure 2.2a extends from $\pm a$:

$$E_x(y) = \begin{cases} A_1 e^{-(y-a)\sqrt{\beta^2 - k_0^2 n_1^2}} & \text{for } y > a \\ A_2 \cos\left(y\sqrt{k_0^2 n_2^2 - \beta^2}\right) \text{ or } A_3 \sin\left(y\sqrt{k_0^2 n_2^2 - \beta^2}\right) & \text{for } a \geq y \leq -a \\ A_4 e^{(y+a)\sqrt{\beta^2 - k_0^2 n_1^2}} & \text{for } y < -a \end{cases} \tag{2.18}$$

where the cosine term corresponds to even modes of the waveguide (i.e. the mode profile has even symmetry) and the sine solution corresponds to the odd waveguide modes. The coefficients A_i can be reduced to a single value and a transcendental equation for the allowable modes can be found by using the boundary conditions at the interface that both $E_x(y)$ and $\partial E_x(y)/\partial y$ are continuous. We will define two new parameters: the delay coefficient γ which is equal to the radical for the cladding regions and the transverse wavevector κ which is equal to the radical in the cladding. For the even modes we can use the first boundary condition to reduce equation 2.18 to:

$$E_x(y) = \begin{cases} Ae^{-\gamma(y-a)} & \text{for } y > a \\ A\frac{\cos(\kappa y)}{\cos(\kappa a)} & \text{for } a \geq y \leq -a \\ Ae^{\gamma(y+a)} & \text{for } y < -a \end{cases} \tag{2.19}$$

and a similar solution can be found for the odd (sine) modes. In this case both κ and γ are dependent on β. For determining the real solutions of β we rely on the second boundary condition and find the eigenvalue equation:

$$\tan(\kappa a) = \frac{\gamma}{\kappa} \tag{2.20}$$

It is useful at this point to add another definition:

$$n_{eff} \equiv \beta / k_0 \tag{2.21}$$

where n_{eff} is the effective index of the guided mode which will become useful in describing the modes for the channel waveguide in the next section. We can also see how this intuitively redefines the parameters γ and κ in terms of refractive index differences.

2.4.3 Channel Waveguide

The channel waveguide is the basic photonic structure used for the work done in this dissertation. As depicted in figure 2.2b, the optical device is defined by a rectangular core region surrounded by a lower index cladding material. Since we are now confined in two dimensions we no longer have pure TE or TM modes. However, we still have modes that are quasi-TE or quasi-TM where the dominant part of **E** is in the x- or y-axis (shown in figure 2.3) respectively. For the remainder of the dissertation these modes will simply be referred to as TE or TM. Marcatili [28] pioneered a method for solving the rectangular waveguide using a wave analysis similar to that shown for the infinite slab waveguide in the previous section. The interested reader should look to [24, 27] for a good review of this analysis. For our purposes we will examine the more general effective index method [29] and discuss the software used for mode solvers of arbitrary waveguide geometries.

Effective Index Method

A simple method for analytically solving for the allowed modes of a rectangular waveguide is the effective index method first proposed by Knox and Toulios [29] and applied to rectangular waveguides by Hocker and Burns [30]. The beauty

of this method is that it turns a single two-dimensional problem into two one-dimensional problems. In figure 2.3a, we draw the symmetric two-dimensional waveguide with a core index of n_2 embedded in a cladding material with a lower index of n_1. As with the wave solution [28], the hashed regions of the waveguide in figure 2.3a can be ignored when solving for β in the waveguide.

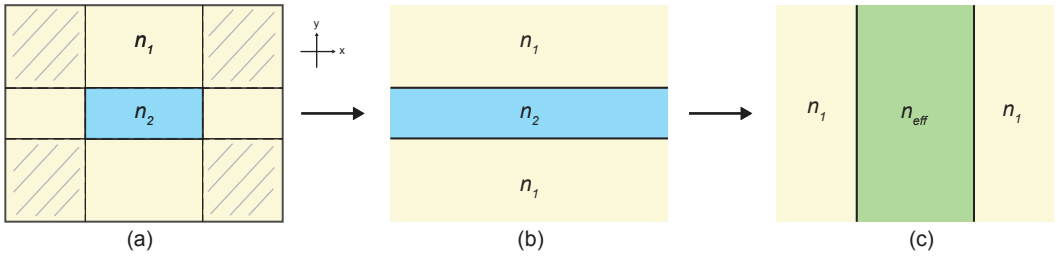

Figure 2.3: **An illustration of the effective index method. a.** The symmetric rectangular waveguide as in Figure 2.2b depicted in the xy-plane. **b.** The slab equivalent of the rectangular waveguide in the x-direction. **c.** After a solution is found for the first slab waveguide, a second slab is formed in the y-direction with the index of the core material set to the n_{eff} solved from the first slab mode.

The first step is to take the thinner dimension, in this case the y-dimension, and stretch the waveguide into an infinite slab along the opposite axis as in figure 2.3b, i.e. there is no longer a field dependence in the thinner dimension of the waveguide. For solving the TE mode of the waveguide, where **E** is polarized along the x-axis, we use equation 2.20 to calculate the allowed values of β for the slab mode. From the solution for the propagation vector, we derive the n_{eff} using equation 2.21. This value is then plugged into the core of the thicker waveguide dimension shown in figure 2.3c. We view this problem as another infinite slab waveguide, but must be careful to use the proper characteristic equation. Given the polarization of **E**, we need to solve for the TM mode of the second slab waveguide. The transcendental equation can be calculated

from the TM-counterpart to equation 2.19 as:

$$\tan(\kappa a) = \left(\frac{n_2}{n_1}\right)^2 \frac{\gamma}{\kappa} \tag{2.22}$$

It should be noted that the effective index method is only valid for large aspect ratios [24], so that it is easy to determine in which dimension the waveguide should first be expanded.

Mode Solvers

Two popular methods for numerically solving partial differential equations (PDE) on arbitrary geometries are the the finite difference method (FDM) and the finite element method (FEM). In work for this dissertation, both have been used to solve for the modes of channel waveguides of various geometries using the Helmholtz equation (equation 2.7). Both methods break the problem into a mesh for analysis as shown in figure 2.4.

The FDM solver breaks the problem up into a grid of two dimensions. It then substitutes the PDE out for a finite difference scheme between grid points. In doing so it creates a system of equations in a matrix form that can then be solved to find the eigenvalues of the system. The accuracy of the solution is proportionate to the fineness of the grid, therefore, a very fine grid is required near boundaries. Unfortunately, (from the perspective of required computational power) the rectangular grids must extend through the entire domain.

The FEM method is better able to handle arbitrary geometries such as the trapezoidal shape which comes from waveguide etching discussed in section 3.3.3. It breaks down the problem into a set of linearized equations solved

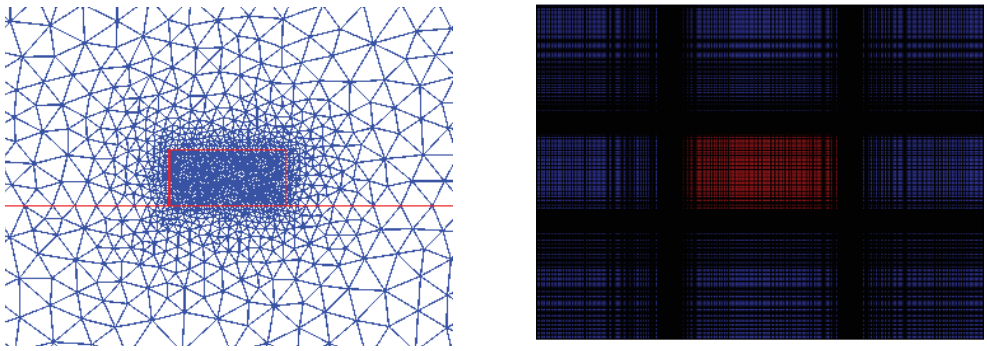

Figure 2.4: **Mode-solver meshes for a rectangular waveguide. a.** For the FEM solver with a triangular mesh. Here the triangles are arbitrarily conformed to the interfaces of the structure. and **b.** The mesh for the FDM solution, everything must be spaced in a grid formation.

for each triangle. The boundary conditions are used to make sure the solution is consistent with the surrounding triangle until an eigenvalue is found.

Both solvers are capable of solving for three cases. The first case requires the input of a specific frequency, ω, for a straight waveguide and provides a solution for β and using equation 2.21 the n_{eff}. The second case solves for a bent waveguide. Here, by a simple transformation of coordinates, we can solve β for the modes of a bent waveguide of some arbitrary radius. The third case is an axisymmetric modesolver. As will be discussed in section 2.6, a cavity is considered to have a resonance when an integer number of wavelengths fit perfectly inside. In this case of the solver, the user must input the mode number, (the number of wavelengths which fit in the cavity), and the bending radius and the solver finds the resonant frequency.

Using the FEM solver, we solve for a sample straight Si_3N_4 waveguide clad with SiO_2. The waveguide has the same dimensions as the mesh plot shown in figure 2.4a and we solve for an input wavelength of 1550 nm. Figure 2.5a

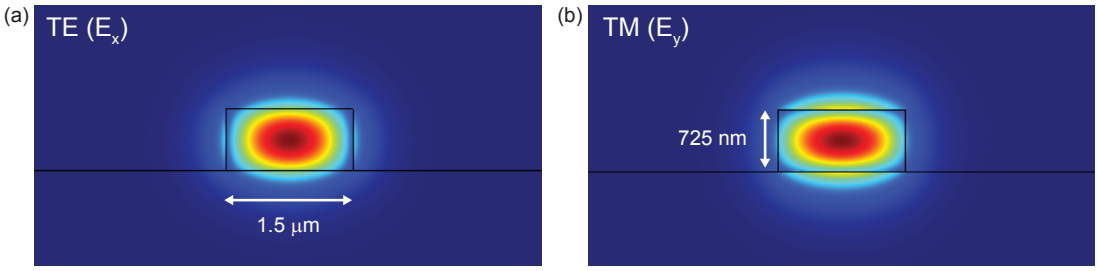

Figure 2.5: **Mode profiles for a sample solution to a Si_3N_4 waveguide.** The solutions are for an input wavelength of 1550 nm and the dominant component for the electric field of each mode is plotted in the xy-plane. **a.** The first order TE mode of the waveguide is plotted, we note the discontinuity of the electric field at the waveguide sidewalls in the x-direction as expected. The solver gives an n_{eff} for the waveguide of 1.8137. **b.** The first order TM mode for the same waveguide with an n_{eff} of 1.7.

shows the E_x component of the the first-order TE mode of the waveguide and figure 2.5b shows the E_y component of the first-order TM mode. By solving for a range of wavelengths, we can track how n_{eff} changes with λ (we will see the importance of this in sections 2.5 and 2.6). We also have free choice over waveguide geometry, core and cladding materials, and can find cutoff dimensions for higher-order modes or, for the case of asymmetric waveguides, propagation.

2.5 Group Index and Group Velocity Dispersion

In vacuum, the velocity of a plane wave is c. However, when traveling through a dielectric medium of index, n, the light is said to slow to a speed of c/n. The phase velocity is defined as the speed at which the phase of a single frequency component travels. In general this value is defined in terms of the angular fre-

quency and wavenumber such that:

$$v_p = \frac{\omega}{k} \tag{2.23}$$

However, in a waveguide where light is confined and propagates in a given direction we refine the definition:

$$v_p = \frac{\omega}{\beta} = \frac{c}{n_{eff}} \tag{2.24}$$

where we have substituted the propagation constant for the wavenumber. We substitute our definition of n_{eff} from equation 2.21 and arrive at the familiar relationship for the speed of light in a medium with index, n.

Because we know β is a function of frequency, the phase velocity must also change for different wavelengths. If we consider an optical pulse composed of multiple frequencies, we can define the group velocity v_g as the speed at which the envelope travels:

$$v_g = \frac{d\beta}{d\omega} \tag{2.25}$$

and substituting equation 2.21 we can rewrite equation 2.25:

$$\frac{1}{v_g} = \frac{1}{c}\left(n_{eff}(\omega) + \omega\frac{dn_{eff}}{d\omega}\right) = \frac{n_g}{c} \tag{2.26}$$

where n_g is the group index. Physically, the group velocity is the speed at which information is carried. It can be useful to consider the value in terms of λ:

$$n_g(\lambda) = n_{eff}(\lambda) - \lambda\frac{dn_{eff}}{d\lambda} \tag{2.27}$$

From these equations we can see that n_g is approximately n_{eff} with a slight adjustment for how the effective index changes with wavelength. The adjustment is often referred to as the dispersion of the material which can be defined as:

$$\beta_2 = \frac{d^2\beta}{d\omega^2} = \frac{1}{c}\left(2\frac{dn_{eff}}{d\omega} + \omega\frac{d^2n_{eff}}{d\omega^2}\right) \tag{2.28}$$

where β_2 is known as the group velocity dispersion (GVD) parameter and is responsible for phenomena such as pulse broadening. The parameter D is called the dispersion parameter and is defined as the change of $1/v_g$ with respect to wavelength:

$$D = \frac{1}{c}\frac{dn_g}{d\lambda} = -\frac{\lambda}{c}\frac{d^2 n_{eff}}{d\lambda^2} \tag{2.29}$$

Due to the phase-matching requirements for many of the nonlinear processes involving waves at non-degenerate frequencies, these parameters become very important for a waveguide. As we will later show, n_g and D are very sensitive to waveguide geometry [31, 32]. In the next section we will discuss how n_{eff} and n_g play a role in the properties of ring resonators.

2.6 Ring Resonator

After the waveguide, the second basic integrated optical structure used in this dissertation is the ring resonator. The resonator is a waveguide formed into a circle which can be accessed via a bus waveguide as shown in figure 2.6. The ring forms a traveling wave cavity in which the optical field circulates in the resonator. When light is on resonance, the field inside the cavity becomes enhanced and the intensity can grow very large. Looking at figure 2.6, we define the resonance condition to be when the phase of B_1 is the same as B_2, such that there is no phase-shift for the round-trip path of the resonator.

From equation 2.16 the phase-shift for an optical wave traversing an arbitrary distance is βz. Therefore, we can define the resonator phase-shift at a particular wavelength:

$$\phi(\lambda) = \beta(\lambda)\, 2\pi r = n_{eff}(\lambda)\, \frac{2\pi}{\lambda} 2\pi r \tag{2.30}$$

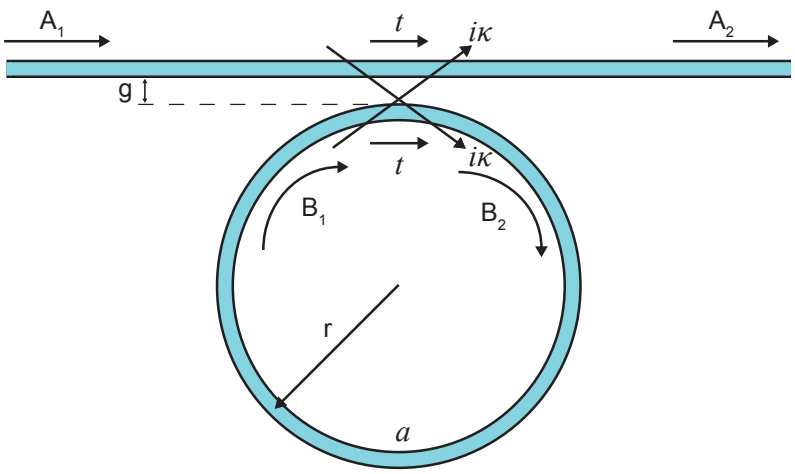

Figure 2.6: **An illustration of a waveguide coupled ring resonator.** The generic resonator shown has radius, r, and a coupling gap, g, from ring to waveguide. The diagram shows the coupling, κ, and transmission, t, coefficients for the input and output fields of the device as well as the round-trip loss factor, a.

with r the ring radius and λ the wavelength of operation. From this equation we can derive the resonance condition for when ϕ is an integer multiple of 2π:

$$m(\lambda_0) = \beta(\lambda_0)\, r = n_{eff}(\lambda_0)\, \frac{2\pi}{\lambda_0} r \tag{2.31}$$

where m, an integer, is the resonant mode number (remember this value is one of the parameters referred to in section 2.4.3 for the axisymmetric mode solver case) and λ_0 is the resonance wavelength.

We can describe all the relevant attributes of the ring using a steady-state derivation which follows the matrix formalism set forth by Yariv [33, 34, 35]. If in figure 2.6 we assume the input only comes from the A_1 side of the waveguide and the coupling from ring to waveguide is lossless, then the electric fields can be described by the transfer matrix:

$$\begin{bmatrix} A_2 \\ B_2 \end{bmatrix} = \begin{bmatrix} A_1 \\ B_1 \end{bmatrix} \begin{bmatrix} t & j\kappa \\ j\kappa & t \end{bmatrix} \tag{2.32}$$

with t the transmission coefficient, κ the coupling coefficient and the condition for a lossless coupler being:

$$|t|^2 + |\kappa|^2 = 1 \tag{2.33}$$

and j being added to the coupling term in equation 2.32 for the π phase shift of the ideal ring to bus waveguide coupler.

We would like to define all the fields in terms of the input field, A_1, but equation 2.32 only gives us two equations for three unknowns. We can relate the fields inside the ring, B_1 and B_2 as follows:

$$B_1 = ae^{j\phi(\lambda)}B_2 \tag{2.34}$$

where a is the round-trip propagation loss caused from either scattering, absorption or radiation. In terms of the m^{-1} power loss, α, which is commonly used to describe the losses for waveguides:

$$a = e^{-\alpha\pi r} \tag{2.35}$$

Consider now the case for normalized input power, where $|A_1|^2$ is equal to one. We can define the circulating power in the ring as a function of wavelength from equations 2.32 and 2.34:

$$P_{circ}(\lambda) = \left|\frac{B_1}{A_1}\right|^2 = \frac{a^2\kappa^2}{1 + a^2t^2 - 2at\cos(\phi(\lambda))} \tag{2.36}$$

and similarly for the transmitted power at the output of the waveguide:

$$P_{trans}(\lambda) = \left|\frac{A_2}{A_1}\right|^2 = \frac{a^2 + t^2 - 2at\cos(\phi(\lambda))}{1 + a^2t^2 - 2at\cos(\phi(\lambda))} \tag{2.37}$$

From equation 2.36, the maximum circulating power occurs when we meet the resonance condition of equation 2.31. The equation for the transmitted

power is reduced to:

$$P_{trans}(\lambda_0) = \frac{(a-t)^2}{(1-at)^2} \tag{2.38}$$

and therefore, we can have complete extinction of the input field when the transmission coefficient has the same value as the round-trip loss in the ring. This is known as critical coupling. We can show that this condition will also maximize the circulating power for the resonator:

$$\max|P_{circ}(\lambda_0)| = \frac{a^2}{(1-a^2)} \tag{2.39}$$

in a lossless resonator, i.e. $a = 1$, equation 2.39 goes to infinity. Therefore, as one would expect, the lower the resonator losses, the larger the circulating power.

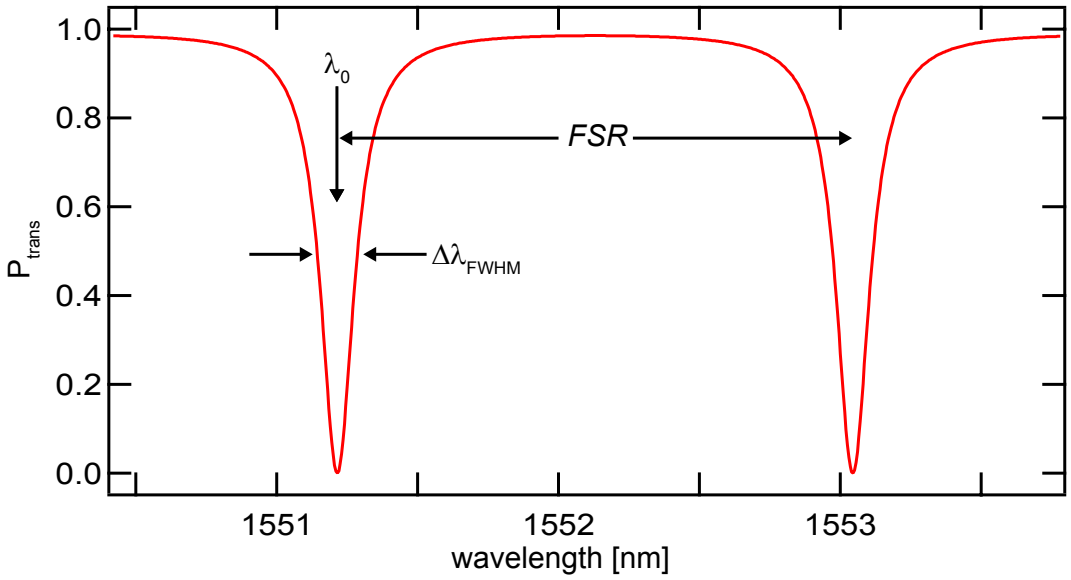

Figure 2.7: **A simulated transmission spectrum of a microring resonator.** In this example, we have simulated the n_{eff} for a range of wavelengths of a 100 µm radius silicon nitride ring with core dimensions of 725 by 1500 nm. We have defined the losses as 17.34 dB cm^{-1} to give a Q_L of about 10,000.

Another, and more common, method of examining the power inside a cavity is to measure the quality factor, Q. There are two definitions for the Q of an

optical resonator, which is a dimensionless parameter, that are equivalent for sufficiently large values.

$$Q = \omega_0 \frac{U}{-dU/dt} \tag{2.40a}$$

$$Q = \frac{\omega_0}{\Delta\omega_{FWHM}} \approx \frac{\lambda_0}{\Delta\lambda_{FWHM}} \tag{2.40b}$$

where U is the stored energy in the cavity and $\Delta\omega_{FWHM}$ is the full bandwidth at half maximum of the transmitted power from equation 2.38 and is referred to as the cavity linewidth. The approximation in equation 2.40b is equivalent to better than one part in Q^2. Therefore, for the large values used in this dissertation, we can experimentally measure Q from the sharpness of the resonance in the wavelength domain. From equation 2.40a, and under real systems where β is complex to include losses, we can also say the Q is related to τ_p, the photon lifetime:

$$Q = \omega_0 \tau_p \tag{2.41}$$

where τ_p arises from absorption, scattering, bending and coupling losses. The Q defined in equation 2.40 takes into account all the losses of the system: from the ring and from the coupling. This is defined as the loaded Q, Q_L, and can be directly measured using equation 2.40b from a measured transmission spectrum such as the one in figure 2.7. We can also define the Q using the parameters from the matrix formalism [36]:

$$Q_L = \frac{\sqrt{ta} L \pi n_g}{(1 - ta)\,\lambda_0} \tag{2.42}$$

and examining solely the losses in the ring we can define the intrinsic quality factor, Q_i, for the resonator:

$$Q_i = \frac{\sqrt{a} L \pi n_g}{(1 - a)\,\lambda_0} \approx \frac{k_0 n_g}{\alpha} \tag{2.43}$$

where the approximation holds assuming low losses and critical coupling (i.e. when the losses in the ring are equal to the coupling losses, $a = t$). We note when

the critical coupling condition is met Q_i is twice Q_L. We define the relationship between these separate quality factors as follows:

$$\frac{1}{Q_L} = \frac{1}{Q_i} + \frac{1}{Q_c} \tag{2.44}$$

where Q_c is the coupling Q. For cases in which we do not have critical coupling, we are still able to calculate the parameters for the matrix formalism, equation 2.32, using equations 2.42, 2.43, 2.44 and the following relations:

$$Q_c = \begin{cases} \frac{2Q_L}{1-\sqrt{T_{min}}} & \text{for } a < t \\ \frac{2Q_L}{1+\sqrt{T_{min}}} & \text{for } a > t \end{cases} \tag{2.45}$$

where T_{min} is the minimum transmitted power at λ_0 from a measurement such as the one in figure 2.7, and the condition for $a < t$ is called under-coupled and $a > t$ is called over-coupled. The coupling strength, κ, is dependent upon the gap, g, shown in figure 2.6 and the wavelength of operation. Going from larger to smaller gaps and from shorter to longer wavelengths increases the coupling. In this way, we can determine if a particular resonance is over- or under-coupled by examining the change in coupling as a function of gap size or wavelength.

So far we have examined the ring properties for a single resonance at λ_0; however, it is of great interest to examine the resonator properties across a broad spectrum for the nonlinear processes discussed later in this dissertation. We define the free spectral range (FSR) as the spacing between adjacent resonances using equations 2.26 and 2.31:

$$FSR^{(\omega)} = (\omega_2 - \omega_1) \approx \frac{1}{r\, d\beta/d\omega} = \frac{c}{r\, n_g(\omega)} \tag{2.46a}$$

$$FSR^{(\lambda)} = \frac{\lambda^2}{2\pi r n_g(\lambda)} \tag{2.46b}$$

where the approximation holds true for small changes in ω of adjacent resonances. Equation 2.46 allows an experimental verification of n_g derived from

simulation.

The final parameter we introduce is the finesse, $\mathcal{F}$, which can be defined as:

$$\mathcal{F} = \frac{FSR^{(\lambda)}}{\Delta\lambda_{FWHM}} \tag{2.47}$$

where the FSR and cavity linewidth can both be experimentally measured or simulated if the losses, coupling coefficients and group index of the ring are known. The finesse can also be related back to the coupling parameters for the low-loss regime. When operating at the critical coupling condition and low loss, from equations 2.33, 2.42, 2.46b and 2.47 the finesse becomes:

$$\mathcal{F} = \frac{a\pi}{\kappa^2} \tag{2.48}$$

and considering equation 2.36 under the same conditions we find:

$$P_{circ} = \frac{a}{\kappa^2} = \frac{\mathcal{F}}{\pi} \tag{2.49}$$

Therefore, simply from the transmission spectrum, we can determine all the key ring parameters presented in this section.

CHAPTER 3

MATERIALS AND FABRICATION

3.1 Introduction

The quality of an optical device is determined by two main factors: the purity of the materials and the fidelity of fabrication. The dielectrics commonly available in CMOS foundries include silicon (Si), silicon dioxide (SiO_2), silicon nitride (Si_3N_4), silicon oxynitride (SiON), high-k dielectrics, and germanium (Ge). For monolithic integration with electronics, we are limited to the use of the above materials. In this chapter we will discuss the relevant material parameters of the films for low-loss waveguides as well as nonlinear optics. We also discuss the fabrication challenges, techniques and methods used for Si_3N_4 optical devices presented in this dissertation.

3.2 Material Parameters

The field of silicon photonics has focused on operation in the near infrared wavelengths of the C-band centered at 1550 nm. In this section we will explore the optical properties of the standard CMOS materials in this wavelength range. For each material we will discuss the material growth and processing, refractive index, transparency window, demonstrated propagation losses and nonlinear properties.

The refractive index of the material comes directly from the linear suscepti-

bility, $\chi^{(1)}$, presented in equation 2.3 and can be found as:

$$n = \sqrt{\epsilon} = \sqrt{\chi^{(1)} + 1} \tag{3.1}$$

with the assumption that $\chi^{(1)}$ is real. If it is a complex number, the real part of $\chi^{(1)}$ should be substituted into equation 3.1 and the imaginary part is proportional to the linear absorption losses, α_L. As discussed in section 2.3, due to material dispersion ϵ is a function of optical frequency and therefore n changes with optical wavelength. To accurately calculate the β values for a waveguide at different wavelengths, we need to precisely know the refractive index at the frequency in question. In order to model $n(\lambda)$, we use the Sellmeier equation which takes the form:

$$n(\lambda) = \sqrt{1 + \frac{A_1\lambda^2}{\lambda^2 - B_1} + \frac{A_2\lambda^2}{\lambda^2 - B_2} + \frac{A_3\lambda^2}{\lambda^2 - B_3} + \cdots} \tag{3.2}$$

where A_i and B_i are coefficients found from experimental measurements.

Since all the materials considered in this chapter are centrosymmetric, the $\chi^{(2)}$ vanishes for the bulk approximation and the lowest nonlinear susceptibility is the $\chi^{(3)}$ which affects the polarization as shown in equation 2.4. In chapter 8, an effective $\chi^{(2)}$ from surface interactions will be discussed but for now this can be ignored. The remaining nonlinear susceptibility gives rise to an intensity dependent refractive index:

$$n(I) = n_0 + n_2 I \tag{3.3}$$

where n_0 is the linear refractive index, I is the optical intensity such that $I = |\mathbf{E}|^2$ and n_2 is the nonlinear refractive index. Using equations 2.4 and 3.3, the relationship between $\chi^{(3)}$and n_2 can be derived as [23, 25]:

$$n_2 = \frac{3}{8n_0}\mathrm{Re}\left(\chi^{(3)}\right) \tag{3.4}$$

Pumping above the half bandgap of a material can lead to two-photon absorption (TPA): the simultaneous absorption of two photons such that the sum of

their energies is greater than the band gap. The imaginary part of $\chi^{(3)}$ is then related to the two-photon absorption parameter, β_{tpa}, defined as [25]:

$$\beta_{tpa} = \frac{3\omega}{4n_0 c}\mathrm{Im}\left(\chi^{(3)}\right) \tag{3.5}$$

3.2.1 Silicon

Silicon has become the workhorse of the microelectronics industry due to its abundance and versatility. The vision of combining photonics with electronics involves leveraging CMOS processing to place silicon waveguides on microelectronic chips [3, 4]. The vision of front-end optical integration would place optics on the same device layer as electronics [37]. On the other hand, back-end integration would require deposited films or wafer bonding [38]. As deposited silicon is amorphous (a-Si) and can be annealed to form polycrystalline silicon (poly-Si), we will consider the properties of these phases of Si as well.

The optical properties of crystalline silicon (c-Si) have been well studied. The refractive index of the film at 1550 nm is 3.45 and the coefficients for the Sellmeier equation can be found in most optical handbooks. Silicon's high refractive index enables the formation of sub-micron waveguides capable of very tight bends when SiO_2 is used as a cladding material. The intrinsic loss of the material can be very low. Since the purity of silicon wafers is very good there should be very few impurities thus minimizing scattering and absorption defects.

The first integrated waveguides using silicon relied on a thick core and a shallow etch to form a ridge waveguide. These waveguides have been shown to demonstrate very low propagation losses on the order of 0.1 to

0.4 dB cm^{-1} [39, 40, 41]. However, light is not tightly confined in these waveguides. Therefore, they are unable to bend sharply and have a lower effective nonlinearity. High confinement, channel waveguides (figure 2.2b) have been demonstrated in silicon with dimensions of approximately 0.25 µm by 0.5 µm. The losses for these waveguides are typically much higher on the order of 1 to 2 dB cm^{-1} [42, 43, 44, 45]. Silicon microresonators have also been extensively investigated with the largest Q for an integrated device being 4×10^5 [46] and for a free-standing disc, 5×10^6 [47].

Silicon also has a large bulk nonlinearity at telecommunications wavelengths, with a value of n_2 measured to be $\sim 4 \times 10^{-14}$ cm^2 W^{-1} [48, 49]. The previously mentioned high-index contrast also enables a very small modal volume which in turn increases the effective nonlinearity as will be discussed in chapter 4. Unfortunately, at telecom wavelengths silicon suffers from two-photon absorption since its gap energy is 1.12 eV. The losses induced by TPA are relatively small, however, the generated carriers lead to free carrier absorption (FCA) which is deleterious to nonlinear processes. Much work has gone into reducing the free-carrier lifetime [50] in order to mitigate such effects.

Most of the work in integrated photonics has until this point focused on the silicon-on-insulator (SOI) platform. SOI is starting to become a popular substrate in the microelectronics industry because it reduces capacitance and resistance compared to bulk-Si CMOS. However, the SOI used in photonics in general requires a buried oxide (BOX) layer of greater than 1 µm (including all the devices with the lowest propagation loss [39, 40, 41, 42, 43, 44, 45]), as opposed to the thinner BOX layer (about 100 nm) used for electronics. An additional constraint to front-end integration is the actual chip space required for

photonic devices compared to electronics devices. Nevertheless, recent works have explored the possibility of using electronic substrates by a clever undercutting method in thin-BOX, SOI wafers [51] and bulk Si wafers [52, 53], as well as a local oxidation method in bulk Si wafers [54].

Although the optical quality of poly-Si is poorer than c-Si, much work has been done to demonstrate devices suitable for integrated photonics [55, 56]. The main advantage of poly-Si over a-Si is the electrical properties which are sufficient to make many of the electro-optic devices that make silicon photonics such a promising field. Deposited a-Si must be hydrogenated in order to achieve low waveguide losses [57]. In these waveguides, the nonlinearity has been shown to be very strong [58, 59], however due to the poorer electrical properties, there is no easy way to extract generated carriers.

3.2.2 Silicon Dioxide

The second material we will examine is silicon dioxide, SiO_2. The development of silica optical fibers in the last fifty years has dropped the optical propagation loss to $0.2\,\mathrm{dB\,km^{-1}}$. More recently, high-$Q$ resonators using silica have been demonstrated with microspheres [60] and on-chip with microtoroids [61]. Some work has been done on doped-SiO_2 as a core material for integrated waveguides [62, 63], but it is normally used as a cladding material due to its low refractive index, 1.44 @ 1550 nm, and low optical losses. Although silica is transparent down to the ultraviolet, it begins to absorb at longer wavelengths beyond 2.5 μm [64].

The highest quality of SiO_2 available on-chip is thermally grown from bulk

Si. The growth kinetics are well-studied and rates are dependent on the atmosphere (dry, O_2, or wet, H_2O) and temperature of the furnace process [65]. The BOX layer of SOI wafers have thermally grown oxide, however, for the cladding layer this is normally impossible since growth of SiO_2 would consume the Si device layer. An oxide layer can be grown from Si_3N_4 [66, 67] as well, but this process is very slow. SiO_2 can also be deposited through chemical vapor deposition (CVD). Both low-pressure (LPCVD) and plasma-enhanced (PECVD) recipes are capable of producing high quality films. We will discuss this process in more detail in section 3.3.4.

The band gap for SiO_2 is greater than 9 eV and therefore it does not suffer from significant nonlinear losses [25]. The strength of the silica nonlinearity is more than 2 orders of magnitude smaller than silicon estimated at $2\,cm^2\,W^{-1}$ [25]. However, because of low propagation losses, negligible nonlinear losses, and high-Q resonators, SiO_2 has been a popular platform for demonstrating many third-order nonlinear optical processes in fiber and resonators.

3.2.3 Silicon Nitride

Silicon nitride is a CMOS-compatible material that is commonly used in the microelectronics industry for masking [65]. The material also has a few notable ceramic forms that are used for their mechanical strength and heat resistant properties, most commonly in turbine engines [68]. There are a number of methods for preparing the material including reaction bonding, hot-pressing or sintering, nitridation of Si, sputtering, evaporation and CVD [69]. Dense and bulk Si_3N_4 takes two crystalline forms with similar but slightly different prop-

erties [68]. However, the CVD deposited thin films used here (with techniques described in section 3.3.1) are amorphous in nature [68, 69]. The film can be oxide-rich, creating SiON, silicon rich, SiN, or stoichiometric, Si_3N_4. The optical properties of the material are less well known than for SiO_2 and Si. Philip was the first to perform measurements of the dielectric constants [70], but no data exists for energies below 1 eV. In section 4.2, we describe measurement for n in the c-band and the calculation of Sellmeier coefficients. Additionally, the deposition chemistry leads to dangling H and O bonds with the Si and N in the films. These bonds lead to absorption peaks near the c-band with the strongest centered at 1520 nm [71, 72] and can cause excess propagation losses for infrared waveguides.

Previously, silicon nitride waveguides have been made using both LPCVD and PECVD for operation at both visible and infrared. The earliest work examined slab waveguides in the visible for LPCVD films [73] with losses of 0.1 dB cm^{-1} and PECVD [74] with losses near 1 dB cm^{-1}. The first measurement of Si_3N_4 waveguides in the c-band was performed by Henry et al. [75], who used LPCVD ridge waveguides to show losses down to 0.3 dB cm^{-1} after an annealing step to reduce the absorption from the dangling Si-H bond.

There has been renewed interest in Si_3N_4 as the guiding material for integrated photonics over the past decade. The first channel waveguides used thin LPCVD films and demonstrated sub 1 dB cm^{-1} in the visible [76]. Other groups have grown LPCVD films as thick as 250 nm before observing cracking of the films due to stresses [77]. Losses as low as 0.1 dB cm^{-1} have been shown in 200 nm thick films at 1550 nm [78] after high temperature annealing. In these waveguides, the optical mode is very delocalized and requires a thick BOX

layer to prevent leakage into the Si substrate. Thicker films have been grown in PECVD by playing with the deposition frequencies [79]. Losses in the infrared for a waveguide core of 400 nm were shown to be 2.1 $\mathrm{dB\,cm^{-1}}$ [80]. Due to the low optical losses, high-Q resonators have been shown in the visible [81, 82] and in the infrared [83].

The material nonlinearities have not been well-characterized. Since the band gap for Si_3N_4 is generally between 4.5 and 5 eV [84], depending on deposition, we can assume negligible TPA for infrared light. Since it is an electrical insulator, the material does not support free-carriers and FCA is not a concern. The strength of n_2 was not known until very recently. In section 4.4, we will explain in detail why it is expected that the nonlinear strength of Si_3N_4 should be between that of Si and SiO_2 from the estimate given by Miller's rule [85]. Concurrently with measurements made for this dissertation, a value of $2.5 \times 10^{-19}\,\mathrm{m^2\,W^{-1}}$ was reported for the n_2 of Si_3N_4 [86]. The measurements shown in section 4.4.2 are in good agreement with this value.

3.2.4 Materials Summary

We present a summary of the key material parameters presented in sections 3.2.1 to 3.2.3 in table 3.1. Although there are other materials available for use which we have not covered in detail, these are the most commonly used in the Si photonics community. We choose to use Si_3N_4 as the core material because it comprises the best attributes of Si and SiO_2 for integrated nonlinear optics. As we will show, the low propagation losses and negligible nonlinear losses of Si_3N_4 outweigh the stronger nonlinear parameter and tighter confinement in Si

waveguides.

material	Si	SiO_2	Si_3N_4
n @ 1550 nm	3.45	1.46	1.99
E_g	1.12	~ 9	~ 5
Transparency window (μm)	1.1-9	.13-3.5	.25-8
β_{tpa}(cm GW^{-1}) @ 1550 nm	0.79	<< 0.01	~ 0
n_2 (m^2 W^{-1}) @ 1550 nm	$(4-9)\times10^{-18}$	$(2-3)\times10^{-20}$	2×10^{-19}

Table 3.1: Relevant optical parameters for CMOS-compatible materials.

3.3 Fabrication

Our optical devices are fabricated on 4″ silicon wafers which are much less expensive than the custom-made SOI used for silicon waveguides. We grow a thermal oxide on the virgin Si wafer. Using a wet oxidation process at 1200 °C, a 4 to 5 μm BOX layer is formed. This thickness is sufficient to optically isolate the waveguide from the silicon beneath. With the capacity of the furnace tubes, the oxidation can be done for 100 wafers at a time which drives down processing costs.

3.3.1 Deposition

We choose to use LPCVD to form our Si_3N_4 core layer. Although we must be careful about film stress and cracking, LPCVD gives the lowest optical losses demonstrated. We use a horizontal loading furnace tube and load the target 100 mm wafers with the thick BOX layer facing the back of the tube single-spaced with two buffer wafers on either side. The deposition takes place at

800 °C under 200 mTorr pressure. The two reacting gases are ammonia, NH_3, and dichlorosilane (DCS), SiH_2Cl_2 which combine to form Si_3N_4, H_2 and HCl. For the deposition step the flow rate of NH_3 is 196 standard cubic centimeters per minute (sccm) and 60 sccm for the DCS. The deposition process was optimized for the microelectronics industry, which requires films which are a maximum of 200 nm. When thicker films are deposited and annealed, the stresses lead to cracks [75, 87, 88] and make the films optically unusable. From our testing, we find 400 nm to be the thickness limit before cracking for our modified LPCVD process. The deposition rate drifts run to run but is close to 3.4 nm/min. A typical deposition of 100 min yields films between 330 and 350 nm.

As discussed in section 5.3, we require a thicker Si_3N_4 core than is possible from a single deposition. To overcome the cracking limit, we employ a thermal cycling technique [89, 90]. After the initial deposition of between 350 and 400 nm, we allow the wafers to cool to room temperature. After a clean, the wafers are annealed at 1200 °C in an ambient N_2 environment for 3 hours. The anneal serves two purposes for improving the optical quality of the film. First, the deposition process described above results in the dangling H bonds mentioned in section 3.2.3. The high temperature anneal serves to outgas any excess hydrogen or oxygen in the film leaving a more stoichiometrically pure Si_3N_4. Second, the anneal also reduces stress which prevents the deposition of thicker films. After allowing the wafer to cool again, we repeat the LPCVD deposition so that the total thickness of Si_3N_4 reaches the design target. In principal this process can be repeated, however, the thicker the film the more likely the wafer is to break or form cracks during the anneal step.

3.3.2 Lithography

Lithography is the process of transferring a designed pattern to the device layer. For microfabrication the two major types of lithography or photolithography and electron beam lithography (e-beam or EBL). Both lithographies require the target wafer to be patterned with a resist (photoresist or e-beam resist respectively) which is then exposed to the design. In photolithography, a pattern is written on a fused quartz reticle patterned with chrome to serve as a photomask with alternating transparent and blocked sections. The features written on this mask are much larger than the final designed features. Using a projection system called a stepper, UV light is used to expose the resist on the wafer. E-beam lithography does not require the patterning of a separate mask. The tool uses a collimated beam of electrons to expose the resist in a direct pattern write.

The advantage of using photolithography is the fast speed and small cost associated with transferring a pattern from a mask to a wafer. However, the drawbacks to using photolithography are limited mask flexibility and the minimum feature size of 0.5 µm (for the i-line process). E-beam allows a great amount of flexibility with patterning a wafer because of the direct write capabilities. Feature sizes can also be much smaller than with photolithography. Minimum line sizes depend on the specific resist used, but features less than 100 nm wide are routinely possible. However, writing times for e-beam can be very long depending on the pattern area, dose and current used. This can lead to very high production costs and potential drift in tool performance during the course of a single write. For the research purposes pursued in this dissertation, we choose to use e-beam because of the flexibility, feature size and resolution advantages over photolithography.

In order to design our pattern for lithography, we use computer aided design (CAD) to draw structures: rectangles for waveguides, circles for rings or discs, and writing to number guides and mark chips. The most effective way to ensure the fidelity of our designs is through scripting. For the waveguides written here this was done using custom macro for the commercial software L-Edit and later through the open-source gdspy package. An example layout is shown in figure 3.1. The pattern is written to the graphic data system II (GDSII) format, a standard in the microelectronics industry. We then use LayoutBEAMER software to transfer the GDSII pattern into the file format the e-beam tool uses.

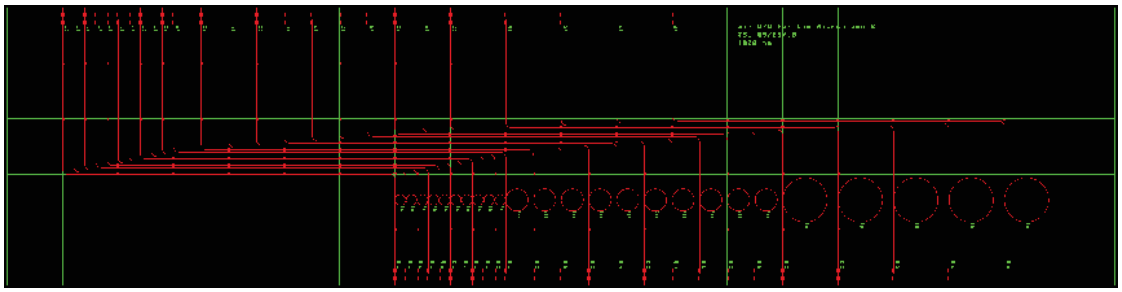

Figure 3.1: **An example layout for e-beam writing of devices.** The green boxes represent the individual e-beam fields. The red lines are the waveguides and ring resonators. There is also writing in green to label the waveguides, ring radius, gap distance and waveguide width. The large writing in the top right corner identifies the chip.

We use the JEOL-9300 tool which is a 100 keV e-beam tool. The current can be adjusted from 500 pA to 10 nA. Larger currents lead to larger spot size for the tool and worse resolution. For our fabrication, we set the current to 2 nA. The dose delivered to the resist depends on the resist used and is defined in terms of μC. The green boxes shown in figure 3.1 represent the field boundaries of the tool. The field size determines how much area the tool writes before it moves the location of the beam. For the JEOL-9300 this is 1 mm. In order to ensure the highest quality devices, we make sure rings are written in a single field to

avoid stitching errors. Stitching errors, such as the one shown in figure 3.2, occur at the field boundaries when the tool's position drifts over time and causes misalignment of the pattern at these points. They can also arise from the accumulation of charge at the field boundaries which later in the write deflects the beam.

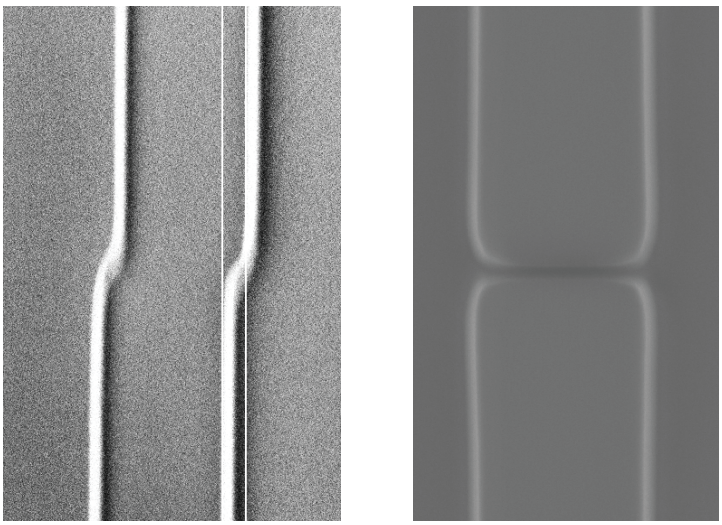

Figure 3.2: **Stitching error at an e-beam field boundary.** The stitching results in misalignment of the waveguide across the boundary. The offset can result in a shift in the waveguide center as shown on the left, or a complete gap formation as shown on the right. In both cases, the waveguide experiences high optical loss.

For our processing we choose to use MaN-2405 resist. Before applying the resist, we clean the wafer using either a MOS clean or piranha clean (H_2SO_4 and H_2O_2). We then spin Surpass 3000, an adhesion promoter, on the wafer to ensure the resist will not peel off. We coat the wafer with MaN-2405, spinning at 1000 rpm for 30 s to achieve a resist thickness of approximately 700 nm. The thickness is necessary to survive the etch process, but also limits the smallest feature size because at high aspect ratios the resist can collapse. We then pre-bake the resist for 1 min at 95 °C. In an attempt to mitigate charging at field boundaries, we spin a chemical e-spacer on the wafer at 2000 rpm for 30 s prior to exposure.

To expose the resist, we use a dose between 900 and 1000 µC. The resist is developed using a Hamatech spin developer with MiF-726 for 90 s. Before etching, we do a descum of the wafer to clean small amounts of resist that were not removed with the developer. We also do a hard bake of the resist at 135 °C for 5 minutes. The hard bake serves to increase the selectivity of the resist during the etch process. Baking at a higher temperature can cause the resist to reflow. Although this process has been shown to reduce waveguide losses [89, 91], it can cause mask erosion during etching which limits the control over waveguide dimensions and leads to trapezoidal waveguide cross-sections.

3.3.3 Etching

Once lithography is completed, we are left with a resist defined pattern on top of our Si_3N_4 film. In order to define channel waveguides, we need to etch the exposed portion of the film. The two principal methods for etching are wet and dry etching. For Si_3N_4, wet etching in hot phosphoric acid, H_3PO_4, has been commonly used with a rate of 10 nm/min depending on concentration and temperature [92]. However, wet etching is generally isotropic and will undercut the Si_3N_4 under the resist mask. Therefore, we choose reactive-ion etching (RIE), which is an anisotropic dry etch technique that will define rectangular waveguides. The principal etch gases for Si_3N_4 RIE are the fluorine containing CHF_3 [93, 94], CF_4 [95] and SF_6 [96]. The gases can be combined with levels of O_2, CO_2 or H_2 to adjust the process etch rates or selectivity.

For devices processed here, we use a CHF_3/O_2 etch chemistry with an inductively couple plasma (ICP)-RIE etcher using the PlasmaLab Systems Oxford

100 tool. In this tool there are two radio frequency (RF) sources; one is inductively coupled to the low-pressure gases, and the second is connected to the sample chuck. The strong RF field on the gases creates a high density plasma by causing the CHF_3 to be stripped of electrons and disassociate into F and CHF_2^+ ions among other possibilities. The reactive species are accelerated into the oppositely charged sample wafer and modify the surface chemistry. The surface reactions that etch Si_3N_4 are [93, 94]:

$$Si_3N_4 + 12F \rightarrow 3SiF_4 + 2N_2 \tag{3.6a}$$

$$Si_3N_4 + 12CHF_2^+ \rightarrow 3SiF_4 + 6N_2 + 6H_2 + 12CF \tag{3.6b}$$

with other combinations possible for the CHF_2^+ reactions [93] which give less stable fluorosilanes than the tetrafluorosilane, SiF_4 [94]. The addition of O_2 to the etch gases gives a few added benefits. It increases the concentration of reactive fluorine at the wafer surface by reacting with CHF_3 to form more volatile compounds such as CO and CO_2 [94]. In doing so it helps block the formation of polymers at the surface which slow the etching time and are deleterious to optical performance. O_2 also increases the selectivity of the etch to the e-beam resist. This prevents mask erosion which can give severely angled sidewalls for the waveguide.

In our process we flow 52 sccm of CHF_3 with 4 sccm of O_2. We etch the wafer for a maximum of five minutes at a time to prevent the excessive formation of polymers on the wafer surface. In between etches, an oxygen plasma clean of the chamber is performed. Depending on the thickness of the Si_3N_4 film, we may have to perform multiple etch steps given the etch rate is usually near 90 nm/min. For films greater than 600 nm thick, we also perform a back-side etch of the wafer to prevent stresses of the wafer which can lead to cracking

during the final anneal step. A cross-section SEM is shown in figure 3.3. In this case, the wafer underwent the reflow process previously discussed and mask erosion caused the sidewall angle to be greater than 20°. More recently, this angle has been decreased to less than 10°. As mentioned in section 2.4.3, we are accurately able to model these shapes so the consequences are manageable. Still, for some applications more vertical sidewall angles are necessary and recent work has shown this is possible with an improved etch process [97].

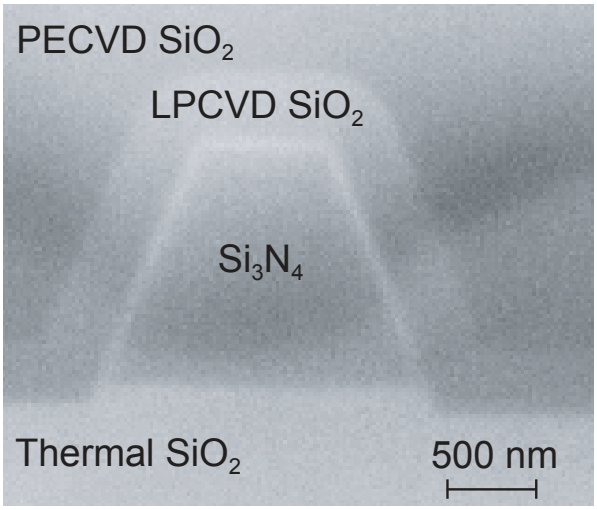

Figure 3.3: **Micrograph of a Si_3N_4 waveguide cross-section.** The sample was prepared using a Transmission Electron Microscope to view the waveguide profile. We can see a severe slope to the sidewalls due to a combination of the etch process and mask erosion.

3.3.4 Cladding

After etching, we strip the remaining resist using an asher in which oxygen plasma removes the resist but leaves the substrate untouched. We are left with exposed Si_3N_4. Since the second deposited layer has not been annealed, we repeat the thermal annealing step from section 3.3.1 on the unclad channel waveg-

uides. In order to form buried channel waveguides we must clad the material with SiO_2. We are unable to use thermally grown SiO_2 for the top cladding material as is used with the substrate. In order to make symmetric waveguides it is ideal that we then deposit a material which is as close in index to the thermally grown SiO_2 as possible. We use both methods of CVD for the cladding mentioned in section 3.2.2.

The LPCVD SiO_2 is called high-temperature oxide (HTO). HTO is deposited by the reaction of 196 sccm N_2O with 66 sccm DCS at 800 °C under pressure of less than 100 mTorr. The deposited film is conformal to the surface of the wafer which is essential for filling in small gaps between waveguide and resonator. The quality of HTO is very high, with an index profile close to the thermally grown SiO_2. Unfortunately, the deposition rate is very slow, usually around 1 nm/min. Because of the cost associated with long use of the furnace tube, we generally deposit between 250 and 500 nm of HTO on the waveguides as shown in figure 3.3. This layer is thick enough to fill in most coupling gaps and since the mode is tightly confined there is little interaction of light beyond the HTO film.

In order to finish cladding the waveguides, we use a PECVD SiO_2. This process is done at a lower temperature, 400 °C, and the deposition rates, 120 nm/min, are much faster than HTO. In the PECVD chamber, 18 sccm SiH_4 and 1800 sccm N_2O are flown into the chamber and a 13.56 MHz, 100 W RF power source induces the plasma. The ions disassociate and are recombined on the film. Unlike HTO, the PECVD SiO_2 is not conformal to the surface of the wafer and can lead to air gaps at the interface of the film and waveguides. Additionally, the index of the film is slightly higher than thermally grown SiO_2

because it is silicon rich. At the stage of our fabrication process in which we use PECVD SiO_2, these factors are unimportant due to the HTO already deposited on the film.

3.3.5 Chip Processing

Following cladding, the waveguides are fully formed and require no further processing. In order to test the devices, we need to cut out the individual die on the wafer. We cover the wafer with a photoresist to protect it while dicing. We then use a silicon blade dicing saw to very carefully cut through the facets of the chips. The dicing step can be critical to insertion losses of the device. Each chip can then be cleaned and tested directly or the facet may be polished to improve coupling efficiencies. We use either a special type of slurry or soap as lubrication while using diamond polish pads of various roughness loaded on a polisher typically used for TEM sample preparation. The final result is a very smooth facet and ideally low insertion loss. In some cases the polished facets cause high back reflections and a fabry-pérot modulation of the transmission spectrum.

CHAPTER 4

SILICON NITRIDE WAVEGUIDES: LOSS REDUCTION AND MEASUREMENT OF THE NONLINEARITY

4.1 Introduction

The key parameters for determining the strength of nonlinear interactions are phase-matching, the interaction length, the material nonlinearity, and the optical intensity. In this chapter, we discuss the basic material properties needed for proper design and simulation of our devices. First in section 4.2, we discuss the measuring of the refractive index and determination of Sellmeier coefficients. Precise knowledge of the material dispersion is necessary for device design to meet the phase-matching condition, discussed in section 5.3. There are many ways to calculate the nonlinear refractive index for bulk materials, most notably a z-scan [23, 98]. However, for thin films the measurement is not straightforward. In section 4.4 we will discuss self-phase modulation (SPM) in Si_3N_4 waveguides in order to calculate the material n_2.

Waveguide losses can be a limiting factor in nonlinear interactions, as well as propagation length and resonator quality factor. The propagation loss directly determines the effective length [25] of a device, and determines the power build-up in a resonator. In section 4.3, we describe methods for measuring the propagation loss of waveguides, measure the losses for a number of film thicknesses and discuss methods for loss reduction.

4.2 Refractive Index Measurements

In order to accurately model our devices, we need to know the refractive index of the film we use. The previous optical data given for Si_3N_4 does not include energies lower than 1 eV [70]. Additionally, given the many different methods for deposition can yield slightly different chemical compositions it is important for us to determine the material refractive index for our films. We do this using ellipsometry which analyzes the polarization changes in light reflected from the sample across a broad wavelength range. From the ellipsometric data we can fit equation 3.2 to get Sellmeier coefficients for out nitride films. Figure 4.1 shows the fit curve and the measured data points.

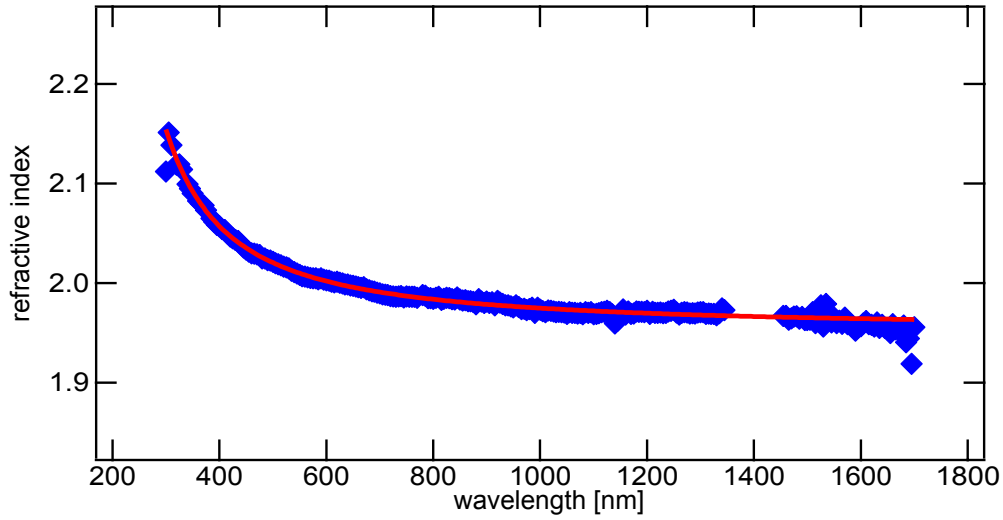

Figure 4.1: **Ellipsometric data points and Sellmeier fit for Si_3N_4.** The blue dots are the data points for the refractive index. The red curve is generated from Sellmeier coefficients determined by a fit to the measurement.

4.3 Waveguide Losses

Losses arise from scattering, absorption, bending, and defects. Scattering loss occurs at the interface between the core and cladding. When the interface is not perfectly smooth light will scatter as Δn^2 and the inverse of the wavelength squared [99, 100]. The sidewall smoothing techniques of oxidation [101], resist reflow [47, 89], or improved etch chemistry are attempts to mitigate scattering loss. Absorption losses arise in two ways. First is the intrinsic absorption loss of the material, which for light at frequencies below the bandgap comes entirely from defects to the material. The second cause of absorption loss is from surface states at the interface between core and cladding [47, 102]. When a waveguide is bent, there is the potential for radiation loss. The sharper the bend and the looser the confinement, the larger the leakage of light. The bend loss becomes a major concern when considering the minimum size resonators achievable on-chip. For the waveguides made here, we can also have random losses across the waveguide from defects such as film cracks mentioned in section 3.3.1 and stitching spots as shown in figure 3.2.

There are a few well known methods for measuring the propagation loss of optical waveguides. The first is the cut-back method. This method was originally developed in fiber where the length of the fiber was literally cut-back as losses were continuously measured. In this way, an accurate per length loss measurement can be calculated. In integrated structures, where it is not straightforward to reduce the length of the device by a known quantity, the cut-back method involves measuring many waveguides of varying length. It is important to have enough waveguides to overcome any random defects which may influence the loss measurement in a single structure. As shown in equation 2.43,

a measurement of a resonator Q can give a value for propagation loss. If the radius is large enough that bending loss is not a concern, this value is assumed to be the same for a straight waveguide of the same cross-section. Propagation loss can also be determined by measuring the scattering of light from a top view of the waveguide using an IR camera [103]. Here the camera is calibrated to the scattered light at the input, and then measures the scattered light again at various points along the length of the waveguide. The light detected by the camera is numerically evaluated to give a normalized propagation loss. The final method for calculating losses is the Fabry-Pérot method [104]. In this method, the waveguide facets act as mirrors and the Fabry-Pérot maximum and minimum are measured to derive the losses in the waveguide. In order to calculate propagation losses in our devices, we focus on the first two methods: cut-back and resonator.

4.3.1 Cut-Back Method

The insertion loss from input to output of an integrated photonic chip can be broken up into coupling loss and propagation loss. The cut-back method enables us to calculate and separate these losses. The method assumes that the coupling loss into each waveguide is the same, and that propagation losses are constant with distance (i.e. they are not dominated by point defects). As mentioned in section 3.3.1, the LPCVD Si_3N_4 films had previously been shown to have the best losses but a cracking limit of 400 nm. In this section, we show losses for three film thicknesses: 200 nm, the thickness of the best previous low loss demonstrations [78]; 400 nm, the thickest single layer deposited films; and 725 nm to show that we can break the film stress limit without suffering severe

optical losses.

The basic test-setup for optical devices includes an input tapered fiber, a chuck holder for the chip and an output collection lens. A source (single frequency or broadband) is sent through polarization paddles to select either TE or TM light to couple into the chip. In this section, all measurements are done for the TE polarization except where mentioned. The fiber holder is set on a stage with three axis piezo-control to very carefully align the fiber to the chip facet. The chip is placed on a chuck, which sits on a rotation stage, using double-sided tape and the edge facet is aligned perpendicular to the fiber. Output coupling can be done in two ways: mirroring the input fiber coupling, or using a lens to collimate the output beam. For the propagation loss measurements, the output is collected with a lens and sent to a power meter. A polarizer can be placed in between the output and the power meter to check the polarization. The measurements are normalized to the power when the chip is not in the setup and the fiber output is coupled directly to the lens.

We pattern waveguides on the 200 nm films with widths of 1.1, 1.8 and 2.2 µm and variable lengths between 1 and 4 cm. The data is shown in figure 4.2 with large optical losses in comparison to previous results. The higher than expected losses could come from a few areas. First, since the loss decreases with width, the etch chemistry for these first generation of waveguides was probably not optimized leaving a rougher sidewall and inducing more loss. Second, the confinement in such thin waveguides is very poor. Therefore, at waveguide bends, a significant portion of the mode will overlap with the sidewall (exacerbating the deleterious effects of the poor etch), and radiation could cause more loss than theoretically expected.

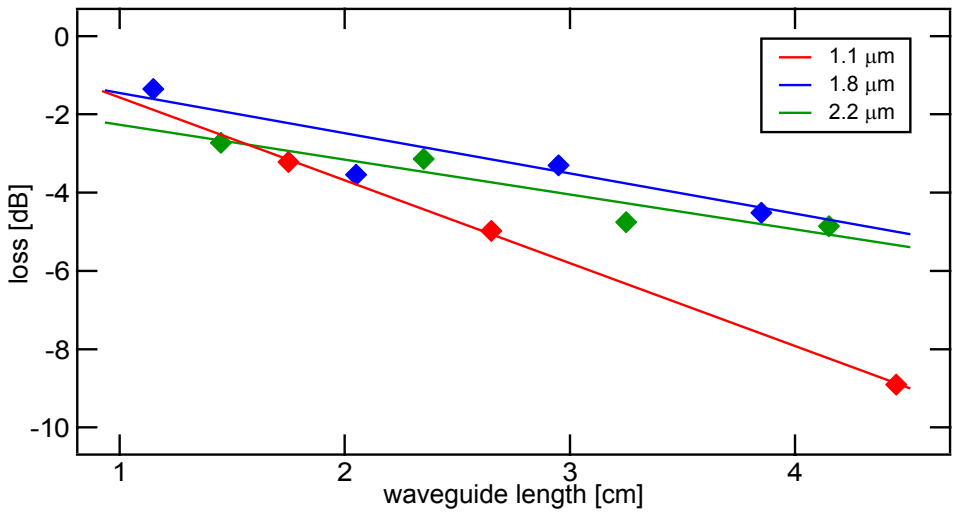

Figure 4.2: **Propagation losses for 200 nm thick waveguide of varying widths.** The losses decrease for the wider wavguides but are still 2.1, 1.0 and 0.9 dB cm^{-1} for the 1.1, 1.8 and 2.2 μm wide guides respectively.

We push the film deposition to the cracking limit to get a Si_3N_4 core thickness of 400 nm. We pattern waveguides 1.5 μm in width and of varying lengths in a paper clip formation. The propagation losses for these devices is 1 dB cm^{-1} as shown in figure 4.3. For these devices, we do not have to worry about increased losses at the bends because the larger core gives a tighter confinement. The results for films of this thickness are noisy because cracks that develop in the film cause point defects in the waveguides. The coupling loss for this device can also be calculated from the y -intercept of the fit. We calculate this value to be 5 dB per facet.

The multilayer deposition process described in section 3.3.1 enables Si_3N_4 films greater than 400 nm. The major challenge in processing these films was to ensure propagation losses did not dramatically increase. The concerns include excess losses caused by the interlayer boundary, etch mask erosion and film frailty for processing. In order to achieve large waveguide lengths while main-

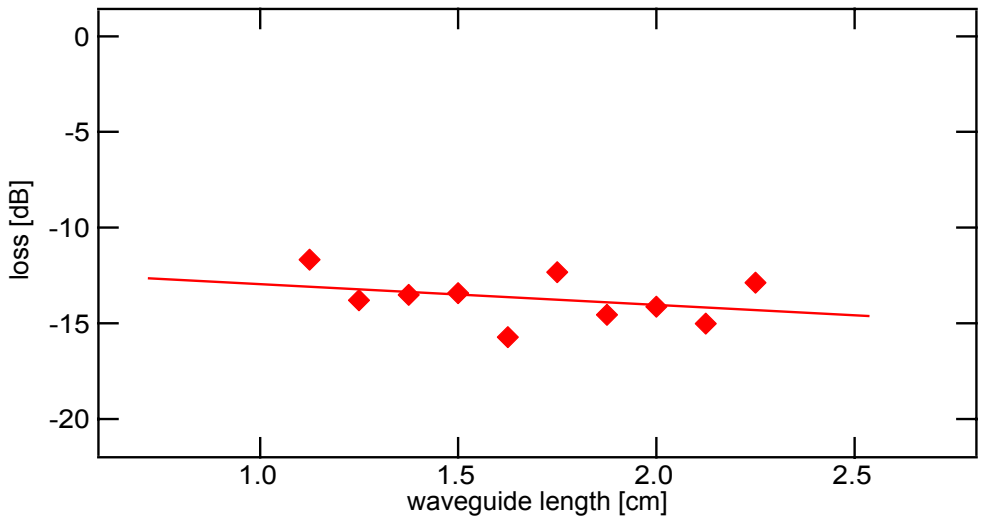

Figure 4.3: **Propagation losses for 400 nm thick waveguides.** The losses are shown for 1.5 µm waveguides. The linear fit gives losses of 1 dB cm^{-1} with coupling loss of 10 dB.

taining a small footprint, we designed spiral waveguides shown in figure 4.4. The design has the added benefit of avoiding stitching errors from the e-beam write.

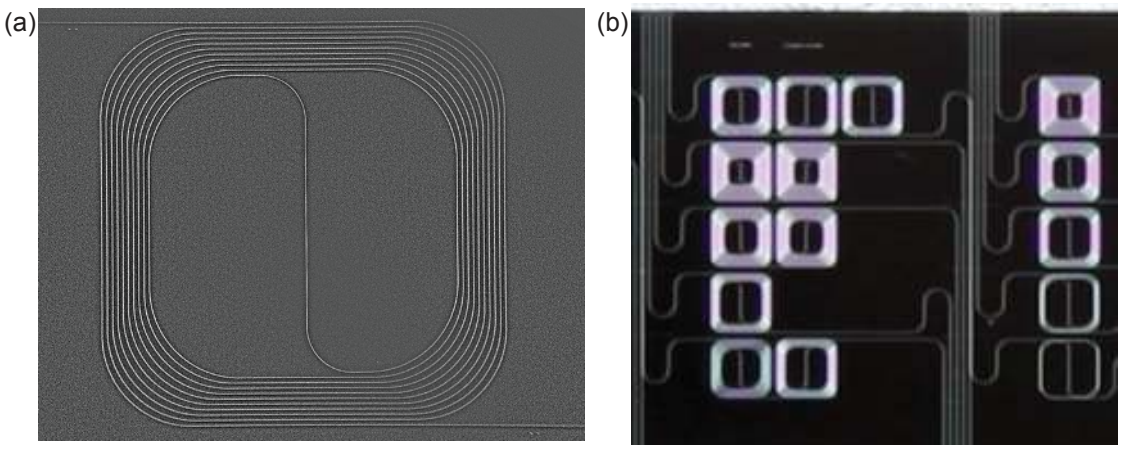

Figure 4.4: **Spiral designs for small footprint long waveguides. a.** A scanning electron micrograph of a single spiral. The device is contained entirely within an e-beam field. **b.** A photograph of an integrated photonic chip, showing many different spirals with waveguides as long as 25 cm.

We pattern 1.5 µm wide waveguides on the 725 nm films. The waveguides vary in length from 1 to 10 cm. The losses are plotted in figure 4.5 and are measured to be 0.51 dB cm^{-1} with a coupling loss of only 3 dB. The improvement in losses compared to previous efforts on thinner films is due to improved processing for deposition, patterning and etching. Because with thicker core layers the light is more confined to the Si_3N_4 and the phase-matching conditions can be met, the waveguides from these results are used for the nonlinear experiments discussed in chapter 5.

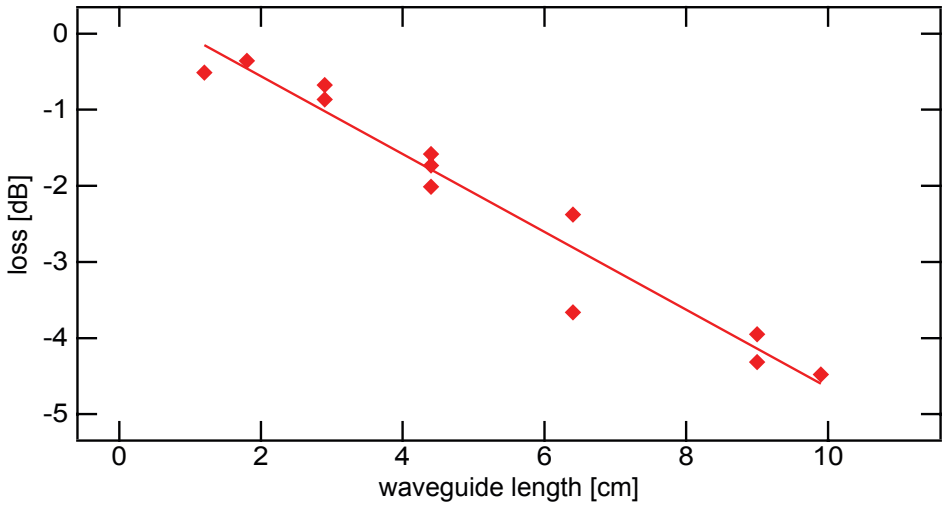

Figure 4.5: **Propagation losses for thick film Si_3N_4 waveguides.** Here we plot the losses for waveguides with a 725 by 1500 nm cross-section. The losses of 0.51 dB cm^{-1} are the first demonstration of low-loss, high-confinement Si_3N_4 waveguides at telecommunications wavelengths.

4.3.2 Resonator Losses

The second method for loss calculation is from the transmission spectrum of microring resonators. From equation 2.43, the intrinsic Q of a device is directly related to the propagation loss. The transmission spectrum of a device gives

Q_L from equation 2.40b and the 3 dB linewidth of the resonance. With accurate knowledge of this value, the normalized minimum transmission and the coupling state (over-, under- or critical-coupling), we can calculate Q_i and therefore the losses.

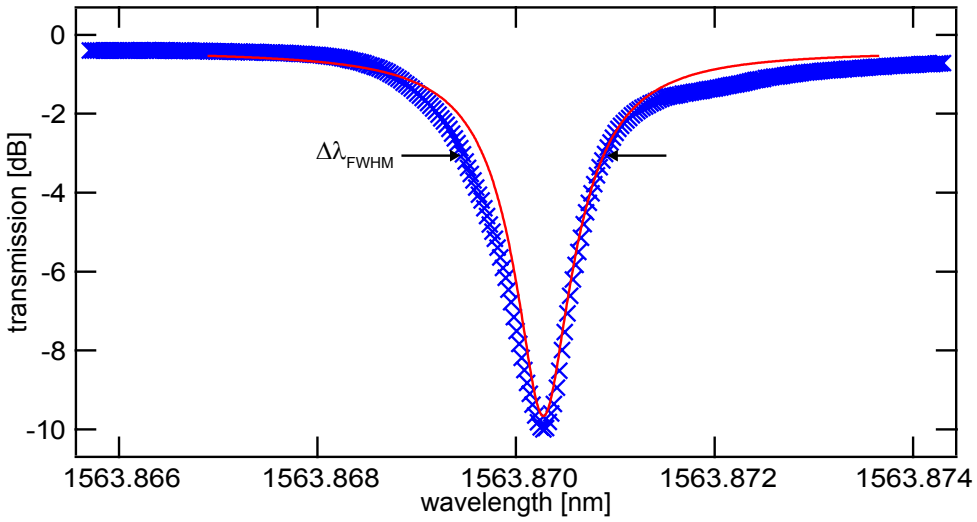

Figure 4.6: **Transmission spectrum for a high-Q resonator.** The blue x's are measured data and the red curve is a Lorentzian with parameters fit to the data. The linewidth of the device is 1.2 pm which gives a Q_L of 1.23×10^6.

In figure 4.6, we plot data from a spectral scan of a measured resonance. We fit the parameters of sample Lorentzian until we get good agreement with the measurement. When a ring is under-coupled, backscattering causes the clockwise and counter-clockwise modes to split. When this splitting is large, the resonance peaks separate into two distinct lines. However, in this case, the modes are nearly degenerate and causes only slight broadening of the measured linewidth. We can see the roll-off from the fit is not nearly as sharp as the measurement. Therefore, we can say the Q of the fit is the minimum for the actual resonator and put an upper bound on waveguide losses. For this case, the intrinsic Q is 3.1×10^6, which gives from equation 2.43 a loss of less than

$0.11\,\mathrm{dB\,cm^{-1}}$. By a careful analysis of the change in resonator linewidth as a function of power, a differentiation between the scattering loss and absorption loss can also be made [89, 105]. For our Si_3N_4, we have previously shown that for high-Q resonators roughly half the loss can be attributed to each factor [89].

4.4 Material Nonlinearity

As discussed in section 3.2, the nonlinear refractive index is related to the real part of the material parameter $\chi^{(3)}$. For materials in which the nonlinearity has not been measured, an accurate estimate can be made based on the linear refractive index [85] or the band gap of the material [106]. A derivation of Miller's rule for calculating n_2 in SI units is given:

$$n_2 = \frac{160\pi^2}{cn_0^2}\left[\chi^{(1)}\right]^4 \tag{4.1}$$

where $\chi^{(1)}$ is in electrostatic units. From equation 4.1, we derive a theoretical value for n_2 at 1550 nm to be $4 \times 10^{-19}\,\mathrm{m^2\,W^{-1}}$. A plot showing Miller's rule as a function of index is shown in figure 4.7*. The measured values for various glasses are plotted against the fitted rule and show good agreement. We have also delineated where Si_3N_4 falls on this curve.

The standard technique for measuring the real and imaginary parts of $\chi^{(3)}$ in bulk materials is the z-scan technique [23, 98]. In thin films a z-scan becomes impractical and different techniques must be used to determine the n_2 and β_{tpa}. In other material, self-phase modulation has been used to determine these values for waveguides [107, 108, 109, 110]. Here, we follow a similar approach and calculate n_2 at 800 nm.

*The figure is adopted with permission from [85]

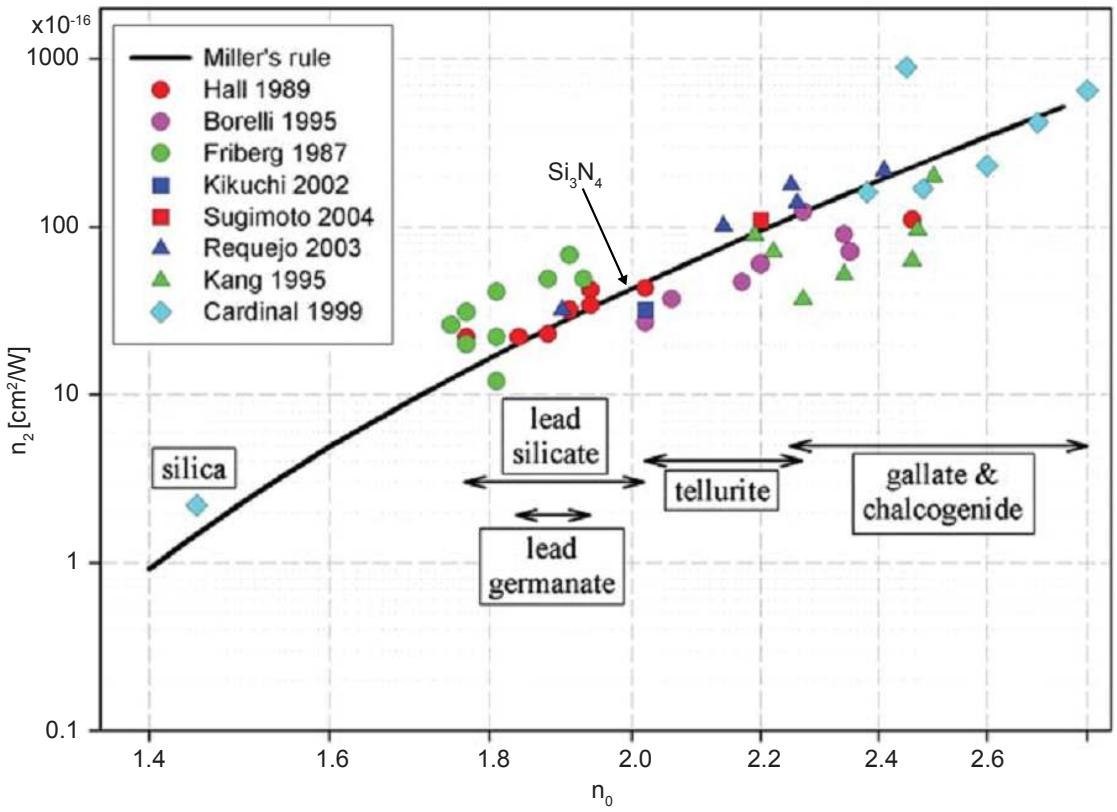

Figure 4.7: **Nonlinear refractive index as a function of linear refractive index for a number of glasses.** This figure plots the n_2 for a number of glasses. The solid curve is a plot of Miller's Rule, equation 4.1. We have pointed out where Si_3N_4 would fall on the theoretical curve.

4.4.1 Self-Phase Modulation

Self-phase modulation (SPM) arises from the nonlinear phase-shift induced by the $\chi^{(3)}$ susceptibility with strong optical intensities. For an optical pulse, this instantaneous phase delay leads to an intensity dependent spectral broadening of the input. By measuring the broadening for different intensities and calculating the phase shift, we are able to use equations 4.3 and 4.4 to determine n_2 for Si_3N_4.

We performed the experiments on the waveguides measured to calculate

losses for 200 nm films from section 4.3.1. The optical source is a titanium sapphire pulsed laser system. The repetition rate is 86 MHz and the pulse width is measured to be 91 fs. We use a variable attenuator to control the input power to our waveguides. The coupling set-up is approximately the opposite of that used for loss measurements. We use a free-space objective to couple light into the waveguide and at the output collect the light with a lensed fiber. A short fiber takes the waveguide output to an optical spectrum analyzer (OSA) to view the spectral broadening of the pulse. We ensure the fiber is short enough so that the fiber does not induce any SPM [107].

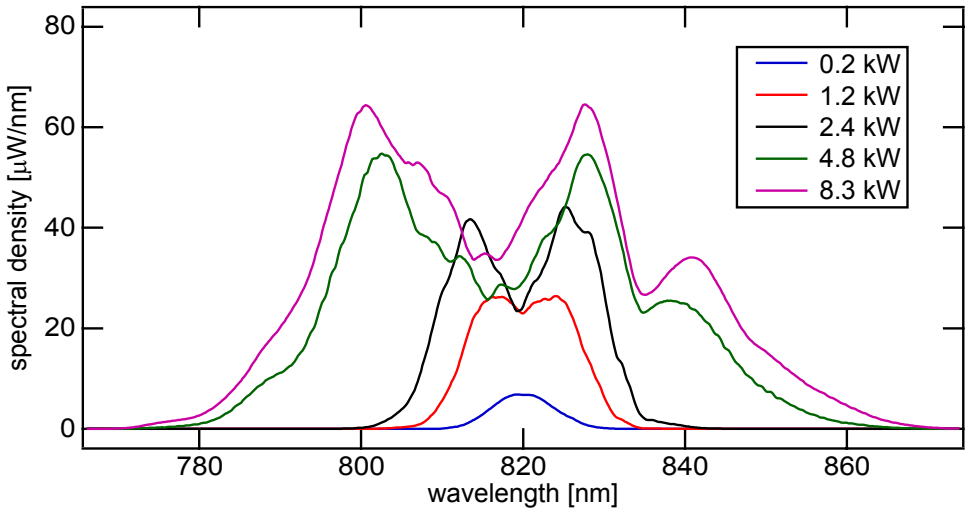

Figure 4.8: **Self-phase modulation in a Si_3N_4 waveguide.** A short pulse from a titanium sapphire laser centered at 820 nm is coupled into our 9 mm long waveguide. We see increased spectral broadening with larger optical intensity.

As we couple light with increased intensity, we induce larger and larger nonlinear phase-shifts and increase the spectral broadening. Figure 4.8 shows the results for a 9 mm long waveguide. The characteristic peaks and valleys are linearly related to ϕ_{max}^{NL}, the maximum nonlinear phase shift, such that $\phi_{max}^{NL} = (m + 0.5)\,\pi$ where m is the number of dips in the spectrum [25]. We can

compare this to the measurement of the spectral broadening for an accurate calculation of the phase shift.

4.4.2 Calculation of n_2

By estimating the maximum phase shift from the spectral plot in figure 4.8, we can derive a value for n_2 using the following relation:

$$\phi_{\max}^{\mathrm{NL}} = \gamma P_0 L_{eff} \tag{4.2}$$

where P_0 is the peak input power to the waveguide, L_{eff} is the effective interaction length and γ is the nonlinear parameter defined as:

$$\gamma = \frac{\omega n_2}{c A_{eff}} \tag{4.3}$$

with A_{eff}, the effective modal area. We use an effective length to take into account propagation losses for our device and define this value as:

$$L_{eff} = \frac{1 - e^{-\alpha L}}{\alpha} \tag{4.4}$$

We estimate the $\phi_{\max}^{\mathrm{NL}}$ with 1.2 kW to be 2π. The waveguide length is 9 mm and the propagation loss of 6 dB cm^{-1} gives an L_{eff} of 5 mm. The effective area of the mode is 3.8×10^{-13} m^2 from simulation, and we take the center wavelength to be 820 nm. Because the mode is loosely confined to the waveguide, we take into account that only 70% of the power is in the Si_3N_4 core. These values yield the value of n_2 as 1.1×10^{-19} m^2 W^{-1}, which agrees well with the only other measurement [86] and is within range of the theoretical results shown in figure 4.7.

A second way of using SPM to measure the material n_2 is from a careful measurement of the linewidth broadening. The linewidth broadening is directly related to $\phi_{\max}^{\mathrm{NL}}$, and therefore we expect linear increase with pump power. We perform a second experiment using waveguides with a 400 by 1200 nm cross-section. These guides confine more light to the Si_3N_4 and have lower propagation losses, which leads to lower pump powers for the same phase shifts from the first experiment. We plot the linewidth broadening as a function of input power in figure 4.9.

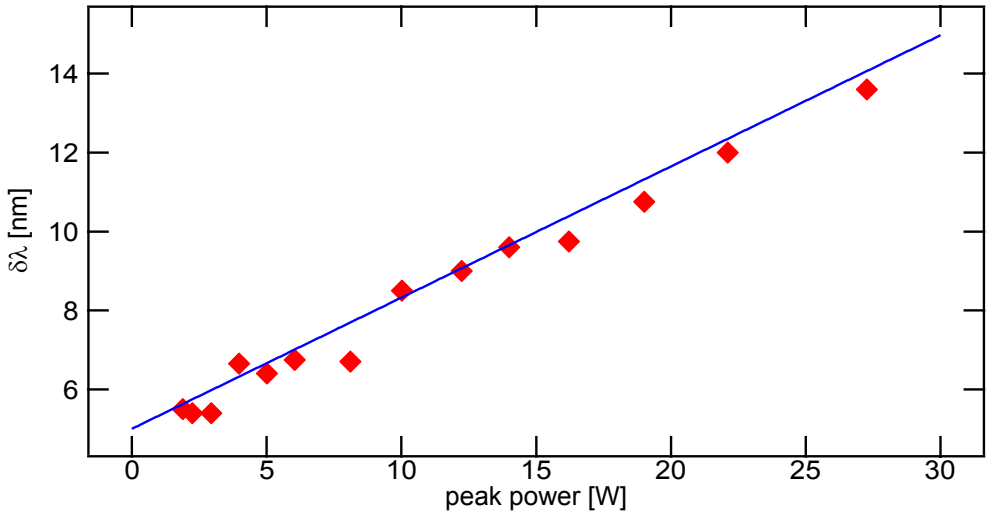

Figure 4.9: **Pulse linewidth broadening from SPM in Si_3N_4 waveguides.** The red diamonds are measurements from a 1.6 cm, 400 by 1200 nm waveguide with variable input pulse powers. The blue line is a theoretical fit using the model from equation 4.5. A good fit is reached when the n_2 value is set to $1.2 \times 10^{-19}\,\mathrm{m^2\,W^{-1}}$.

The theoretical broadening is linearly proportional to n_2 for a Gaussian pulse as shown in [109]:

$$\delta\lambda = \delta\lambda_0 + 4\sqrt{\frac{2\ln 2}{e}}\frac{\lambda n_2 L_{eff} P}{c A_{eff} t_p} \tag{4.5}$$

where $\delta\lambda_0$ is the input pulse bandwidth and t_p is the pulse linewidth. With an initial pulse bandwidth of 5 nm, we use a value of $n_2 = 1.2 \times 10^{-19}\,\mathrm{m^2\,W^{-1}}$ for

the fit to the measured data shown in figure 4.9.

CHAPTER 5

FOUR-WAVE MIXING

5.1 Introduction

Four-wave mixing (FWM) is a third order nonlinear process. As the name suggests, the process involves four waves, usually designated as two pump waves, a signal and an idler wave. The process is parametric in that when the two pump photons are annihilated strict energy conservation dictates the frequencies of the converted signal and idler waves. Degenerate FWM occurs when the pump photons are the same frequency; in this case a strong single pump source can provide both photons for the nonlinear interaction. With a simple pump input, FWM occurs with the mixing of the pump and the background noise. The process can also have a seeded signal wave. In this case the signal can experience parametric gain and the information on the frequency will be converted to the idler wavelength.*

Although the process will occur in bulk materials with overlapped beams [23], FWM becomes much more efficient over the long interactions lengths provided in waveguides. In optical fibers very efficient parametric amplification and frequency conversion have been demonstrated [111]. In silicon-based photonics, early demonstrations showed very weak conversion efficiencies [112, 113] over a limited bandwidth. By using phase-matched waveguides, parametric gain was demonstrated on-chip using a pulsed source [19]. However, because of the TPA and FCA in silicon waveguides, the conversion efficiency for continuous-wave (CW) pumping is shown to be signifi-

*Portions of this chapter are reproduced with permission from [90]

cantly lower [114], but can be very broad-band [115] due to the short interaction length. Other materials have been used for FWM in integrated photonics including doped glass [116], which suffers from a weaker nonlinearity, and chalcogenides [117], which are more complicated for fabrication and struggle with high input powers (thus limiting their efficiency). A number of applications for the FWM have been explored recently, including high-speed wavelength conversion [118], high data rate broadcasting [119], tunable optical delay [120], signal regeneration [20], and an optical time-lens [22]. As previously discussed, we believe the use of Si_3N_4 will be able to overcome the limitations of other materials to provide a robust system for broadband parametric gain and high efficiency frequency conversion.

5.2 Coupled Amplitude Equations

The FWM effect arises directly from the nonlinear polarization induced by $\chi^{(3)}$ in the material when we consider the interactions between waves at four frequencies. In chapter 2, we introduced the optical susceptibilities in the case for only a single field. Considering multiple fields we can rewrite equation 2.5c as [23]:

$$\mathbf{P}(\mathbf{r},t) = \sum_n P_n(\mathbf{r})\, e^{j\omega_n t} + \text{c.c.} \tag{5.1a}$$

$$P_n(\mathbf{r}) = \chi_n^{(1)}\mathbf{E}_n + P_n^{NL} \tag{5.1b}$$

$$P_n^{NL} = \sum_{i,j,k} \epsilon_0 \chi^{(3)}\left(\omega_n = \omega_i + \omega_j + \omega_k : \omega_i, \omega_j, \omega_k\right)\mathbf{E}_i\mathbf{E}_j\mathbf{E}_k \tag{5.1c}$$

where we have ignored the $\chi^{(2)}$ contribution to P_n^{NL} and note that the subscripts represent individual frequencies. From equation 5.1c, we note the subscripts i,

j, and k can represent any field such that their sum (or difference) add up to the frequency ω_n. For the case when we have multiple fields interacting, we want to rewrite the polarization of each individual field in the form:

$$P_n^{NL} = P_n(z)\, e^{j(\beta_n z - \omega_n t)} \tag{5.2}$$

for a wave propagating in the z-direction. We can find $P_n(z)$ from equation 5.1c and substitute this into the nonlinear wave equation, equation 2.10. From here, we can then solve for the coupled amplitude equations which will take the general form [23]:

$$\frac{dE_n}{dz} = \frac{j2\pi\omega_n}{nc} P_n^{NL} \tag{5.3}$$

where E_n is the field amplitude at frequency ω_n and is related to the intensity by $I_n = nc\epsilon_0 |E_n|^2 /2$.

In the degenerate case of FWM (DFWM), the frequencies for the idler wave, ω_i, is defined by the pump and signal frequencies such that $\omega_i = 2\omega_p - \omega_s$. We can write the coupled amplitude equations considering a strong undepleted pump and low power signal and idler waves as [25, 121, 122, 123]:

$$\frac{dE_p}{dz} = -\frac{\alpha_p}{2} E_p + j\gamma \left|E_p\right|^2 E_p \tag{5.4a}$$

$$\frac{dE_s}{dz} = -\frac{\alpha_s}{2} E_s + 2j\gamma \left|E_p\right|^2 E_s + \gamma E_p^2 E_i^* e^{-j\Delta\beta z} \tag{5.4b}$$

$$\frac{dE_i}{dz} = -\frac{\alpha_i}{2} E_i + 2j\gamma \left|E_p\right|^2 E_i + \gamma E_p^2 E_s^* e^{-j\Delta\beta z} \tag{5.4c}$$

where α_n represents the losses at frequency ω_n which for Si_3N_4 can be assumed to arise only from linear loss mechanisms and we have assumed that the A_{eff} for all waves is the same (this is lumped into the γ parameter defined in equation 4.3). The first term is responsible for the linear loss in the waveguide. The second term of 5.4a represents the SPM, while the second term for equations 5.4b and 5.4c are from cross-phase modulation (XPM) of the pump on the

signal and idler respectively. All these terms induce a nonlinear phase-shift on the respective waves. The final term in equations 5.4b and 5.4c is the energy transfer term, which is responsible for parametric gain and wavelength conversion. The energy transfer is dependent on the linear phase-mismatch, $\Delta\beta$, defined as:

$$\Delta\beta = 2\beta_p - \beta_s - \beta_i \tag{5.5}$$

The term arises from the $P_n(z)$ term in equation 5.2 when substituted into the coupled amplitude equations.

To find the final phase-matching condition for an efficient FWM process we must take into account not only the linear phase-shift but also the nonlinear phase-shift from SPM and XPM. Considering the case for a strong pump and weak signal and idler waves, the net phase-matching term can be shown to be approximately [25, 111, 122, 19]:

$$\kappa = 2\gamma P_p - \Delta\beta \tag{5.6}$$

As we can see from equations 5.5 and 5.6, meeting the phase-matching condition is dependent both on pump power and the propagation constants at each wave involved. In order for κ to be zero, we must achieve anomalous group velocity dispersion (i.e. a positive D from equation 2.29 or a negative β_2 from equation 2.28). Since the material dispersion is normal, we must use the waveguide dispersion (or modal dispersion) as counterbalance [31, 117].

5.3 Dispersion Engineering

In this section we will show that by changing the dimensions of the waveguide, we can drastically change the dispersion curves. As discussed in the previous section, we require anomalous dispersion at the pump wavelength. For relatively low pump intensities, the phase-matching term reduces to the linear phase-matching condition which occurs when pumping at a zero group velocity dispersion (ZGVD) point. We show sample dispersion curves for 1500 nm wide Si_3N_4 waveguides of various core thickness in figure 5.1. For the very thin waveguide cores the dispersion remains very normal which leads to an inefficient nonlinear process. From the simulated curves, we estimated the need for guide thickness of more than 700 nm to achieve anomalous dispersion in the c-band.

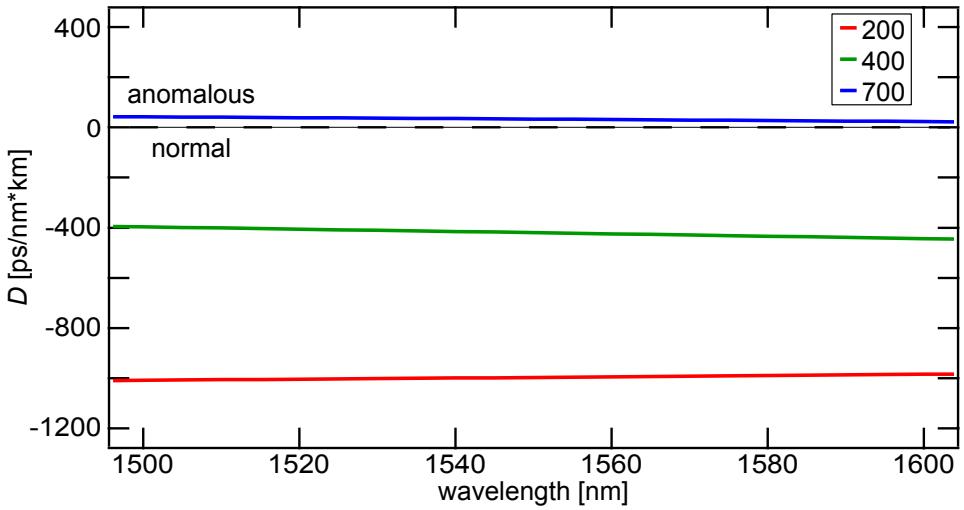

Figure 5.1: **Group velocity dispersion for Si_3N_4 with variable core thickness.** The waveguides all have the same width, 1500 nm, but the core thickness drastically shifts the dispersion curve. Although the width also affects the curves, to achieve anomalous dispersion at a wavelength of 1550 nm the core thickness must be at least 700 nm.

After the deposition process described in section 3.3.1 for thick films was developed, we could simulate how width changes the dispersion curves for a core thickness of 725 nm and with a sidewall angle of 10° from the etch described in section 3.3.3. We see in figure 5.2 for relatively small changes in the waveguide width we can alter the dispersion curve and shift the ZGVD wavelength. Additionally, the wider waveguides have a flatter dispersion, which is necessary to phase-match at a variety of pump wavelengths. Precise control over the width is critical to meet the phase-matching condition of equation 5.6.

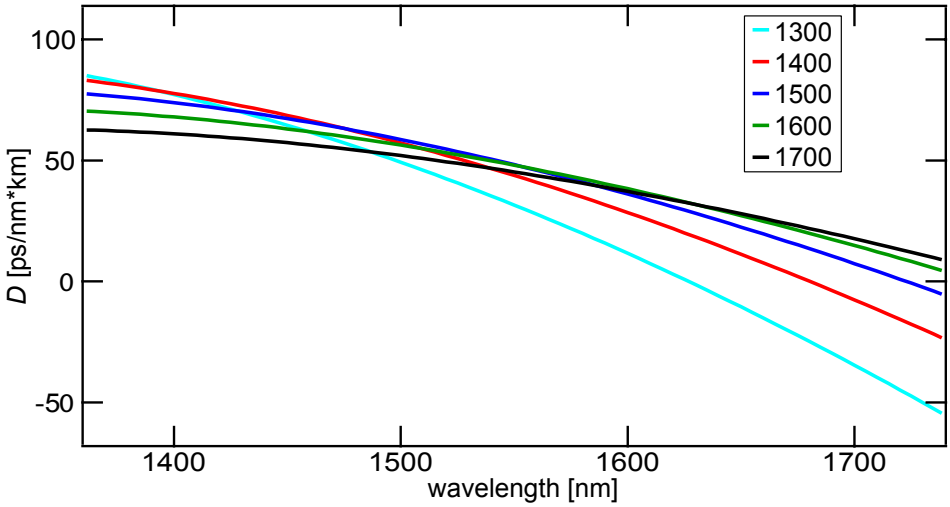

Figure 5.2: **Dispersion curves for varying waveguide width.** The waveguides all share a core thickness of 725 nm and a sidewall angle 10°. For the narrower waveguides the ZGVD wavelength is pushed closer to 1550 nm. For wider waveguides the dispersion curve becomes flatter.

The dispersion can also be altered in a curved waveguide where a sharp bend deforms the mode from the straight waveguide case. In figure 5.3, we view the change in the dispersion curve across a number of bend radii. The tighter the bend radius, the more normal the dispersion becomes as the optical mode is pulled into the SiO_2 cladding. These curves become critical for the devices discussed in chapter 6.

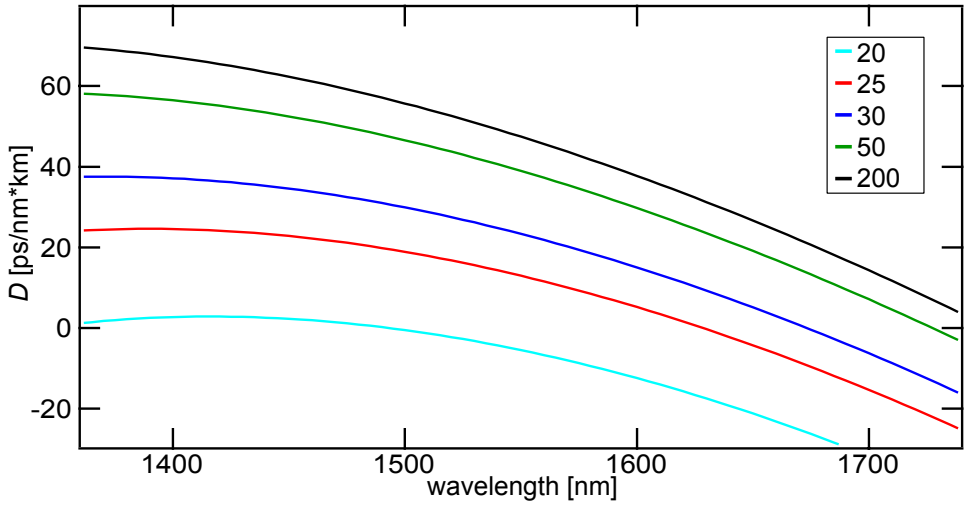

Figure 5.3: **Dispersion curves for variable bend radii.** All the waveguides have a cross-section of 725 by 1600 nm and a 10° sidewall angle. For tighter bending radii, the dispersion drops significantly and can go from anomalous with no bend to normal with a 20 µm bend at the wavelength of interest.

5.4 Wavelength Conversion

The conversion efficiency η from signal to idler wave is commonly defined as $\eta = \frac{P_i^{\text{out}}}{P_s^{\text{in}}}$ and can be measured by comparing the power of the signal and idler at the output of a waveguide with accurate knowledge of the propagation losses. By solving the coupled amplitude equations and assuming an undepleted pump. We can solve for the conversion efficiency [25, 111, 122]:

$$\eta = \left(\frac{\gamma P_p}{g}\sinh\left(gL_{eff}\right)\right)^2 \tag{5.7a}$$

$$g = \sqrt{\left(\gamma P_p\right)^2 - \left(\frac{\kappa}{2}\right)^2} \tag{5.7b}$$

where g is known as the parametric gain coefficient and P_p is the pump power at the waveguide input.

We measure the conversion efficiency for a waveguide with a cross-section

of 725 by 1450 nm with a 23° sidewall angle. The waveguide length is 6.2 cm and has linear loss as described in section 4.3.1 of 0.5 dB cm^{-1}. The waveguide cross-section gives a ZGVD wavelength of 1565 nm. Therefore, we center the pump laser at 1535 nm, just into the anomalous regime. The signal will be tuned from 1400 to 1525 nm which create idler waves from 1699 to 1545 nm respectively.

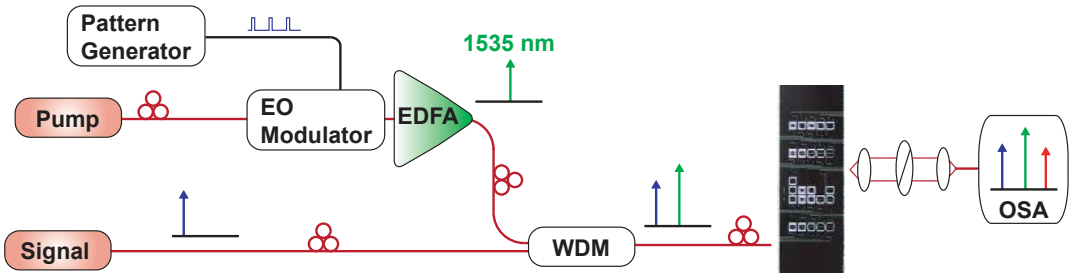

Figure 5.4: **Experimental set-up for FWM in Si_3N_4 waveguides.** The pump wavelength is kept fixed and is modulated and amplified to achieve large peak powers. The signal is tuned across a wide wavelength range. Using a multiplexer the beams are combined and coupled into the chip. With polarization rotators, we are able to independently ensure the polarizations for pump and signal are properly set and aligned. The output from the chip is collimated and sent to an OSA for measurements.

Figure 5.4 shows the experimental set-up for measuring the wavelength conversion. We use an electro-optic modulator to increase the peak power of the pump during operation. The pump is modulated at 1 MHz with a duty cycle 100:1 created by a pattern generator. This leads to 10 ns of "on" pump for every 1 µs. The pump intensity is increased using an erbium doped fiber amplifier (EDFA). We use a multiplexer to combine the pump and signal beams and a tapered fiber to couple into the chip. The waveguide output is collected with a lens and collimated to an optical fiber. We use an optical spectrum analyzer (OSA) to measure the output power for the signal and idler waves.

In figure 5.5, we plot the measured conversion efficiency as a function of

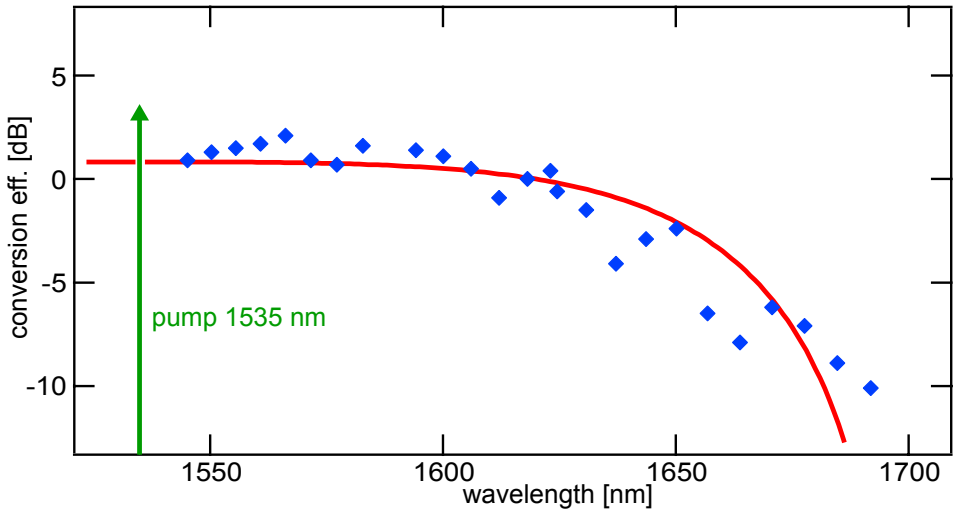

Figure 5.5: **Signal to idler conversion efficiency in a Si_3N_4 waveguide.** With a pump centered at 1535 nm and with a peak power of 20 W the FWM signal to idler conversion efficiency is plotted for the generated idler wavelengths. The red curve is the simulated efficiency and shows good agreement with the measured blue diamonds.

idler wavelength. On this graph we have corrected for the modulation on the pump to increase the raw efficiency measurements by the duty cycle. The average pump power in the waveguide for this measurement is 200 mW which leads to a peak power of 20 W. We see broadband conversion, with a 3 dB point more than 90 nm from the pump. Since the efficiency is symmetric about the pump, this gives a total conversion bandwidth of over 180 nm which can only result from the strong phase-matching. We also plot the theoretical conversion efficiency for our peak pump power assuming an n_2 of 2×10^{-19} m^2 W^{-1}. The good agreement demonstrates accurate modeling of the dispersion and estimate of the nonlinear refractive index.

5.5 Parametric Gain

With the high conversion efficiencies experienced by the idler wave shown in figure 5.5, we also expect to observe gain on the signal wave. The on/off gain is defined as the output signal power when the pump is on compared to the output signal with no pump. The gain of the device is defined slightly differently, by comparing the input signal power to the output signal power. Working from the coupled amplitude equations, the gain, G, can be calculated as [25, 111, 19, 122]:

$$G = \frac{P_s^{\text{out}}}{P_s^{\text{in}}} = 1 + \eta = 1 + \left(\frac{\gamma P_p}{g}\sinh\left(gL_{eff}\right)\right)^2 \tag{5.8}$$

If the phase-matching is poor or the value of g is small, we expect to see generation of a weak idler and little signal gain. In this case both the conversion efficiency and idler grow as P_p^2 which can be described as the weak conversion approximation. However, if we assume we have ideal phase-matching (i.e. $\kappa \to 0$) and gL_{eff} becomes much greater than 1, the gain becomes [25]:

$$G \approx \frac{1}{4}e^{2\gamma P_p L_{eff}} \tag{5.9}$$

The experiment performed in section 5.4 has large peak powers but relatively low average power. The conversion efficiency for the average power case is closer to $-20\,\text{dB}$ and therefore, we cannot resolve the signal gain with the OSA. In order to directly measure on/off gain, we filter the signal wavelength from the output and send it to a high-speed photodetector. We view the resulting signal on an oscilloscope, figure 5.6. We measure an on/off gain of $3.8\,\text{dB}$ showing the strong peak pump powers induce parametric gain of the signal.

In order to directly measure the signal gain across a broad-band spectrum, we modify the experimental set-up shown in figure 5.4. We now modulate both

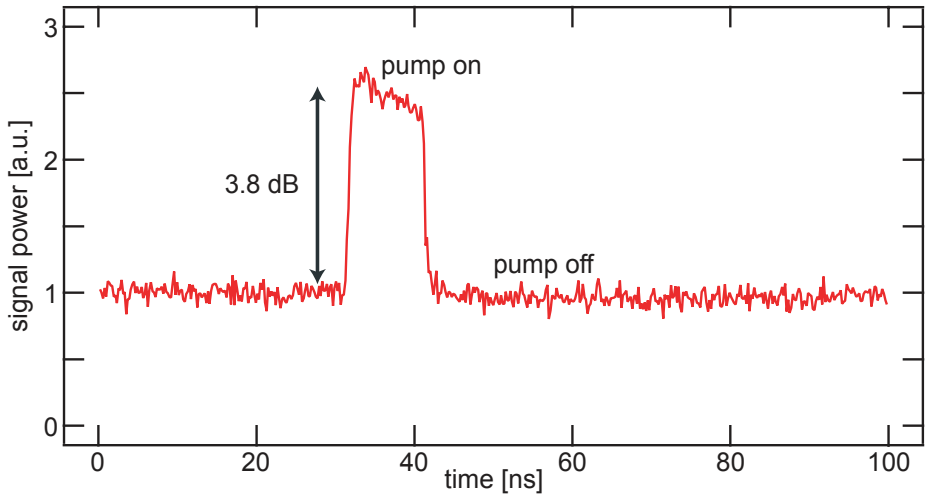

Figure 5.6: **Temporal visualization of parametric gain.** By filtering the signal wavelength from the experiment in section 5.4, we can use an oscilloscope to measure the on/off parametric gain.

the pump and signal at 5 MHz with the same 100:1 duty cycle to generate 2 ns "on" states. The pump is tuned to 1550 nm and the signal is varied between 1475 and 1625 nm. We use a tunable optical delay to ensure the "on" state for both pump and signal to overlap in the waveguide. We again use an OSA to measure the signal power with the pump on and compare that to the power with the pump off.

The peak pump power for the experiment is 24 W. In figure 5.7, we plot the measured on/off gain as a function of wavelength. The waveguide's propagation loss is 3 dB, therefore, any on/off gain greater than this value results in a net gain. The waveguide is therefore behaving as a broadband parametric amplifier covering more than 55 nm.

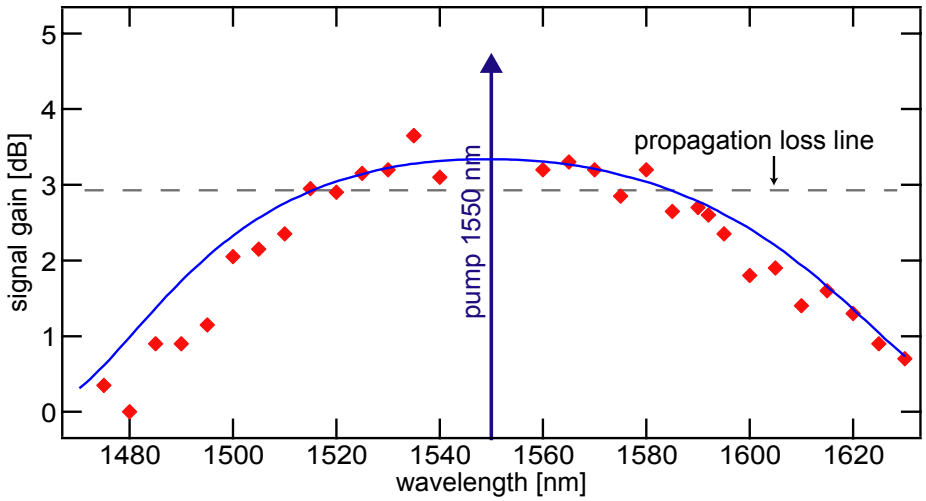

Figure 5.7: **Signal gain as a function of wavelength.** The measured on/off gain, red diamonds, is plotted with the propagation loss line through the waveguide superimposed. Any points residing above this line demonstrate net parametric gain through the waveguide. The simulated parametric gain is plotted as well showing good agreement with experiment.

CHAPTER 6

PARAMETRIC OSCILLATION

6.1 Introduction

Silicon-based optical amplification has been achieved through stimulated Raman scattering [6, 124, 125], parametric mixing [19] and by silicon nanocrystals [126] or nanopatterned silicon [127]. Losses in most of these structures have prevented oscillation. Raman oscillators have been demonstrated [128, 129, 130], but with a narrow gain bandwidth insufficient for WDM.*

As in lasing, optical parametric oscillation (OPO) occurs when the round-trip parametric gain exceeds the loss in a cavity. The first OPO exploited parametric gain from a $\chi^{(2)}$ crystal placed inside a large free-space cavity [131]. By tuning the size of the cavity in this set-up the generated frequencies can be selectively tuned [23]. In this chapter, we present a different approach in order to make an integrated OPO. In section 5.5, we demonstrated parametric gain in a Si_3N_4 waveguide utilizing a $\chi^{(3)}$ process. As shown in section 4.3.2, the low optical losses in Si_3N_4 can be translated into high-Q resonators. Here, we will discuss the process of optical parametric oscillation induced by FWM-base parametric gain for Si_3N_4 ring resonators. We will examine the threshold pump power both theoretically and experimentally, and discuss the cascading process that occurs during oscillation. The microresonator based OPO can also be used to generate an optical frequency comb. In section 6.4, we examine this process and look at broadband combs and combs centered at different wavelengths.

*Portions of this chapter are reproduced with permission from [90]

6.2 FWM-based Optical Parametric Oscillation

By achieving phase-matching in waveguides and with sufficient pump power and interaction length we are able to achieve parametric gain in straight Si_3N_4 waveguides. By using an optical resonator, the power requirement and device footprint for achieving gain can be reduced due to the enhancement of the optical field (as in equation 2.49). When all interacting waves of the DFWM process are on resonance, we get an even greater enhancement of the nonlinear process [116, 132, 133] and generate signal and idler waves from the background noise that overcome the cavity loss. Because the FWM wavelengths are strictly determined by energy conservation, phase-matching in the microresonator enables the cavity modes to be evenly spaced in frequency and coincide with the generated wavelengths.

When a pump laser is tuned to a cavity resonance (figure 6.1), the device is capable of generating simultaneous parametric oscillations at signal and idler waves. The FWM process can cascade generating new wavelengths at multiple resonances. High-Q CaF_2 toroidal resonators [134] and silica microtoroids [135] and microspheres [136] have shown parametric oscillation based on this process. However, because these materials have low nonlinearities, the Q necessary for operation is extremely high. As a result, these devices are sensitive to perturbations and not conducive to on-chip integration. Operation requires a purged N_2 environment and delicate tapered-fiber coupling.

A microring resonator using phase-matched design waveguides discussed in section 5.3 is used to create an OPO. The first measured resonator has a 20 µm radius with a cross-section of 727 by 1580 nm. The device has a Q_L of 100,000,

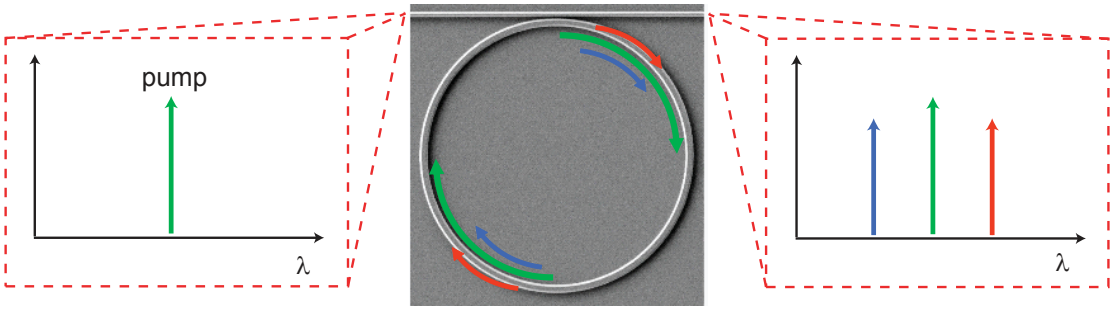

Figure 6.1: **On-chip optical parametric oscillation.** A single pump laser tuned to the resonance of a Si_3N_4 microring allows the generation of numerous new wavelengths. As the pump power is increased by the field enhancement of the ring, the parametric gain overcomes the round trip loss and neighboring resonances begin oscillations. The pump and generated frequencies are coupled out of the ring and back to the bus waveguide.

and the free spectral range is 9.4 nm (1.17 THz), giving a finesse of over 600. We use a tunable laser initially centered 1560.7 nm and amplify the emitted light using a high power EDFA. Before coupling into our waveguides, we filter out the amplified spontaneous emission (ASE) of the EDFA to get a cleaner output spectrum and to prevent any ASE noise from seeding a four-wave mixing process in the cavity. We collect the output from the waveguide with a fiber and view the results with an OSA. We observe oscillations initially in the second cavity mode (the m±2 modes) on either side of the pump frequency (cavity mode "m"). We show a sample output spectrum in figure 6.2. Here, the modes "fill-in" via the cascaded four-wave mixing process as the pump power in the resonator is increased. The power dropped into the ring at this point is 150 mW.

To show the flexibility of frequency spacing, we perform the same experiment on a ring with a different radius. We use a ring with a 58 µm radius and a cross-section of 711 by 1700 nm, giving anomalous GVD in the C-band and a ZGVD wavelength of 1610 nm. The ring has a Q_L of 500,000 and a FSR of

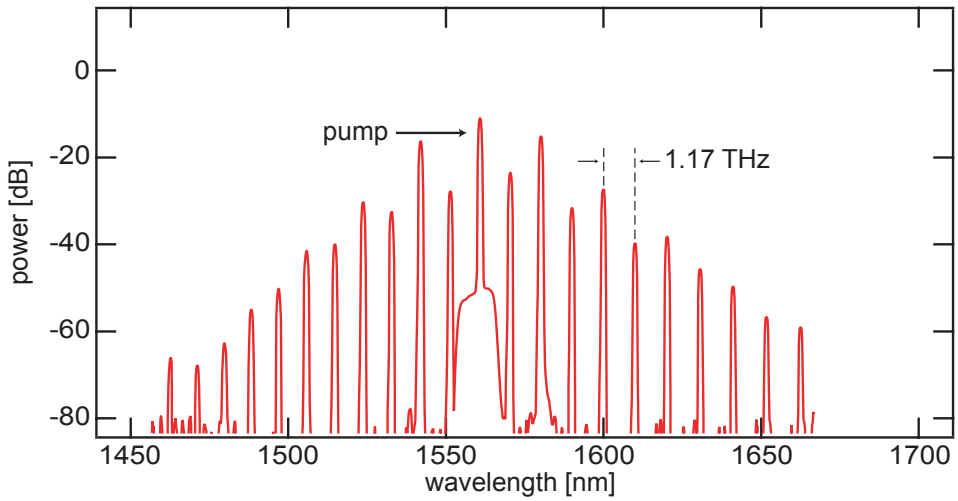

Figure 6.2: **Demonstration of optical parametric oscillation in a** 20 µm **ring.** Pumping near 1561 nm, we generate 21 new wavelengths over a 200 nm span with spacing equivalent to the ring FSR.

403 GHz. In figure 6.3, we plot the measured spectrum as a function of dropped pump power to show how the generated oscillations change as a function of power. We see the initial oscillation at frequencies near the peak of the theoretical parametric gain and with increased power the process cascading and the modes filling. By increasing the pump power and then slowly tuning the pump frequency deeper into the thermally shifted resonance, it is possible to achieve a soft "thermal lock" in which the cavity heating is countered by diffusive cooling [137], and the coupled power remains constant. At an input power of 310 mW, the output spectrum with a broadband flat response shown in figure 6.4 is observed. Eighty-seven new frequencies are generated between 1450 and 1750 nm, corresponding to wavelengths covering the S, C, L, and U communication bands. In this case, the cascaded oscillations have not only been mixed through a DFWM process but also through non-degenerate FWM creating a frequency comb discussed in more detail in section 6.4. The suitability of the generated comb as a multiple frequency source is discussed in greater detail

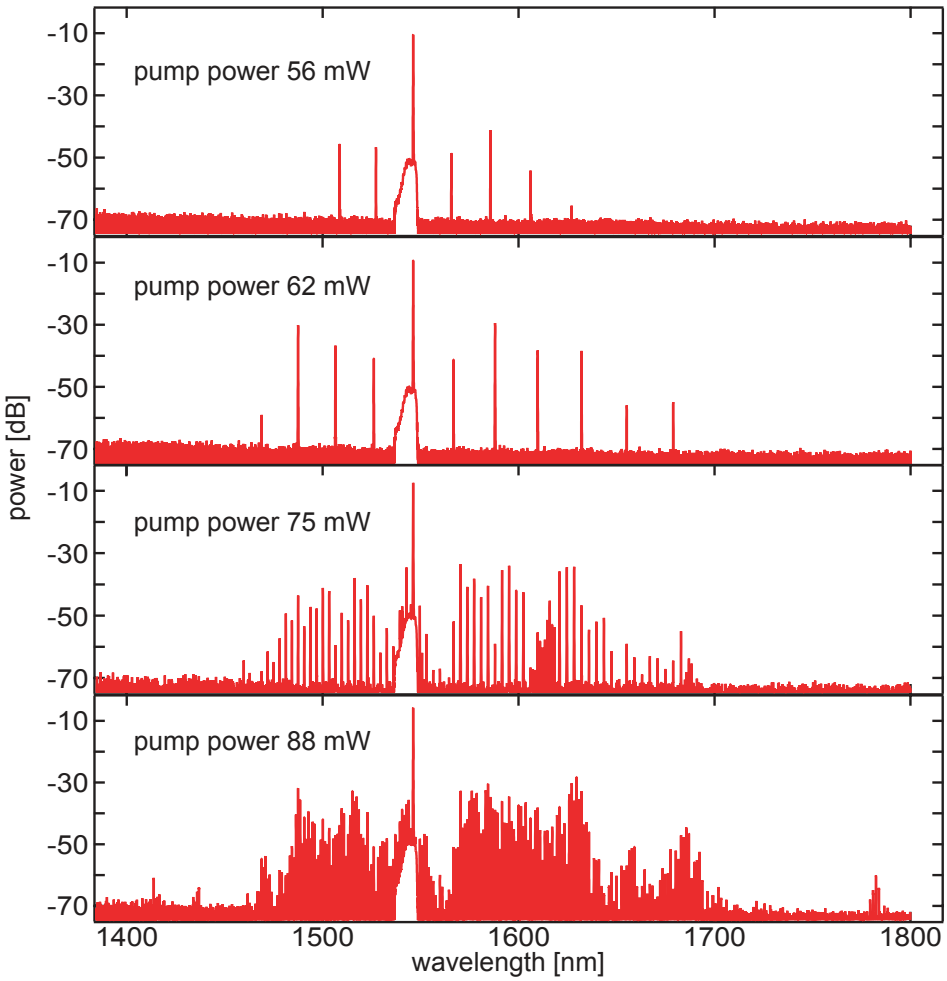

Figure 6.3: **Generated spectrum from a microresonator optical parametric pump power with varying input powers.** We observe the first oscillations at the peak of the parametric gain spectrum. As we increase the power, more and more resonator modes oscillate as the FWM process is cascaded and threshold powers are reached for more wavelengths.

in chapter 7.

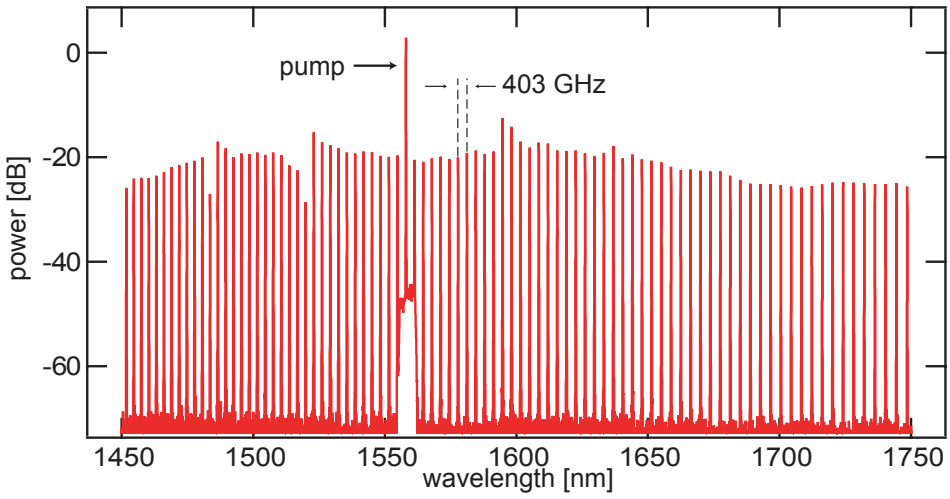

Figure 6.4: **Flat broadband multiple wavelength generation.** Using a 58 µm radius ring and pumping at 1557.8 nm, 87 wavelengths are generated with equal spacing. By using each line as a carrier frequency, the source can be used to drive an on-chip WDM network.

6.3 Threshold Power

We can theoretically calculate the threshold power for the ring resonator by equating the parametric gain from equation 5.9 with the round trip power loss from 2.35. This gives the condition for the pump power:

$$2\gamma P_p = \alpha \tag{6.1}$$

and if we assume a critically coupled cavity and use the resonant enhancement factor from equation 2.49, the necessary power input to the cavity is shown to be:

$$P_t = \frac{2\pi^2 n_g^2 R A_{eff}}{\lambda_0 n_2 Q_i^2} \tag{6.2}$$

where P_t is the threshold power. This equation is in agreement with deriving an equation for the threshold power using coupled mode theory [134] and by calculating the power needed to shift the resonance by one cavity linewidth with

the static Kerr effect [138]. The important thing to note from equation 6.2 is that the theoretical threshold power is proportional to ring radius and inversely proportional to the quality factor. At small radii, a trade off between Q and radius exists with smaller rings having lower Q due to a combination of radiation and extra scattering and absorption from the increased modal overlap with the sidewalls. For larger rings, the Q does not continue to increase with the radius and subsequently the threshold power for larger rings will begin to increase linearly with physical size.

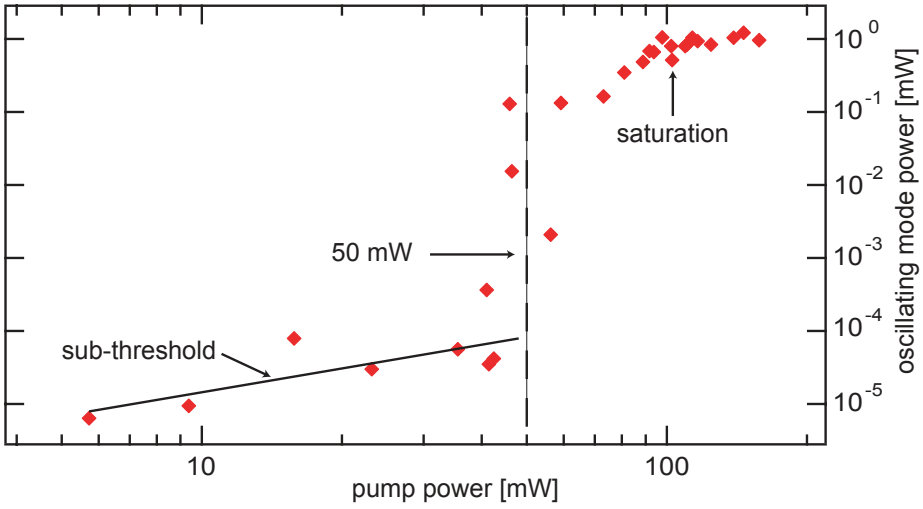

Figure 6.5: **Measurement of the oscillation threshold.** The output power in the first generated mode is compared to the pump power. In this device, parametric oscillation occurs with 50 mW of pump power and the subsequent slope efficiency is 2%.

We experimentally measured the threshold power for a 40 µm ring with a Q_L of 200,000. We monitored the power of the first generated frequency while increasing the pump power. We measure an oscillation threshold of 50 mW dropped into the ring as shown in figure 6.5. From equation 2.49, the circulating power of the resonator is about 10 W. This value is very close to the power used to demonstrate net gain in straight waveguides from section 5.5. The power

with the first oscillating mode saturates when the pump power reaches 100 mW due to the cascaded FWM causing a power redistribution to newly generated modes. Additionally, in the sub-threshold behavior, the signal noise should increase proportionately to the pump squared [139] as with the weak conversion case discussed in section 5.5. On the log-log plot in figure 6.5, we roughly see a slope of two for the increased power in the background noise from the increasing pump before reaching threshold, further confirming the parametric oscillation and analogy to lasing. Recently, we have demonstrated 20 µm radius Si_3N_4 rings with Q_i greater than 3×10^6. Theoretically, the oscillation threshold for such a device would be less than 0.5 mW, which is well within the range of standard laser sources.

6.4 Frequency Comb Generation

If we consider a commercial mode-locked pulsed laser, in the time domain a train of pulses are emitted at the laser repetition rate, T_r. In the frequency domain, the short-pulse train is a comb of frequencies separated by $f_r = 1/T_r$ and with a spectral bandwidth inversely proportional to the temporal pulse width. In a free-running system, each successive pulse is not precisely the same and spectrally this creates a slip between the pulse envelope and the carrier phase. The offset is generally referred to as the carrier-envelope offset frequency, f_{ceo} and creates a global shift for the exact frequencies of the comb. By measuring and stabilizing the f_{ceo}, an optical frequency comb is formed in which the precise frequency of all comb lines are known [140]. This has powerful implications for metrology [141], high-precision optical clocks [142], astronomical (and other) spectroscopy [143], arbitrary waveform generation [144], microwave synthesis

and direct optical links to the microwave regime. Theodor W. Hänsch and John L. Hall shared the 2005 Nobel Prize in part for development of the optical frequency comb for precision spectroscopy.

More recently, a different class of optical frequency combs using the FWM in microresonators explored earlier in this chapter has been developed [145]. After initial oscillation mediated by DFWM as in section 6.2, three additional interactions can occur. The first is the cascading to higher order signal and idler waves in which the generated modes act as a pump and the original pump acts as signal. The second occurs when enough power is transferred to the generated modes and they are able to induce side-band oscillations of their own. The final, and most important to generation of a precisely spaced frequency comb, occurs when non-degenerate FWM results in mixing between all the generated lines in the resonator such that the energy conservation required by this mixing precisely determines and "locks" into place the comb lines. The first demonstrations for these μ-combs was in silica microtoroids [146]. The work was followed up in crystalline CaF_2 resonators [147].

In this section, we will discuss the generation of optical frequency combs in Si_3N_4 ring resonators. The repetition rate of our frequency comb is determined by the FSR of the individual ring and is usually in the hundreds of GHz range. Traditional ultra-fast laser combs have much lower repetition rates, but the μ-combs can access a very desirable frequency range linking RF and optical regimes. Additionally, the robust platform of the monolithically integrated Si_3N_4 combs, compared to the other demonstrated μ-combs, enables on-chip photonic integration and stable operating environment. The generation of frequency combs once oscillation is achieved is relatively straightforward. Assum-

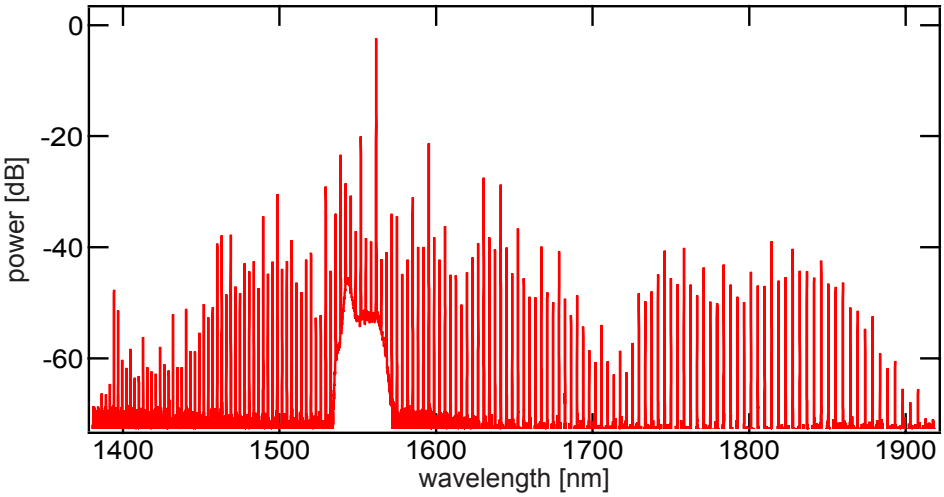

Figure 6.6: **A Si_3N_4 microresonator optical frequency comb.** By increasing the pump power after oscillations, higher order DFWM and non-degenerate FWM occurs between resonator modes. As the mode lines fill-in and begin mixing with each other the resonator modes are "pulled-in" and the frequency spacing becomes very precise generating an optical frequency comb. Here, over 150 comb lines are generated spanning over 60 THz.

ing a properly dispersion-engineered cavity, by increasing the pump power we can increase the breadth of the comb. By pumping the comb used to generate the spectrum shown in figure 6.4 with 400 mW, we can generate the frequency comb observed in figure 6.6. We have also recently experimentally shown the optical comb lines are evenly spaced to within 1 part in 10^{15} [148]. The well-defined spacing is critical for metrology and spectroscopy applications.

6.4.1 Octave Spanning Comb

The most common way of stabilizing the f_{ceo} is through $f - 2f$ self-referencing technique [149]. In this technique, a frequency generated at the shorter end of the spectrum, frequency f, is doubled using second-harmonic generation (SHG)

and then compared to the corresponding comb line at the other end of the generated spectrum, frequency $2f$. The resulting beat-note is equal to the f_{ceo} and by using feedback mechanisms to control the changes in this value the comb can be fully stabilized. A necessary precondition for this technique is an octave spanning comb. Only recently in silica microtoroids has an octave spanning [150] μ-comb been demonstrated. By engineering the dispersion to peak near the pump wavelength and increasing the pump power, we are able to generate an octave in a 100 μm Si_3N_4 ring resonator with cross-sectional dimensions of 725 by 1650 nm with a 10° sidewall angle. As seen in figure 6.7 [151], the comb spans over 128 THz with line-spacing of 230 GHz. The pump power necessary to generate this comb is about 750 mW dropped into the ring.

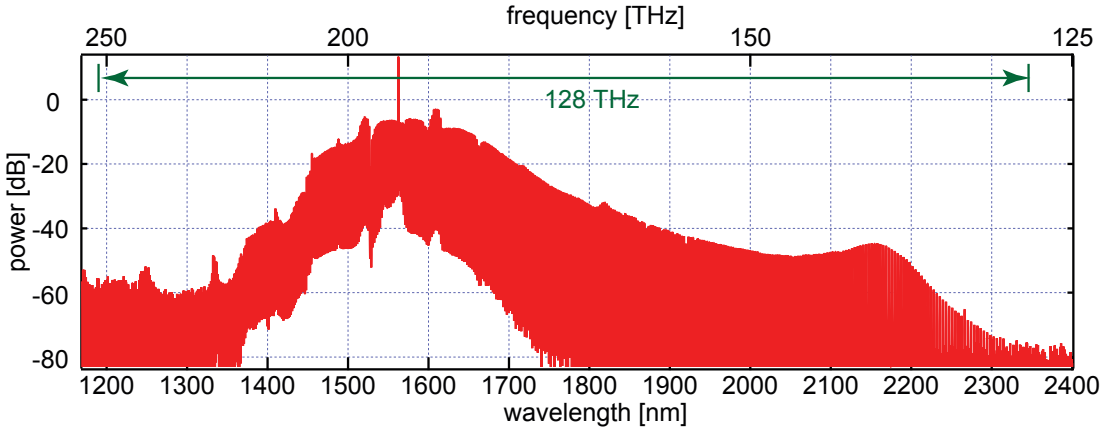

Figure 6.7: **An octave spanning Si_3N_4 μ-comb.** The optical resonator has a frequency spacing of 230 GHz and spans more than 128 THz resulting in the generation of over 550 comb-lines. Generating a full octave is necessary for $f - 2f$ self-referencing to stabilize the comb.

6.4.2 One Micron

Although we are able to achieve a full octave while pumping near 1550 nm, the lack of available frequency doubling materials at the longer wavelengths of 2.3 µm makes self-referencing difficult. Due to the flexibility in dispersion with waveguide design discussed in section 2.5, we can redesign the optical comb to be pumped at a different wavelength. We choose to pump at 1064 nm because of the readily available high power pump sources developed at this wavelength and the availability of doubling crystals and amplifiers for the extent of an octave-spanning comb in the c-band.

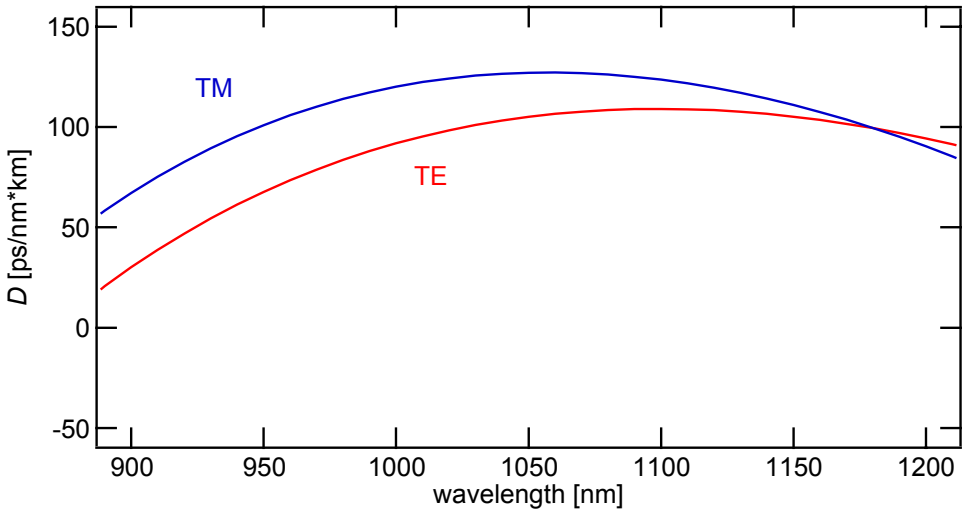

Figure 6.8: **Dispersion curves for optical comb generation with a** 1 µm **pump wavelength.** Both the TM (blue) and TE (red) curves are anomalous at the pump wavelength allowing use of either polarization for comb generation.

In figure 6.8, we show the redesign of the waveguide cross-section gives anomalous dispersion near one-micron. We see that unlike in our previous FWM based experiments centered in the C-band, we can achieve anomalous dispersion for both the TE and TM modes. This allows us to choose either po-

larization for comb generation and possibly generate two orthogonal combs simultaneously in the same cavity. We use free-space coupling to pump a 100 µm radius ring with cross-section of 725 by 1000 nm. Although the observed threshold for oscillation of the TE mode is lower, because of coupling inefficiencies we are able to generate a broader comb (figure 6.9) using the TM polarization. The coupling loss into the waveguide reduces the maximum pump power we have to drop on the ring and limits the breadth of the comb. However, with improved design of the coupling section the increased power should enable octave spanning combs centered at one micron.

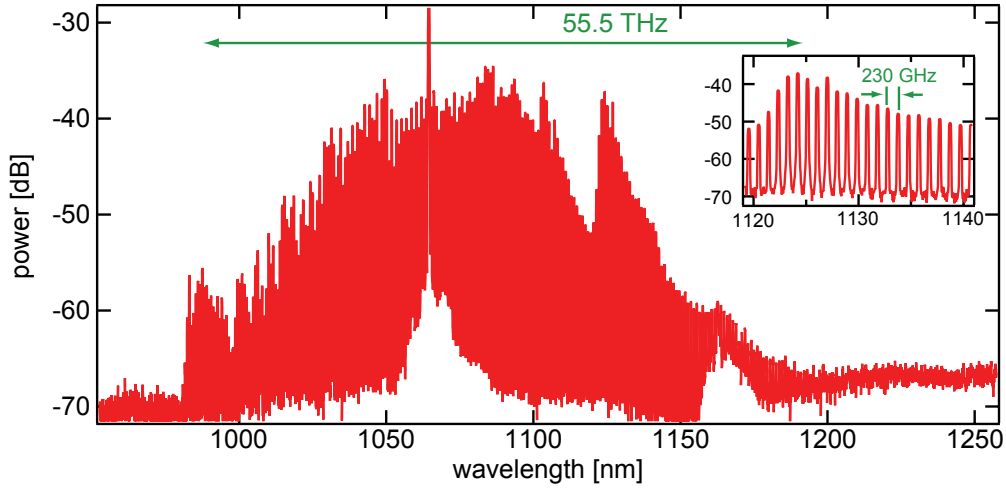

Figure 6.9: **Frequency comb pumped near** 1 µm**.** The generated comb spans over 55.5 THz with line spacing of 230 GHz (inset). The comb is the first Si_3N_4 demonstration of the TM mode oscillating in the microresonator.

Although previous work has shown flexibility in pump wavelength for CaF_2 resonators [152], this is the first demonstration of broad comb generation with a flexible pump wavelength. The work has broad applications to perhaps monolithic integration of combs centered at a variety of wavelengths on the same chip and even coupled to the same bus waveguide. The only limitation is the broad transparency window of Si_3N_4.

6.4.3 Low Repetition Rate

In order to directly link between the optical regime and the microwave regime, the repetition rate of the μ-comb must be within the detection range of fast photo-diodes (generally a maximum of 50 GHz). Because of the resonator size need to ensure such an FSR (as can be calculated from equation 2.46), we choose to change the resonator shape from a ring to an arbitrary closed loop spiral as shown in figure 6.10a. By making the minimum bend radius more than 100 μm, we can ensure the dispersion will not be influenced by the curved sections compared to the straight portions. Additionally, keeping a semi-ring at the coupling region ensures precise control over the coupling parameter to enable critically coupled devices. An additional benefit of using the enclosed spiral loop as opposed to the ring include reduced device footprint and avoiding the e-beam stitch fields discussed in section 3.3.2.

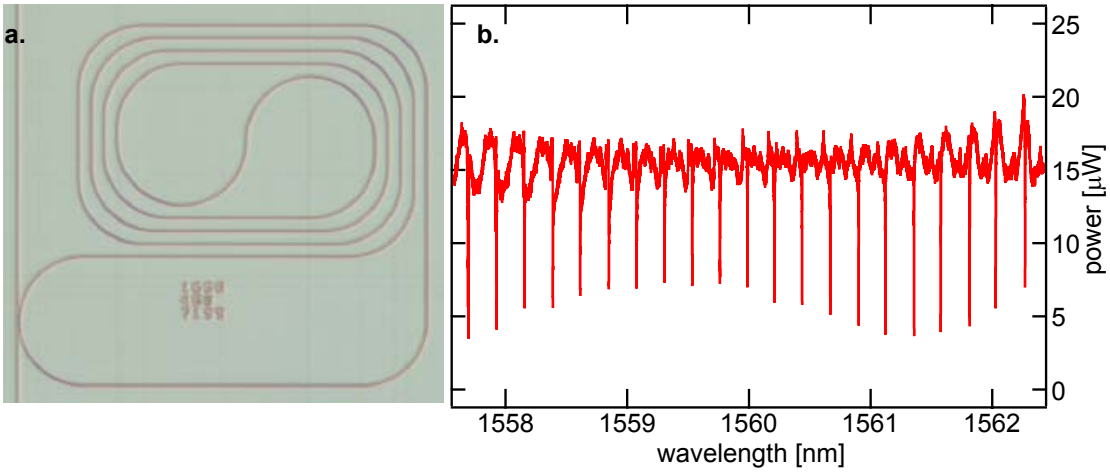

Figure 6.10: **A** 20 GHz **FSR Si_3N_4 resonator. a.** A micrograph of the enclosed spiral resonator. The path length of the device is precisely controlled to be 7.2 mm. **b.** The optical transmission spectrum showing the designed mode spacing and resonator Q greater than 1×10^6.

Preliminary experiments have shown the resonator's FSR to be as designed (figure 6.10b) and oscillations at high input powers. Because of the necessity for higher powers, we have not yet generated enough power in all the comb lines to directly observe the microwave beat-note as has been done in low-repetition rate silica [138] and CaF_2 combs [137]. Improving the coupling efficiency and using a higher powered EDFA should enable oscillation at every cavity resonance and the generation of a detectable beat-note. Additionally, improvements in the resonator Q could enable lower power comb generation in these devices (equation 6.2).

CHAPTER 7

ON-CHIP MULTIPLE WAVELENGTH SOURCE

7.1 Introduction

Silicon-based integrated photonics aims to deliver on-chip optical communications networks with bandwidths orders of magnitude larger than electronic networks. As the microelectronics industry moves to multi-core and multi-processor chips, CMOS-compatible photonics will replace much of the electronic communications backbone. A key benefit of optical communication systems is wavelength-division multiplexing (WDM) which enables a single waveguide to carry multiple data streams and is essential to reach the full bandwidth potential of photonic integrated circuits. Many components necessary for on-chip optical interconnects such as filters [153], modulators [6], switches [154] and detectors [8] have been demonstrated over the past decade. However, an integrated on-chip source capable of generating the many wavelengths necessary to drive the network has been elusive. Because silicon is an indirect band gap material, approaches thus far have focused on integrating III-V active devices by bonding, such as microdisk lasers [155] or a hybrid waveguide [156]. Although both methods can be replicated on-chip to generate multiple wavelengths, scaling to the hundreds of wavelengths envisioned by optical network architectures [119, 157] quickly becomes power hungry and space consuming. All-optical approaches have included utilizing the Raman effect in silicon [128]. Although this process can be cascaded [158], the wavelength separation is determined by the Raman shift which is inadequate for WDM standards.*

*Portions of this chapter are submitted as [159]

In this chapter, we examine the characteristics of the generated comb lines from the Si_3N_4 μ-comb described in section 6.4 and analyze their fidelity for WDM sources. In principle, the highly nonlinear process used to generate the comb could induce signal noise. The parametric process which generates the new wavelengths also induces a distinct phase relationship between the generated comb lines [145, 160]. Additionally, the large quality factor of the resonator leads to high circulating powers. The large intensities could also induce instability in the system due to the sensitivities of both the parametric gain and cavity lineshape to power and temperature fluctuations. Therefore, a robust measurement of the generated frequencies is required to demonstrate the usefulness of the on-chip source. We perform measurements of the linewidths for the generated frequencies and compare this with the pump laser linewidth. We also discuss the stability and long-term performance of the generated μ-comb by modulating individual comb lines. In section 7.3, we measure and discuss both the bit-error rate (BER) and eye-diagram.

7.2 Linewidth Measurement

The linewidth of one of the generated modes is measured by selecting a single mode from the output of the device with a tunable bandpass filter. The filtered mode is amplified using a low-noise EDFA and the signal is split using a 50/50 coupler. The first arm of the signal is sent through a 20 km spool of fiber so that it is no longer coherent with the other arm. The second arm is modulated at 5 GHz with a pattern generator driving an electro-optic modulator. The two arms are recombined, accounting for the difference in power between them using a variable attenuator, and the signal is sent to an electrical spectrum analyzer. By

measuring the FWHM of the noise about the 5 GHz line (and ignoring the narrow feature resulting from the unmixed signal), an accurate measurement of the linewidth can be made.

The mode generated at 1564.2 nm has a measured linewidth of 424 kHz. Replacing the new wavelength with the pump source, we measure 140 kHz. We believe the broadening is caused by the cascaded FWM interactions involved with the generation of the multiple wavelengths and is not strongly influenced by the much broader cavity resonance. Nevertheless, the demonstrated linewidth is sufficiently narrow for any type of on-chip optical communication. Furthermore, we measure the stability of a single generated frequency by taking a single-shot measurement of the temporal power fluctuations. The measurement shows less than 5% power variation over 50 µs with a 100 MHz detection bandwidth. By comparing the noise from the generated OPO mode and the background noise on the detector, we calculate the relative intensity noise to have an rms value of 1.6% over this bandwidth range.

7.3 Modulated Comb Lines

The measurements are performed on a 116 µm radius 725 by 1550 nm Si_3N_4 ring resonator OPO that generates over 100 new wavelengths across a 200 nm span (Figure 7.1) by pumping the cavity at a resonance near 1541 nm. The intrinsic Q of the ring is on the order of 10^6 which induces a cavity enhancement of the input pump by more than two orders of magnitude. Recently, we have shown that the spacings between these frequencies are even to within 1 part in 10^{15} of the center frequency [148]. In section 6.4.1, we have shown spectrally flat

and very broad frequency combs spanning an octave. However, the broadband combs can exhibit a high level of intensity noise measured with an RF spectrum analyzer indicating that the generated wavelengths are unstable in frequency and amplitude. For use as an on-chip source, the generated wavelengths must lack frequency or power drift. The ring must also be stable enough to maintain oscillations for an arbitrary period of time without falling "out of resonance".

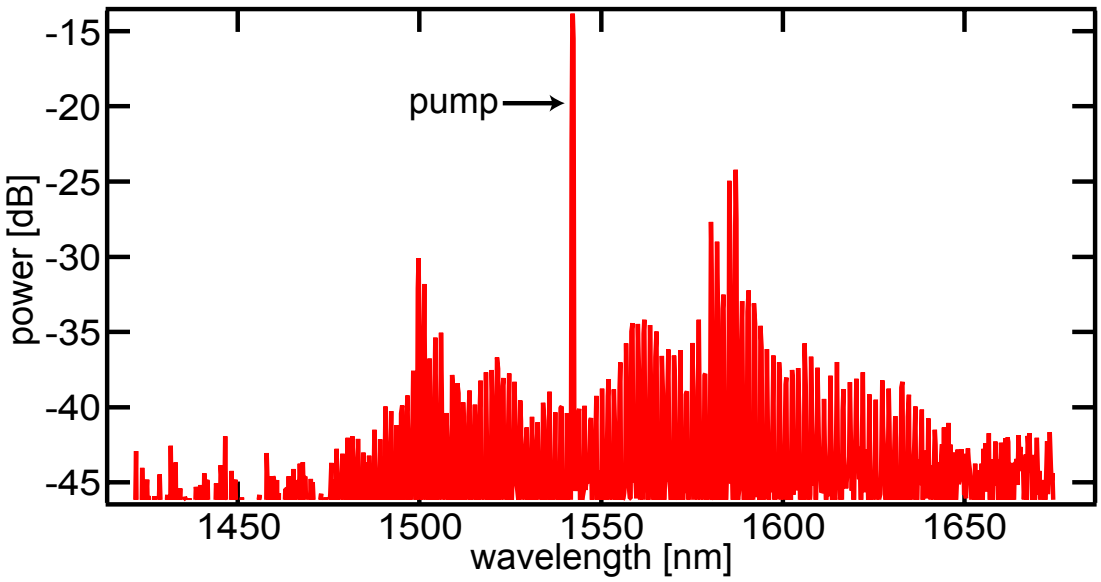

Figure 7.1: **Optical spectrum of the generated frequency comb at the output of the Si_3N_4 waveguide with a pump wavelength of** 1541 nm**.** The comb is in a stable low-noise state with this spectrum and we are able to manipulate and process the generated frequencies when filtering out the pump.

We achieve stable operation of the comb by tuning the pump wavelength to a spectral point in the microring resonance where the comb intensity noise drops. We tune the pump laser into resonance from the "blue-detuned" side to avoid thermal bistability. As we tune into the resonance the RF intensity noise drops by more than 25 dB and measurement of the temporal output suggests the comb is mode-locked [160]. In this low-noise operation state, a stable comb

can be maintained for hours meeting the first condition necessary for an on-chip source.

7.3.1 Experimental Setup

The experimental setup is shown in figure 7.2. The input and output coupling to the chip are the same as described in section 5.4. For the pump input, we use a voltage controlled narrow linewidth source to lock into a cavity resonance. We

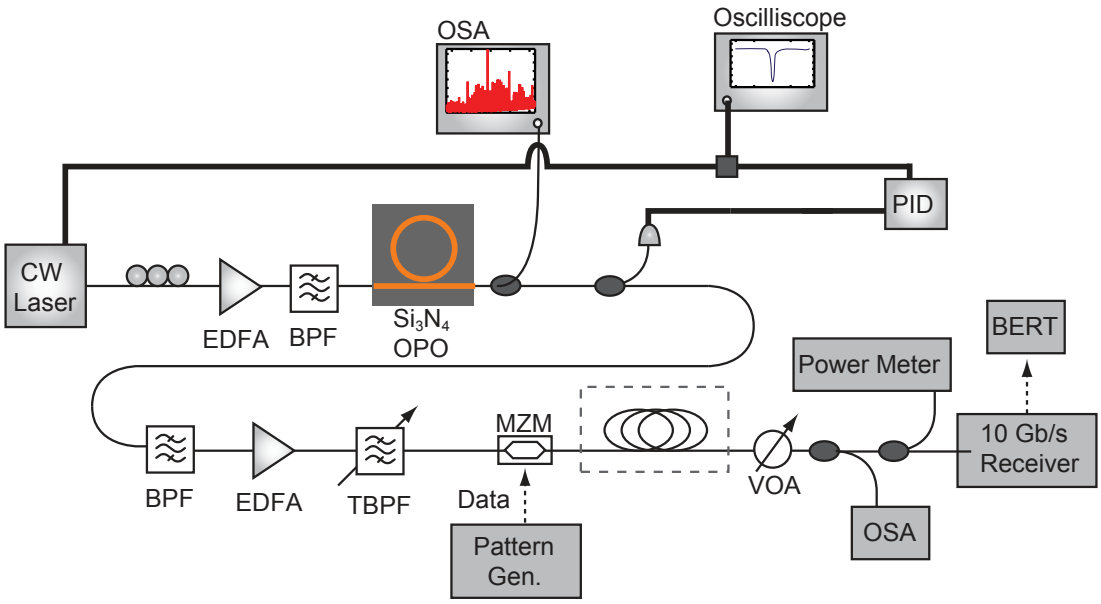

Figure 7.2: **The experimental setup for the BER and eye diagram comb measurements.** The input of the device is an amplified narrow linewidth pump source tuned into the cavity resonance. The output is split three ways. The first is to monitor the cavity resonance and to provide feedback for tuning the pump wavelength. The second monitors the comb spectral output. The third is filtered using a bandpass filter to select comb lines without the pump. These are then amplified and then a narrow filter selects individual lines. The lines are then modulated and sent through a variable optical attenuator to control the received power.

view the cavity lineshape by sweeping the piezo-voltage of the pump laser and viewing the response on an oscilloscope. By turning off the sweep and slowly tuning the voltage, we tune deeper into the resonance. The output is split into three separate fibers. The first provides the feedback needed to control the input wavelength by examining the resonance as described. The second goes to an oscilloscope and monitors the comb spectrum as in figure 7.1. The final is sent through a bandpass filter to isolate a 10 nm spectral range consisting of six newly generated wavelengths. The power at each wavelength coupled from the ring to the bus waveguide is on the order of 1 mW; however, the inefficiency of our off-chip collection and filtering require amplification for further processing. Therefore, we use a low-noise EDFA to increase the power of the filtered comb lines. We then use a 1 nm tunable filter to select individual wavelengths. We modulate the selected wavelength with a lithium niobate Mach-Zehnder modulator driven by a pattern generator to imprint a $2^{31} - 1$ non-return-to-zero psuedo-random bit sequence (PRBS) at a data rate of $10\,\mathrm{Gb\,s^{-1}}$. The modulated signal is then sent to either a sampling oscilloscope to generate eye diagrams or to a variable optical attenuator (VOA), then into a $10\,\mathrm{Gb\,s^{-1}}$ lightwave receiver and a bit-error-rate tester (BERT). For the baseline measurement of our set-up, we modulate a tunable external cavity diode laser, operating at a wavelength near the filtered comb lines.

7.3.2 Bit-Error-Rate Measurements

A common method for measuring the performance of a device or system is to take BER measurements. This is done by counting the number of errors per bit received using an arbitrary data pattern sent through the device under test and

to a comparator. As the noise in the system increases and the signal to noise ratio degrades, the number of measured errors increases dramatically. On the other hand, for very low-noise systems in which few errors occur a BER test must run for thousands of seconds or longer to ensure an accurate measurement.

The BER as a function of received optical power for our device is plotted in Figure 7.3. We observe a negligible power penalty for the tested comb lines as compared to the baseline across a 30 nm span, where power penalty is defined as the difference in received power at a 10^{-9} error rate between the baseline and test data. Additionally, we achieve error-free operation, that is a BER less than 10^{-12}, for the generated wavelengths. Although we expect the BER to be linear with received power, we observe a slight curvature in the data. Since the curvature is the same for the baseline and data measurement we conclude it originates from our test equipment and is not fundamental to the microring wavelength generator. If we examine the measurements for a BER of 10^{-6} or less, we can achieve a good linear fit of the data curves. Additionally, we transmit data from one of the comb lines through a 10 km spool of optical fiber to show suitability for long-haul optical communications. In this case, we incur a very small power-penalty in reference to the same comb line without the added fiber.

7.3.3 Eye Diagrams

Open eye diagrams confirm the low power penalty of the modulated spectral lines. Figure 7.4 shows the eye diagram for each comb line on which we performed BER measurements. As expected, the $10\,\mathrm{Gb\,s^{-1}}$ signal shows up clearly on the oscilloscope with minimal noise and no closing of the pattern eye. We can

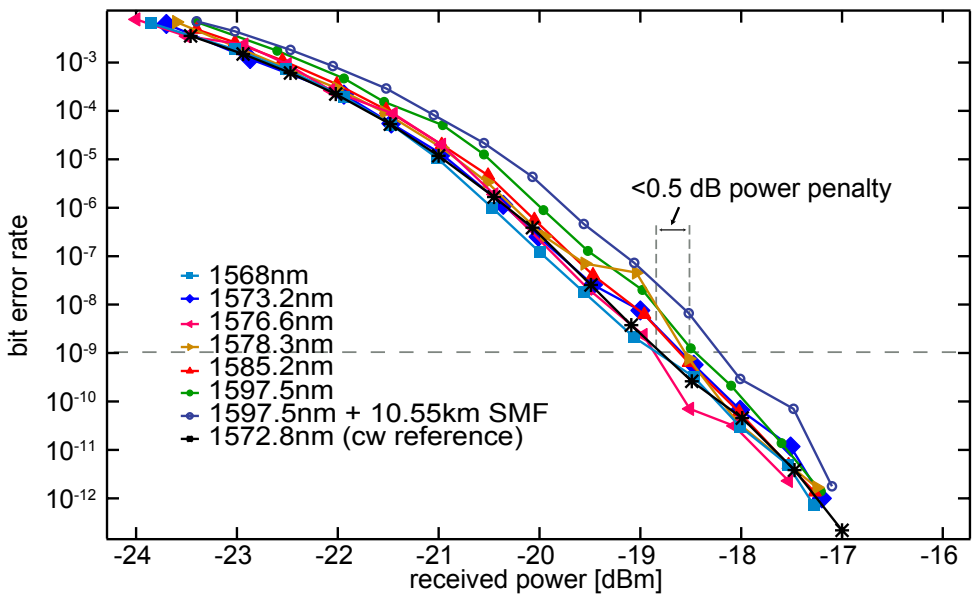

Figure 7.3: **BERT measurements of the filtered comb lines.** The cw reference measurement acts as a back-to-back baseline with which to compare the modulated comb lines. We note error-free operation of the comb lines and a minimal power penalty measured at a bit-error-rate of 10^{-9}

also see the difference the VOA makes in the quality of the received signal. The eye-pattern in figure 7.4d is more closed than the others because it is taken at a weaker adjusted received power. From the BER and clean eye measurements, we can declare the independent filtering and modulation of comb lines without distortion from generated neighbors.

In summary, we characterize the performance of the multiple wavelength source generated from a microring resonator OPO and show that it is suitable for an on-chip optical communications network. The frequency comb used in this experiment had a line spacing of about 200 GHz. As discussed in section 6.4, we can tune this parameter by modifying the resonators radius, which allows for great flexibility in channel spacing and the potential to meet standard WDM specifications. Although in this work filtering and modulation are done

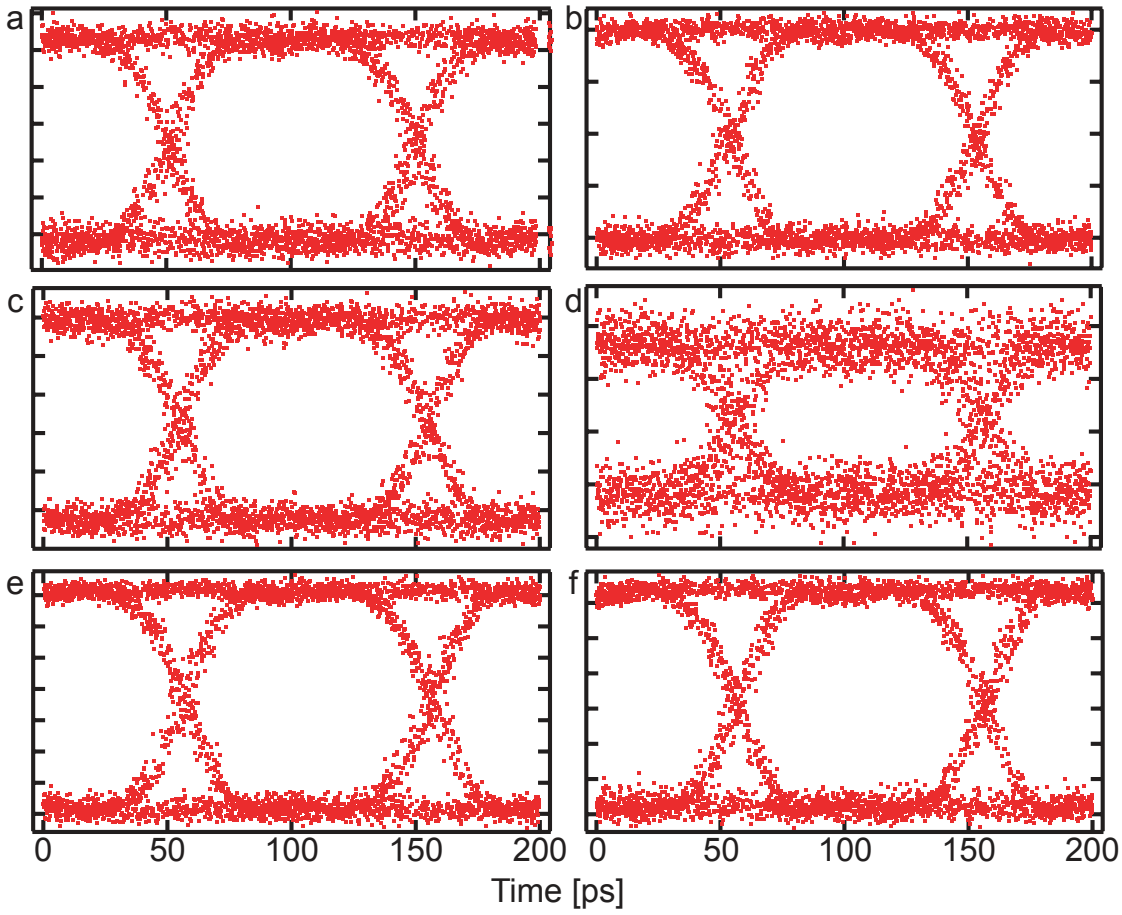

Figure 7.4: **Eye diagrams for the six measured comb lines generated by the microcavity for a.** 1568 nm **b.** 1573.2 nm **c.** 1576.6 nm **d.** 1578.3 nm **e.** 1585.2 nm and **f.** 1597.5 nm. The clean and open eye confirms the BER data showing no power-penalty.

off-chip, through the incorporation of cascaded silicon electro-optic ring resonators [161], the same functionality can be performed on-chip for a completely integrated system. In that case, each silicon ring modulator would be aligned to one of the hundreds of generated wavelengths to enable on-chip data transmission rates of over 1 Tb/s.

CHAPTER 8

HARMONIC GENERATION IN RING RESONATORS

8.1 Introduction

As discussed in chapter 3, the materials used in CMOS-compatible photonics are centrosymmetric and the bulk $\chi^{(2)}$ vanishes leaving the $\chi^{(3)}$ as the lowest order susceptibility. We have discussed already some of the interesting phenomena that arise from the $\chi^{(3)}$ nonlinearity of Si_3N_4. In this chapter, we will examine the topic of harmonic generation. Third harmonic generation (THG) arises from the bulk $\chi^{(3)}$ nonlinearity and with sufficient optical powers and phase-matching should be observable in Si_3N_4. Previous works have shown THG in silicon photonic crystal cavities [162] and silica microtoroids [163]. Although both are nominally on-chip devices, in practice integration is not straightforward for either: the light emitted from the silicon is out of plane and the SiO_2 toroid requires the same specialized coupling set-up as the silica μ-combs described in section 6.4.*

We also examine second harmonic generation (SHG) in Si_3N_4 ring resonators. Here, we induce a $\chi^{(2)}$ response utilizing the interface between two centrosymmetric materials: the Si_3N_4 core and the SiO_2 cladding. The waveguide interface breaks the bulk symmetry and a second-order nonlinear response can arise [165, 166, 167, 168] from the asymmetric dipole potential formed at the surfaces. Previously, detecting the second harmonic wave from a reflected interface has been used for monitoring surface properties [166, 168], even with centrosymmetric materials, however no CMOS-compatible integrated devices have

*Portions of this chapter are reproduced with permission from [164]

shown guided SH. It has been shown that the use of Bragg reflectors to form microcavities which are either singly resonant [169] or doubly resonant [170] can greatly enhance SH conversion efficiencies. More recent work has shown similar results in deposited silicon [171] and even various compositions of silicon-rich silicon nitride films [172, 173, 174]. It has also been suggested that waveguides [175] could be used to enhance surface SHG.

In section 8.2, we describe the device design and physical process for both SHG and THG in Si_3N_4. We describe the CW conversion of the pump to both SH and TH waves in section 8.3. Unlike previous work in the area, we are able to quantify the strength of the nonlinearity and conversion efficiency for the SHG in our device and discuss the calculation of an effective $\chi^{(2)}$ in section 8.4.

8.2 Device Design

8.2.1 Second Harmonic Generation

The nonlinear process of SHG also known as frequency doubling describes the process of a conversion from a pump frequency, ω_p, to the SH frequency, ω_{sh}, such that $\omega_{sh} = 2\omega_p$. We can model the process by using coupled amplitude equations similar to the discussion of FWM in section 5.2, except examining the nonlinear polarization induced by $\chi^{(2)}$. For the case of Si_3N_4 waveguides, where there is no bulk $\chi^{(2)}$, we substitute in an effective susceptibility, $\chi^{(2)}_{\text{eff}}$. We begin our analysis by developing coupled amplitude equations along the lines

of [23, 176]:

$$\frac{dE_p}{dz} = \frac{j\omega_p^2 \chi_{\text{eff}}^{(2)}}{\beta_p c^2} E_{sh} E_p^* e^{-j\Delta\beta z} \tag{8.1a}$$

$$\frac{dE_{sh}}{dz} = \frac{j\omega_{sh}^2 \chi_{\text{eff}}^{(2)}}{2\beta_{sh} c^2} E_p^2 e^{j\Delta\beta z} \tag{8.1b}$$

$$\Delta\beta = 2\beta_p - \beta_{sh} \tag{8.1c}$$

If we consider the undepleted pump condition, we can directly integrate equation 8.1b to obtain an expression for the SH field. Just like the FWM process, the phase-matching plays a critical role in the conversion efficiency. We can expand equation 8.1c to put it in terms of n_{eff} for pump and SH:

$$\Delta\beta = 2\beta_p - \beta_{sh} = \frac{1}{c}\left(2\omega_p n_{eff,p} - \omega_{sh} n_{eff,sh}\right) = \frac{2\omega_p}{c}\left(n_{eff,p} - n_{eff,sh}\right) \tag{8.2}$$

which gives the condition that the n_{eff} for pump and second harmonic must be the same to achieve zero phase mismatch.

Given the material and waveguide dispersion, meeting the condition of equation 8.2 is in general not achievable. A common scheme employs quasi-phase-matching to overcome this limitation in which the crystal axis is inverted in a periodic manner. This has the consequence of alternating the sign of $\chi^{(2)}$ and overcoming a nonzero phase mismatch [177]. Here, we match the effective index for the fundamental mode of the pump to a higher order mode in the visible range. This method has previously been suggested for phase-matched THG in SiO_2, in both microtoroids [163], and microstructured fibers [178, 179]. We use the FEM mode solver discussed in section 2.4.3 to calculate n_{eff} for a range of pump and SH frequencies for a Si_3N_4 waveguide with a 725 by 1500 nm cross-section. Figure 8.1 shows a plot of the effective index against wavelength for the first 8 modes of the waveguide at the SH wavelength and the fundamental TE mode at the pump wavelength. Since the phase-matching condition is

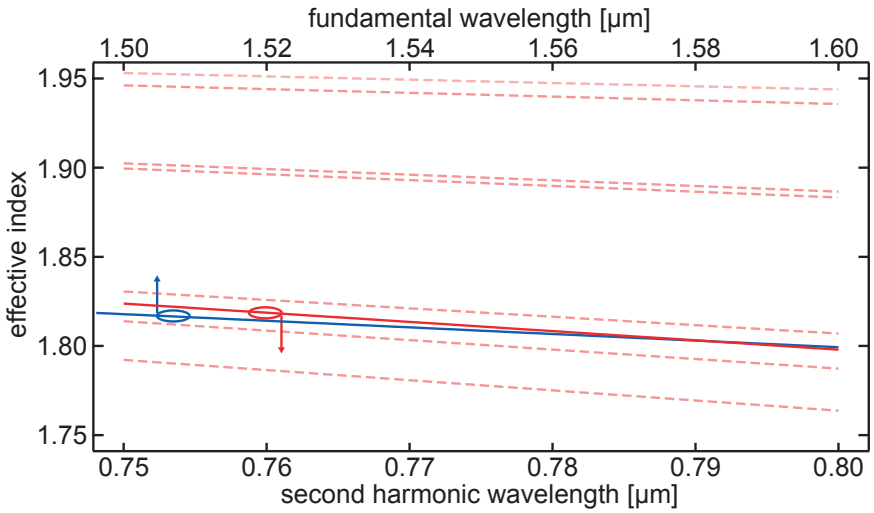

Figure 8.1: **Phase-matching condition for SHG in Si_3N_4 waveguides.** The solid blue line represents the effective index of the fundamental TE mode of the pump. The dashed red lines represent the effective indices for the modes corresponding to the SH wavelengths. The sixth-order mode of the SH (solid red) crosses the blue line indicating a point of perfect phase-matching.

satisfied when the effective index at the pump and corresponding SH wavelengths are equal, crossing points between the blue and red lines are perfectly phase-matched for the corresponding wavelength pair and mode number. As the plot shows, we have a phase-matching point near our experimental pump wavelength with the 6^{th} transverse waveguide mode at the SH wavelength.

8.2.2 Third Harmonic Generation

By using the bulk $\chi^{(3)}$ of Si_3N_4, THG unlike SHG is an expected nonlinear process. Deriving the coupled amplitude equations and phase matching condition is the same as shown in equations 8.1 and 8.2 except $\chi^{(2)}_{\text{eff}}$ is replaced by $\chi^{(3)}$, all "sh" subscripts should be replaced by "th" and E_{th} should be squared in equa-

tion 8.1a, E_p should go to the third power in equation 8.1b and $2\beta_p$ should be $3\beta_p$ for the phase-matching equation. In the end, the phase-matching condition is the same as for SHG: the effective index of the pump and TH wave must be equal. By performing similar simulations as above, we find the fundamental TE mode of the pump is best matched to the 18^{th} order transverse mode at the TH wavelength.

8.3 Experimental Results

In order to increase the efficiency of the harmonic generation we use a ring resonator with a 116 µm radius similar to the devices described in chapter 6. We will first consider the generation and detection of SH light and then examine the behavior of the TH. Interestingly, these processes can occur simultaneously. If we consider the pump to be undepleted the two processes have no effect on each other since they arise from different susceptibilities. However, in the truly coupled amplitude case the problem becomes very complex. Additional complexity is added to the problem when frequency comb generation occurs as well. We will show how comb generation can result in the selective harmonic generation of various comb lines (not the input pump) because of the favorable phase-matching conditions at the generated wavelengths.

8.3.1 Observation of SHG

To measure SHG of a single pump source (no comb generation), a tunable diode laser is amplified using an EDFA and coupled to the waveguide using a tapered

lensed fiber. We use a polarization controller to launch light in the fundamental quasi-TE mode of the waveguide. The pump wavelength, λ_P, is tuned into the resonance of the ring cavity near 1554 nm and, with suitable power levels, we are able to observe generation of the second harmonic. We are able to capture the scattered harmonic light with a top-view color CCD camera. The image in figure 8.2 shows the generated light (strongly enhanced in the ring) coupled to the output waveguide.

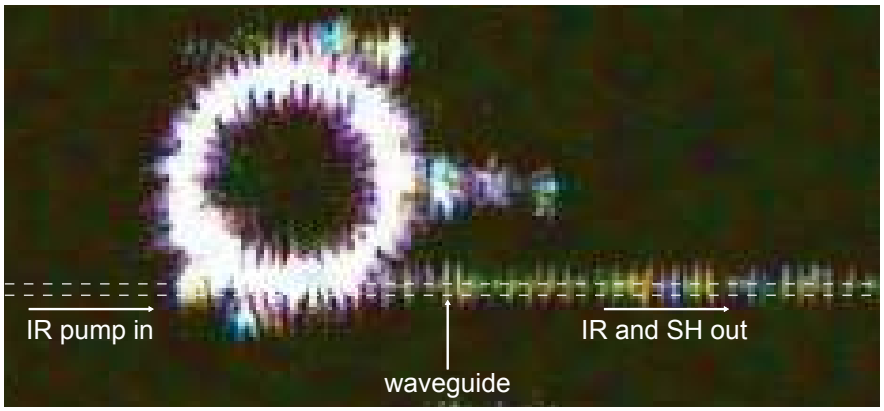

Figure 8.2: **Top view of scattered SH light captured with a color CCD camera.** The input pump comes from the left in this picture and the cavity enhancement of pump power leads to harmonic generation. The light generated in the ring couples out to the bus waveguide.

We use a spectrometer to measure the wavelength of the visible emitted light. After the collection lens at the output of the chip, we place a beam splitter which redirects the generated visible light to the spectrometer. Figure 8.3 displays the output with the generated SH wavelength, λ_{SH}, measured to be 777.1 nm which, as expected, is $\lambda_P/2$. Since only the SH wavelength is detected, we conclude we are not generating broadband photoluminescence which has been previously described in silicon nitride [180, 181]. To measure the power of the SH, both the IR pump and the visible signal are collected into an OSA.

The powers measured by the OSA are corrected to the absolute power values coming out of the waveguide, taking into consideration the coupling efficiencies from the waveguide to the fiber and to the OSA for both pump and SH wavelengths, respectively. The OSA confirms the wavelength measurement for both

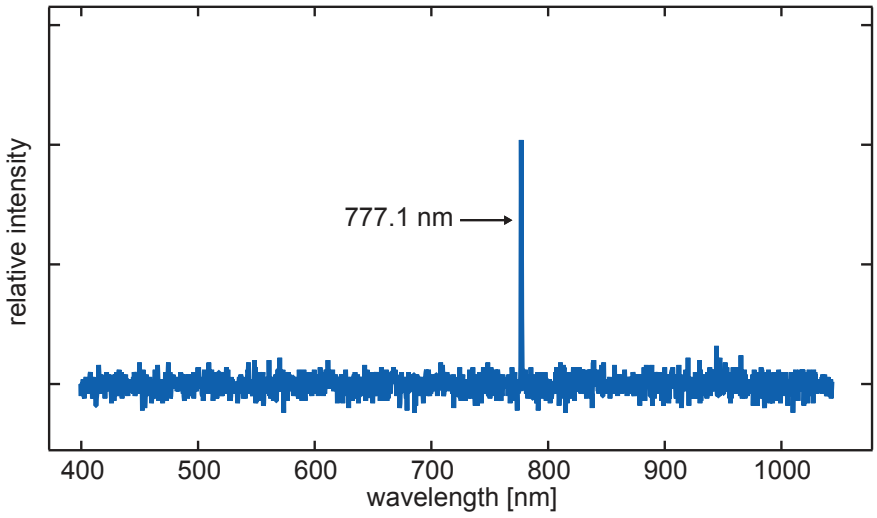

Figure 8.3: **Measurement of the SH wavelength using an optical spectrometer.** The output from the waveguide coupled to a ring resonator pumped at 1554.2 nm shows generation at exactly the expected SH wavelength.

the pump and SH. We observe a maximum conversion efficiency of -35 dB with 100 µW of SH generated for a pump of 315 mW. At increased pump powers, the ring's resonance experiences a severe thermal shift which prevents efficient coupling from the waveguide to the resonator.

8.3.2 Observation of THG

We pump a ring with the same cross section as in the SHG experiment but a smaller radius of 58 µm at a resonance near 1560 nm. For most materials that exhibit SHG, the third harmonic is more difficult to observe due to the relative

strength of the $\chi^{(2)}$ compared to the $\chi^{(3)}$ (as mentioned in section 2.2). However, since the $\chi^{(2)}_{\text{eff}}$ is generated in our case from an interface effect and the $\chi^{(3)}$ is a bulk susceptibility, at the proper phase-matching condition we observe only THG. Additionally, since the TH has a cubic dependence on pump power compared to the square dependence of the SH at larger powers the THG should dominate. As shown in figure 8.4, we generate light at exactly the TH wavelength for our

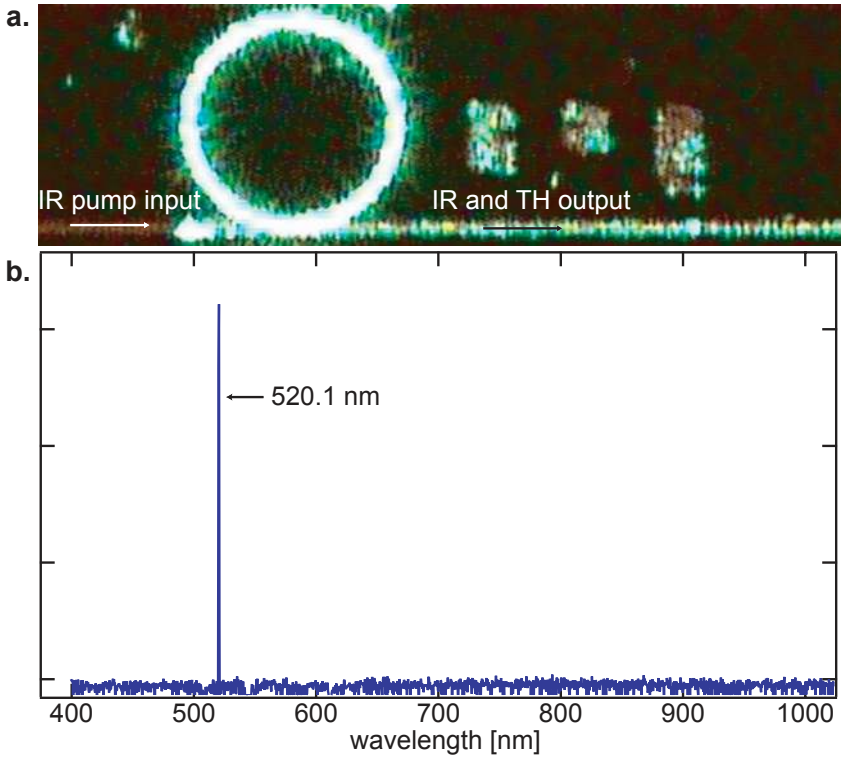

Figure 8.4: **THG in Si_3N_4 ring resonators.** **a.** Top view CCD image of the waveguide coupled ring generating visible TH from an infrared pump. **b.** The spectrometer output from the waveguide shown in **a**. The monochromatic response confirms the wavelength and that THG is occurring.

pump at 520 nm. Unlike the SH, the TH has very poor coupling efficiency to the OSA. However, we can measure the output power using the spectrometer by calibrating the photon count to the integration time. Although this calculation is not precise, it gives a very good idea for the order of magnitude for the TH

generated by our device. With a few hundred mW's of input power we measure pW's with this measurement scheme. This is on the same order as shown in a silicon photonic crystal [162], but here light is coupled and guided in the bus waveguide as opposed to out of plane emission.

8.3.3 Simultaneous Generation of μ-Comb and Harmonics

By pumping the rings at different wavelengths, we observe many interesting phenomena which combine the comb generation from chapter 6 and both SHG and THG. Figure 8.5 shows the spectrum from an OSA and the spectrometer the output of a 116 μm ring with a 730 by 1650 nm cross section when the resonance is pumped at 1542 nm for varying optical powers. Although the pump wave is the strongest in the resonator, because it has poor phase-matching for SHG and THG no harmonics are generated. After oscillation threshold is reached, some of the newly generated modes have enough power and are properly phase-matched for harmonic generation. We can also see that by varying the pump power (and changing the comb shape) different dynamics for harmonic generation, favoring SHG or THG, can be observed.

8.3.4 Modal Profile Image

The captured mode image of the waveguide output (Figure 8.6) corresponds well to the simulated mode profile for the 6^{th} order SH mode which optimizes the phase-matching condition. Since the ring and bus waveguide cross-sections are identical, we expect the same-order mode generated in the ring resonator to

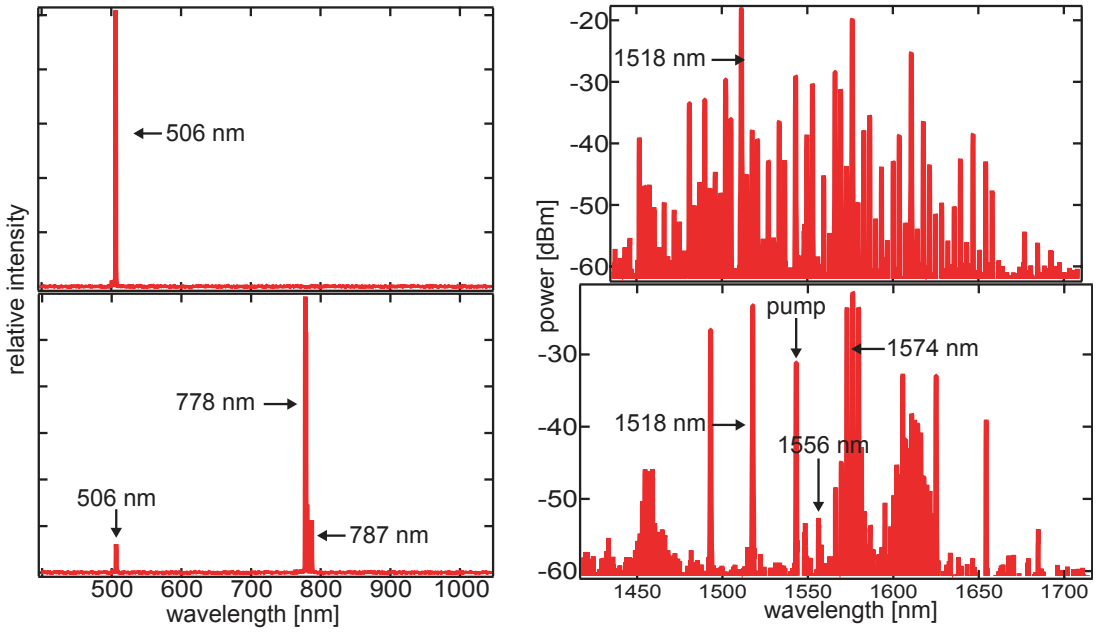

Figure 8.5: **Harmonic generation from generated wavelengths of a Si_3N_4 μ-comb.** The detected visible light from the spectrometer compared to the comb output from the OSA. Although we are pumping at 1542 nm, some of the generated comb lines are better phase-matched and therefore, we see their harmonics instead of the pump's. For different pump powers, we can favor SHG or THG.

couple to the waveguide. Although the point coupling does not guarantee this, because of the large ring radius the effective coupling length is long enough when combined with polarization sensitivity to eliminate other modes. To effectively image the mode, we polish away the nanotapers [182], used to increase coupling efficiency, at the output of the waveguide. We collect the output light with a high NA objective to focus the image on a CCD camera. There are three distinct lobes in the mode showing a good match with the simulated mode.

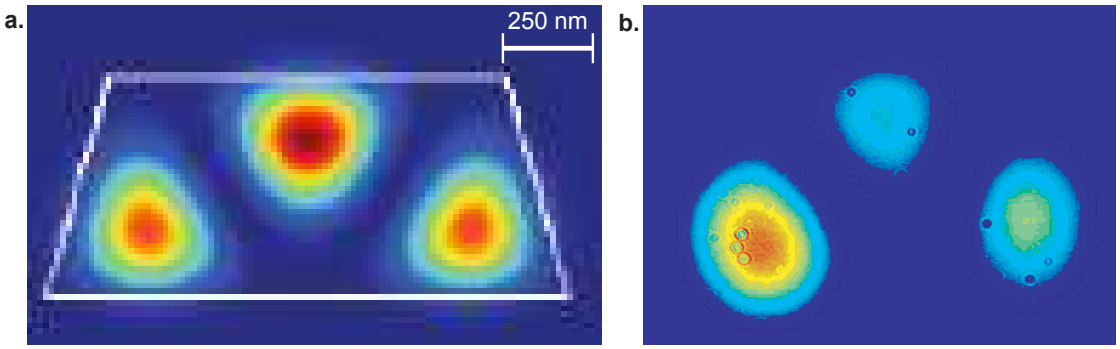

Figure 8.6: **Calculation of mode-order for phase matched SH generation.** **a.** The simulated cross-section mode profile for the sixth-order mode of our waveguide at 777.1 nm. **b.** The captured mode image of the visible emission from our waveguide showing good agreement with the simulated mode profile.

8.4 Analysis and Calculation of $\chi^{(2)}$

We calculate the $\chi^{(2)}_{\text{eff}}$ to be $4 \times 10^{-14}\,\text{m}\,\text{V}^{-1}$ from the conversion efficiency observed in the ring. For SHG with an undepleted pump, the expected signal power may be calculated for a given pump intensity and propagation distance by solving the coupled amplitude equations given by equation 8.1. Since we are using a resonator, the intensity of the pump and SH are increased by the respective cavity enhancement effects of the ring. In order to accurately model the nonlinear susceptibility, we take into account the finesse of the cavity, the simulated modal field overlap and phase-mismatch, and the radius of the ring. The power P_{sh} for second harmonic wave is then given by:

$$P_{sh} = \frac{C_{sh} C_p^2 (\omega_p \chi^{(2)} L P_p)^2}{8 n_p^2 n_{sh} c^3 \epsilon_0 A_p^2} A_{sh} \text{sinc}^2(\Delta\beta L/2) f(A_p, A_{sh}) \tag{8.3a}$$

$$C_i = \frac{P_{circ}}{P_{in}} = \left| \frac{j\kappa_i e^{-\alpha_i L/2}}{e^{j\beta_i L} - \tau_i e^{-\alpha_i L/2}} \right|^2 \tag{8.3b}$$

where n_i is the effective index for the modes, A_i is the mode area, L is the ring circumference and P_p is the pump power dropped to the ring. The modal over-

lap integral between the fundamental and second-harmonic fields is accounted for by the function $f(A_p, A_{sh})$ and is calculated in our case to be very high, 0.83 where the maximum is 1. C_i takes into account the circulating power in the ring [132, 133] where κ and τ represent the coupling parameters from the waveguide to the ring (as described in section 2.6), α_i is the propagation loss in the ring and β_i is the propagation coefficient for the respective waves. We can directly measure C_p from the transmission spectrum of the pump resonance and calculate the value to be approximately 156. For the SH resonance we are unable to directly characterize the intrinsic and coupling Q's due to the difficulty of accessing the higher order transverse mode. Therefore, we estimate that C_{sh} is at most C_p and at least unity. From this approximation we come up with a range of potential values for $\chi^{(2)}_{\text{eff}}$ of 3×10^{-15} to 4×10^{-14} m V^{-1}. We believe the actual enhancement at the SH wavelength to be closer to unity than C_p and $\chi^{(2)}_{\text{eff}}$ to be on the larger side of this range.

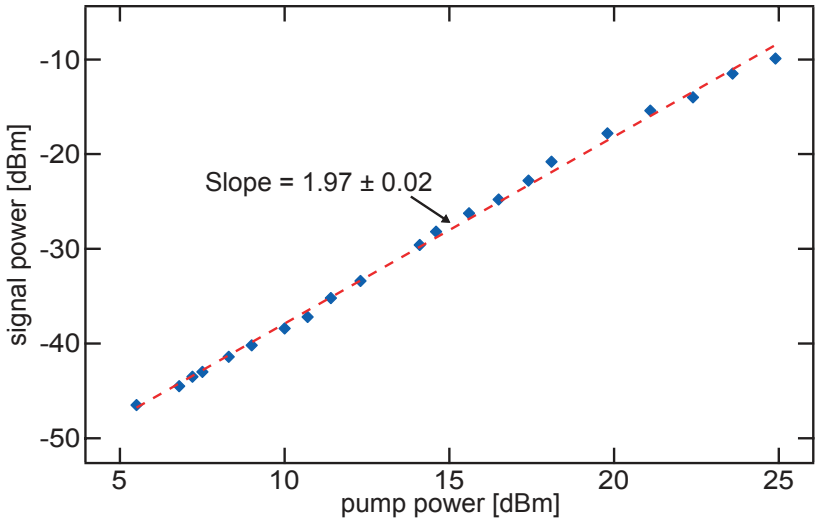

Figure 8.7: **The power output from the generated SH light as a function of input.** The red-dashed line with slope near 2 on the log-log plot represents the best fit line to the data and is very close to the theoretical square prediction.

From equation 8.3a, we see that the SH wave has a quadratic dependence on the pump power. As mentioned earlier, we are able to accurately measure the power at both pump and SH waves using an OSA and calibrating for the different coupling efficiencies. In order to clearly demonstrate the theoretical square dependence of the SH process, we plot the dropped pump power against the generated SH on a log-log scale (figure 8.7) and calculate a best fit slope of 1.9745 ± 0.0225. We note discernible SH in the waveguide coupled to the resonator for input pump powers as low as 1 mW.

The THG efficiencies can be measured and plotted in the same fashion. When measuring the photons detected by the spectrometer for varying pump powers we indeed see the theoretical cubic power dependence. Although the measured powers here are relative, from the estimate given in section 8.3.2 we expect a much stronger conversion efficiency given the circulating pump power and value of $\chi^{(3)}$ measured previously. We believe that imperfect phase-matching and the weak spatial overlap between the fundamental and TH modes may account for the weaker than expected conversion. This also suggests our estimation of $\chi^{(2)}_{\text{eff}}$ may be a lower bound since we assume ideal phase-matching, as suggested by our simulations, for the value given.

Our demonstration of guided on-chip visible light generation opens the available spectrum for Si-based devices from the IR to the visible, increasing bandwidth and enabling potential integration of silicon photo-detectors to on-chip optical networks. Additionally, the doubly resonant SH generation presented here could produce squeezed states [183] of both the pump and SH frequencies for quantum optics studies. Finally, the induced second-order nonlinearity could be used for difference frequency generation to combine two near

infrared pumps to generate a mid-infrared source [184].

CHAPTER 9

SUMMARY AND FUTURE WORK

Integrated optical devices increase the efficiency for a multitude of exciting nonlinear processes with applications from wavelength converters to amplifiers to optical clocks. By developing the silicon nitride platform, we have exploited a broad transparency window, high-index contrast and low loss material to improve the performance for four-wave mixing and harmonic generation devices.

Although the losses and high-Q resonators presented in this dissertation surpass previous efforts in high confinement Si_3N_4 films, there is still room for materials and processing improvement. Roughness and absorption occurring at the waveguide sidewalls is a serious limitation on the process. Recently, very thin (and therefore loosely confined) Si_3N_4 waveguides were developed which minimized the modal overlap with the sidewall for record low-losses [185]. Despite the limitations of these devices, especially for nonlinear interactions, the work exploits a key to overall loss reduction that could be further developed by improving processing of etching and potentially deposition. It should be noted that although we are able to overcome catastrophic film cracking, the stresses on thick films still can form a handful of cracks per wafer which significantly reduce device yields. Even so, the current devices could also be used as the bus waveguide for new three-dimensional designed network architectures [186] because it is deposited and the losses are more than an order of magnitude lower than silicon waveguides.

We decided to examine Si_3N_4 because of its suspected high nonlinear refractive index and negligible nonlinear losses. It should be noted that there are potentially other solutions for achieving these material parameters for

CMOS-compatible nonlinear optics. Recent work using a material named Hydex^{TM} [187], which is essentially a deuterium rich silicon oxynitride, have shown low linear loss and good nonlinear performance [188]. Although this material is proprietary, and therefore not of much use to the scientific community in general, it demonstrates the range of material compositions that can be developed using CMOS CVD processes. A more interesting route might be to explore low-stress nitride (LSN) also known as silicon-rich nitride [189] because the chemical composition has more silicon than stoichiometric Si_3N_4. Although the silicon content of the film may increase the TPA, the material may not support free carriers in which case a stronger n_2 could outweigh the nonlinear losses when compared to Si_3N_4. This material has the added benefit of a slightly larger refractive index and is specifically designed to be stress free so film cracking would not be an issue.

The parametric amplification and efficient wavelength conversion shown here in the quasi-CW regime represent a great improvement over the gain only seen in pulsed pump operation for silicon [19]. The high pump powers could be compensated by increasing the interaction length with reduced losses. The loss values for the waveguides was measured at $0.5\,\mathrm{dB\,cm^{-1}}$ where as the ring resonators show losses as low as $0.1\,\mathrm{dB\,cm^{-1}}$. Of course the longer interaction length reduces the operation bandwidth, but an ideal device could be designed to create an all-optical broadband CW amplifier. Because of the wavelength flexibility of the Si_3N_4 platform, varying designs could lead to different operation windows which are not limited by an energy level material response like most commercially available amplifiers.

Amplifiers based on the Raman effect have been well explored in integrated

silicon waveguides [6, 124, 125, 128, 129]. The Raman effect scatters a small portion of the optical energy of a field to a lower frequency determined strictly by the vibrational modes of the material. Because silicon is crystalline, the bandwidth for Raman gain is very narrow (about 1 nm) and occurs at a well defined frequency shift. Their is a much broader Raman gain bandwidth for silica that has been exploited for amplification in both fibers [190] and microtoroids [191]. This area is one of interest for Si_3N_4 as the effect has not yet been explored and could provide integrated amplifiers (and potentially oscillators) without the need for phase-matching which leads to tight constraints on the waveguide dimensions. Just like the other nonlinear properties we would expect the Raman parameters for Si_3N_4 to lie somewhere between silicon and SiO_2. Therefore, we could have a broader gain bandwidth than silicon and a lower threshold power than SiO_2.

The optical frequency comb has many applications, such as the multiple wavelength source described in chapter 7. The use of a single input laser to generate all the frequencies necessary for an integrated WDM network has major implications for lowering power consumption and potential arrival time of on-chip optical communications. An exciting follow-up work would be full integration of the pump source for the Si_3N_4 resonator on-chip as well, which if it were electrically pumped could eliminate the need for an external laser source that has been a constant energy drag for all-optical communications. Along the same lines, integration of the μ-comb with silicon electro-optic modulators would be an exciting demonstration of the potential for on-chip filtering and modulation in a cross material platform. We have shown preliminary results in this work for moving the comb to a different pump frequency. The growing demand for comb sources in the visible and mid-IR is a potential area of explo-

ration for Si_3N_4 waveguides with differing cross-sections, but potentially on the same chip.

Perhaps most exciting are the applications to fundamental physics of the μ-comb. Continuing along the lines presented with the octave spanning comb, demonstration of $f - 2f$ locking and stabilization would provide a compact source for a range of applications including high-precision spectroscopy, metrology and optical clock sources. The frequency comb temporally generates ultrashort optical pulses with a repetition rate determined by the ring FSR. By using smaller rings and optical rectification, we can perhaps generate radiation in the difficult to reach terahertz regime [192].

We described the surprising second harmonic generation in the Si_3N_4 ring resonators. The generation of a $\chi^{(2)}_{\text{eff}}$ in integrated materials opens up a whole new array of nonlinear optical phenomena. It would be exciting to explore some additional $\chi^{(2)}$ processes in Si_3N_4 such as difference frequency generation to down convert two C-band pump sources. Even more useful could be the Pockels effect which might arise from the induced $\chi^{(2)}$ by applying DC fields across silicon nitride waveguides. It may be necessary to perform a more accurate measurement of $\chi^{(2)}_{\text{eff}}$ than given here which could be done by performing SHG in a long waveguide to more accurately gauge the power and losses in the waveguides at both pump and harmonic wavelengths. Additionally, generation of the fundamental mode at the harmonic wavelength could be achievable by using a quasi-phase-matching scheme as opposed to the high-order mode phase-matching employed here.

Overall, the work presented in this dissertation represents a step forward for the integrated nonlinear photonics community. The exploitation of a new

material system, Si_3N_4, has enabled the demonstration of a new array of functionalities previously unavailable to silicon photonics. It is my hope that this work leads to the development of numerous exciting technologies based on this platform from practical network applications to fundamental physical experimentation.

BIBLIOGRAPHY

[1] Gordon E. Moore. Cramming more components onto integrated circuits. *Electronics*, 38(8):114–117, September 1965.

[2] D.A.B. Miller. Limit to the Bit-Rate Capacity of Electrical Interconnects from the Aspect Ratio of the System Architecture. *Journal of Parallel and Distributed Computing*, 41(1):42–52, February 1997.

[3] Andrew Alduino and Mario Paniccia. Interconnects: Wiring electronics with light. *Nature Photonics*, 1(3):153–155, March 2007.

[4] D.A.B. Miller. Optical interconnects to silicon. *IEEE Journal of Selected Topics in Quantum Electronics*, 6(6):1312–1317, 2000.

[5] Ansheng Liu, Richard Jones, Ling Liao, Dean Samara-Rubio, Doron Rubin, Oded Cohen, Remus Nicolaescu, and Mario Paniccia. A high-speed silicon optical modulator based on a metal-oxide-semiconductor capacitor. *Nature*, 427(6975):615–8, February 2004.

[6] Qianfan Xu, Vilson R. Almeida, and Michal Lipson. Demonstration of high Raman gain in a submicrometer-size silicon-on-insulator waveguide. *Optics Letters*, 30(1):35–7, January 2005.

[7] Qianfan Xu, Sasikanth Manipatruni, Brad Schmidt, Jagat Shakya, and Michal Lipson. 12.5 Gbit/s carrier-injection-based silicon micro-ring silicon modulators. *Optics Express*, 15(2):430–436, January 2007.

[8] Donghwan Ahn, Ching-Yin Hong, Jifeng Liu, Wojciech Giziewicz, Mark Beals, Lionel C. Kimerling, Jurgen Michel, Jian Chen, and Franz X. Kärtner. High performance, waveguide integrated Ge photodetectors. *Optics Express*, 15(7):3916–21, April 2007.

[9] Long Chen, Po Dong, and Michal Lipson. High performance germanium photodetectors integrated on submicron silicon waveguides by low temperature wafer bonding. *Optics Express*, 16(15):11513–8, July 2008.

[10] Solomon Assefa, Fengnian Xia, and Yurii a Vlasov. Reinventing germanium avalanche photodetector for nanophotonic on-chip optical interconnects. *Nature*, 464(7285):80–4, March 2010.

[11] Po Dong, Stefan F. Preble, and Michal Lipson. All-optical compact silicon comb switch. *Optics Express*, 15(15):9600–5, July 2007.

[12] Vilson R. Almeida, Carlos A. Barrios, Roberto R. Panepucci, Michal Lipson, Mark A. Foster, Dimitre G. Ouzounov, and Alexander L. Gaeta. All-optical switching on a silicon chip. *Optics Letters*, 29(24):2867–9, December 2004.

[13] Yurii Vlasov, William M. J. Green, and Fengnian Xia. High-throughput silicon nanophotonic wavelength-insensitive switch for on-chip optical networks. *Nature Photonics*, 2(4):242–246, March 2008.

[14] Fengnian Xia, Mike Rooks, Lidija Sekaric, and Yurii Vlasov. Ultra-compact high order ring resonator filters using submicron silicon photonic wires for on-chip optical interconnects. *Optics Express*, 15(19):11934–41, September 2007.

[15] Linjie Zhou and Andrew W Poon. Electrically reconfigurable silicon microring resonator-based filter with waveguide-coupled feedback. *Optics Express*, 15(15):9194–204, July 2007.

[16] T. H. Maiman. Stimulated Optical Radiation in Ruby. *Nature*, 187:493–494, 1960.

[17] P. A. Franken, A. E. Hill, C. W. Peters, and G. Weinreich. Generation of Optical Harmonics. *Physical Review Letters*, 7(4):118–120, 1961.

[18] C. Koos, P. Vorreau, T. Vallaitis, P. Dumon, W. Bogaerts, R Baets, B Esembeson, I. Biaggio, T. Michinobu, F. Diederich, W. Freude, and J. Leuthold. All-optical high-speed signal processing with siliconorganic hybrid slot waveguides. *Nature Photonics*, 3(4):216–219, March 2009.

[19] Mark A. Foster, Amy C. Turner, Jay E. Sharping, Bradley S. Schmidt, Michal Lipson, and Alexander L. Gaeta. Broad-band optical parametric gain on a silicon photonic chip. *Nature*, 441(7096):960–3, June 2006.

[20] Reza Salem, Mark A. Foster, Amy C. Turner, David F. Geraghty, Michal Lipson, and Alexander L. Gaeta. Signal regeneration using low-power four-wave mixing on silicon chip. *Nature Photonics*, 2(1):35–38, December 2007.

[21] F. Li, M. Pelusi, D-X. Xu, A. Densmore, R. Ma, S. Janz, and D.J. Moss.

Error-free all-optical demultiplexing at 160Gb/s via FWM in a silicon nanowire. *Optics Express*, 18(4):3905, February 2010.

[22] Mark A. Foster, Reza Salem, David F. Geraghty, Amy C. Turner-Foster, Michal Lipson, and Alexander L. Gaeta. Silicon-chip-based ultrafast optical oscilloscope. *Nature*, 456(7218):81–4, November 2008.

[23] Robert W. Boyd. *Nonlinear Optics*. Academic Press, third edition, 2008.

[24] Clifford Pollock and Michal Lipson. *Integrated Photonics*. Kluwer Academic Publishers, Norwell, MA, 2003.

[25] Govind P. Agrawal. *Nonlinear Fiber Optics*. Academic Press, New York, 3 edition, 2001.

[26] John D. Joannopoulos, Steven G. Johnson, Joshua N. Winn, and Robert D. Meade. *Photonic Crystals: Molding the Flow of Light*. Princeton University Press, Princeton, New Jersey, second edi edition, 2008.

[27] Katsunari Okamoto. *Fundamentals of Optical Waveguides*. Academic Press, San Diego, CA, second edi edition, 2006.

[28] E. A. J. Marcatili. Dielectric rectangular waveguide and directional coupler for integrated optics. *Bell Systems Technical Journal*, 48(21):2071–2102, 1969.

[29] R.M. Knox and P.P. Toulios. Integrated Circuits for the Millimeter through Optical Frequency Range. In J. Fox, editor, *MRI symposium on Submillimeter Waves*, page 497, Brooklyn, NY, 1970. Polytechnic Press.

[30] G. B. Hocker and W. K. Burns. Mode dispersion in diffused channel waveguides by the effective index method. *Applied Optics*, 16(1):113–8, January 1977.

[31] Amy C. Turner, Christina Manolatou, Bradley S. Schmidt, Michal Lipson, Mark A. Foster, Jay E. Sharping, and Alexander L. Gaeta. Tailored anomalous group-velocity dispersion in silicon channel waveguides. *Optics Express*, 14(10):4357–62, May 2006.

[32] Feng Luan, Mark D. Pelusi, Michael R. E. Lamont, Duk-Yong Choi, Steve Madden, Barry Luther-Davies, and Benjamin J. Eggleton. Dispersion engineered As_2S_3 planar waveguides for broadband four-wave mix-

ing based wavelength conversion of 40 Gb/s signals. *Optics Express*, 17(5):3514–20, March 2009.

[33] A. Yariv. Universal relations for coupling of optical power between microresonators and dielectric waveguides. *Electronics Letters*, 36(4):321–322, 2000.

[34] A. Yariv. Critical coupling and its control in optical waveguide-ring resonator systems. *IEEE Photonics Technology Letters*, 14(4):483–485, April 2002.

[35] Joyce Poon, Jacob Scheuer, Shayan Mookherjea, George Paloczi, Yanyi Huang, and Amnon Yariv. Matrix analysis of microring coupled-resonator optical waveguides. *Optics Express*, 12(1):90–103, January 2004.

[36] P. Rabiei, W. H. Steier, and L. R. Dalton. Polymer micro-ring filters and modulators. *Journal of Lightwave Technology*, 20(11):1968–1975, November 2002.

[37] Michael Hochberg and Tom Baehr-Jones. Towards fabless silicon photonics. *Nature Photonics*, 4(8):492–494, August 2010.

[38] John E. Cunningham, Ashok V. Krishnamoorthy, Ron Ho, Ivan Shubin, Hiren Thacker, Jon Lexau, Daniel C. Lee, Dazeng Feng, Eugene Chow, Ying Luo, Xuezhe Zheng, Guoliang Li, Jin Yao, Thierry Pinguet, Kannan Raj, Mehdi Asghari, and James G. Mitchell. Integration and Packaging of a Macrochip With Silicon Nanophotonic Links. *IEEE Journal of Selected Topics in Quantum Electronics*, 17(3):546–558, May 2011.

[39] U. Fischer, T. Zinke, J.-R. Kropp, F. Arndt, and K. Petermann. 0.1 dB/cm waveguide losses in single-mode SOI rib waveguides. *IEEE Photonics Technology Letters*, 8(5):647–648, May 1996.

[40] Walid Mathlouthi, Haisheng Rong, and Mario Paniccia. Characterization of efficient wavelength conversion by four-wave mixing in sub-micron silicon waveguides. *Optics express*, 16(21):16735–45, October 2008.

[41] J. Schmidtchen, A. Splett, B. Schuppert, K. Petermann, and G. Burbach. Low loss singlemode optical waveguides with large cross-section in silicon-on-insulator. *Electronics Letters*, 27(16):1486, 1991.

[42] Tai Tsuchizawa, Koji Yamada, Hiroshi Fukuda, Toshifumi Watanabe,

Shingo Uchiyama, and Seiichi Itabashi. Low-Loss Si Wire Waveguides and their Application to Thermooptic Switches. *Japanese Journal of Applied Physics*, 45(No. 8B):6658–6662, August 2006.

[43] P. Dumon, W. Bogaerts, V. Wiaux, J. Wouters, S. Beckx, J. Van Campenhout, D. Taillaert, B. Luyssaert, P. Bienstman, D. Van Thourhout, and R. Baets. Low-Loss SOI Photonic Wires and Ring Resonators Fabricated With Deep UV Lithography. *IEEE Photonics Technology Letters*, 16(5):1328–1330, May 2004.

[44] Fengnian Xia, Lidija Sekaric, and Yurii Vlasov. Ultracompact optical buffers on a silicon chip. *Nature Photonics*, 1(1):65–71, January 2007.

[45] M. Gnan, S. Thoms, D.S. Macintyre, R.M. De La Rue, and M. Sorel. Fabrication of low-loss photonic wires in silicon-on-insulator using hydrogen silsesquioxane electron-beam resist. *Electronics Letters*, 44(2):115, 2008.

[46] Shijun Xiao, Maroof H Khan, Hao Shen, and Minghao Qi. Compact silicon microring resonators with ultra-low propagation loss in the C band. *Optics express*, 15(22):14467–75, October 2007.

[47] Matthew Borselli, Thomas J. Johnson, and Oskar Painter. Beyond the Rayleigh scattering limit in high-Q silicon microdisks: theory and experiment. *Optics Express*, 13(5):1515–30, March 2005.

[48] M. Dinu, F. Quochi, and H. Garcia. Third-order nonlinearities in silicon at telecom wavelengths. *Applied Physics Letters*, 82(18):2954, 2003.

[49] Alan D. Bristow, Nir Rotenberg, and Henry M. van Driel. Two-photon absorption and Kerr coefficients of silicon for 8502200nm. *Applied Physics Letters*, 90(19):191104, 2007.

[50] Amy C. Turner-Foster, Mark A. Foster, Jacob S. Levy, Carl B. Poitras, Reza Salem, Alexander L. Gaeta, and Michal Lipson. Ultrashort free-carrier lifetime in low-loss silicon nanowaveguides. *Optics Express*, 18(4):3582–91, March 2010.

[51] Suresh Sridaran and Sunil A. Bhave. Nanophotonic devices on thin buried oxide Silicon-On-Insulator substrates. *Optics Express*, 18(4):3850–7, February 2010.

[52] Charles W. Holzwarth, Jason S. Orcutt, Miloš A. Popović, Vladimir Sto-

janović, Judy L. Hoyt, Rajeev J. Ram, and Henry I. Smith. Localized substrate removal technique enabling strong-confinement microphotonics in bulk Si CMOS processes. *2008 Conference on Lasers and Electro-Optics*, pages 1–2, May 2008.

[53] Jason S. Orcutt, Anatol Khilo, Charles W. Holzwarth, Miloš A. Popović, Hanqing Li, Jie Sun, Thomas Bonifield, Randy Hollingsworth, Franz X. Kärtner, Henry I. Smith, Vladimir Stojanović, and Rajeev J. Ram. Nanophotonic integration in state-of-the-art CMOS foundries. *Optics Express*, 19(3):2335–46, January 2011.

[54] Nicolás Sherwood-Droz, Alexander Gondarenko, and Michal Lipson. Oxidized silicon-on-insulator (OxSOI) from bulk silicon: a new photonic platform. *Optics Express*, 18(6):5785–90, March 2010.

[55] Ling Liao, Desmond R. Lim, Anuradha M. Agarwal, Xiaoman Duan, Kevin K. Lee, and Lionel C. Kimerling. Optical transmission losses in polycrystalline silicon strip waveguides: Effects of waveguide dimensions, thermal treatment, hydrogen passivation, and wavelength. *Journal of Electronic Materials*, 29(12):1380–1386, December 2000.

[56] Kyle Preston, Bradley Schmidt, and Michal Lipson. Polysilicon photonic resonators for large-scale 3D integration of optical networks. *Optics express*, 15(25):17283–90, December 2007.

[57] A. Harke, M. Krause, and J. Mueller. Low-loss singlemode amorphous silicon waveguides. *Electronics Letters*, 41(25):41–42, 2005.

[58] Karthik Narayanan and Stefan F. Preble. Optical nonlinearities in hydrogenated amorphous silicon waveguides. *Optics Express*, 18(9):8998–9005, April 2010.

[59] Bart Kuyken, Stéphane Clemmen, Shankar Kumar Selvaraja, Wim Bogaerts, Dries Van Thourhout, Philippe Emplit, Serge Massar, Gunther Roelkens, and Roel Baets. On-chip parametric amplification with 26.5 dB gain at telecommunication wavelengths using CMOS-compatible hydrogenated amorphous silicon waveguides. *Optics Letters*, 36(4):552–4, March 2011.

[60] D. W. Vernooy, V. S. Ilchenko, H. Mabuchi, E. W. Streed, and H. J. Kimble. High-Q measurements of fused-silica microspheres in the near infrared. *Optics Letters*, 23(4):247–9, February 1998.

[61] D. K. Armani, T. J. Kippenberg, S. M. Spillane, and K. J. Vahala. Ultra-high-Q toroid microcavity on a chip. *Nature*, 421(6926):925–8, February 2003.

[62] G. Grand, J.P. Jadot, H. Denis, S. Valette, A. Fournier, and A.M. Grouillet. Low-loss PECVD silica channel waveguides for optical communications. *Electronics Letters*, 26(25):2135, 1990.

[63] Christopher Richard Doerr and Katsunari Okamoto. Advances in Silica Planar Lightwave Circuits. *Journal of Lightwave Technology*, 24(12):4763–4789, December 2006.

[64] Richard A. Soref, Stephen J. Emelett, and Walter R. Buchwald. Silicon waveguided components for the long-wave infrared region. *Journal of Optics A: Pure and Applied Optics*, 8(10):840–848, October 2006.

[65] James D. Plummer, Michael D. Deal, and Peter B. Griffin. *Silicon VLSI Technology: Fundamentals, Practice and Modeling*. Prentice Hall, 2000.

[66] Tatsuya Enomoto, Ryo Ando, Hiroshi Morita, and Haruo Nakayama. Thermal Oxidation Rate of a Si_3N_4 Film and Its Masking Effect against Oxidation of Silicon. *Japanese Journal of Applied Physics*, 17(No. 6):1049–1058, June 1978.

[67] E. P. Gusev, H.-C. Lu, E. L. Garfunkel, T. Gustafsson, and M. L. Green. Growth and characterization of ultrathin nitrided silicon oxide films. *IBM Journal of Research and Development*, 43(3):265–286, May 1999.

[68] Frank L Riley. Silicon Nitride and Related Materials. *Journal of the American Ceramic Society*, 83(2):245–265, December 2004.

[69] C. Morosanu. The preparation, characterization and applications of silicon nitride thin films. *Thin Solid Films*, 65(2):171–208, January 1980.

[70] Herbert R. Philipp. Optical Properties of Silicon Nitride. *Journal of The Electrochemical Society*, 120(2):295, February 1973.

[71] K. Worhoff, P. V. Lambeck, and A. Driessen. Design, tolerance analysis, and fabrication of silicon oxynitride based planar optical waveguides for communication devices. *Journal of Lightwave Technology*, 17(8):1401–1407, 1999.

[72] F. Ay and A. Aydinli. Comparative investigation of hydrogen bonding in silicon based PECVD grown dielectrics for optical waveguides. *Optical Materials*, 26(1):33–46, June 2004.

[73] W. Stutius and W. Streifer. Silicon nitride films on silicon for optical waveguides. *Applied Optics*, 16(12):3218–22, December 1977.

[74] S. Sriram, W. D. Partlow, and C. S. Liu. Low-loss optical waveguides using plasma-deposited silicon nitride. *Applied optics*, 22(23):3664–5, December 1983.

[75] C. H. Henry, R. F. Kazarinov, H. J. Lee, K. J. Orlowsky, and L. E. Katz. Low loss Si_3N_4-SiO_2 optical waveguides on Si. *Applied Optics*, 26(13):2621–2624, July 1987.

[76] D.A.P. Bulla, B.-H.V. Borges, M.A. Romero, N.I. Morimoto, and L.G. Neto. Design and fabrication of SiO_2/Si_3N_4 integrated-optics waveguides on silicon substrates. *IEEE Transactions on Microwave Theory and Techniques*, 50(1):9–12, 2002.

[77] M. Melchiorri, N. Daldosso, F. Sbrana, L. Pavesi, G. Pucker, C. Kompocholis, P. Bellutti, and A. Lui. Propagation losses of silicon nitride waveguides in the near-infrared range. *Applied Physics Letters*, 86(12):121111, 2005.

[78] Michael J. Shaw, Junpeng Guo, G. Allen Vawter, Scott Habermehl, and Charles T. Sullivan. Fabrication techniques for low-loss silicon nitride waveguides. In *Proceedings of SPIE*, volume 5720, pages 109–118. SPIE, 2005.

[79] A. Gorin, A. Jaouad, E. Grondin, V. Aimez, and P. Charette. Fabrication of silicon nitride waveguides for visible-light using PECVD: a study of the effect of plasma frequency on optical properties. *Optics Express*, 16(18):13509–16, September 2008.

[80] S. C. Mao, S. H. Tao, Y. L. Xu, X. W. Sun, M. B. Yu, G. Q. Lo, and D. L. Kwong. Low propagation loss SiN optical waveguide prepared by optimal low-hydrogen module. *Optics Express*, 16(25):20809–16, December 2008.

[81] Ehsan Shah Hosseini, Siva Yegnanarayanan, Amir Hossein Atabaki, Mohammad Soltani, and Ali Adibi. High quality planar silicon nitride microdisk resonators for integrated photonics in the visible wavelength range. *Optics Express*, 17(17):14543–51, August 2009.

[82] Paul E. Barclay, Kartik Srinivasan, Oskar Painter, Benjamin Lev, and Hideo Mabuchi. Integration of fiber-coupled high-Q SiN_x microdisks with atom chips. *Applied Physics Letters*, 89(13):131108, 2006.

[83] J. Guo, M. J. Shaw, G. A. Vawter, P. Esherick, G. R. Hadley, and C. T. Sullivan. High-Q integrated on-chip micro-ring resonator. In *The 17th Annual Meeting of the IEEE Lasers and Electro-Optics Society, 2004. LEOS 2004.*, pages 745–746. IEEE, 2004.

[84] J. Bauer. Optical properties, band gap, and surface roughness of Si_3N_4. *Physica Status Solidi (a)*, 39(2):411–418, February 1977.

[85] Tanya M. Monro and Heike Ebendorff-Heidepriem. Progress in Microstructured Optical Fibers. *Annual Review of Materials Research*, 36(1):467–495, August 2006.

[86] Kazuhiro Ikeda, Robert E. Saperstein, Nikola Alic, and Yeshaiahu Fainman. Thermal and Kerr nonlinear properties of plasma-deposited silicon nitride/ silicon dioxide waveguides. *Optics Express*, 16(17):12987–94, August 2008.

[87] D. Southworth, R. Barton, S. Verbridge, B. Ilic, A. Fefferman, H. Craighead, and J. Parpia. Stress and Silicon Nitride: A Crack in the Universal Dissipation of Glasses. *Physical Review Letters*, 102(22):1–4, June 2009.

[88] C. A. Barrios, B. Sánchez, K. B. Gylfason, A. Griol, H. Sohlström, M. Holgado, and R. Casquel. Demonstration of slot-waveguide structures on silicon nitride / silicon oxide platform. *Optics Express*, 15(11):6846–56, May 2007.

[89] Alexander Gondarenko, Jacob S. Levy, and Michal Lipson. High confinement micron-scale silicon nitride high Q ring resonator. *Optics Express*, 17(14):11366–70, July 2009.

[90] Jacob S. Levy, Alexander Gondarenko, Mark A. Foster, Amy C. Turner-Foster, Alexander L. Gaeta, and Michal Lipson. CMOS-compatible multiple-wavelength oscillator for on-chip optical interconnects. *Nature Photonics*, 4(1):37–40, December 2010.

[91] Michael Shearn, Kenneth Diest, Xiankai Sun, Avi Zadok, Harry Atwater, Amnon Yariv, and Axel Scherer. Advanced silicon processing for active planar photonic devices. *Journal of Vacuum Science & Technology B: Microelectronics and Nanometer Structures*, 27(6):3180, 2009.

[92] W. van Gelder and V. E. Hauser. The Etching of Silicon Nitride in Phosphoric Acid with Silicon Dioxide as a Mask. *Journal of The Electrochemical Society*, 114(8):869, 1967.

[93] J. Dulak, B. J. Howard, and C. Steinbruchel. Etch mechanism in the reactive ion etching of silicon nitride. *Journal of Vacuum Science & Technology A: Vacuum, Surfaces, and Films*, 9(3):775, May 1991.

[94] T. C. Mele. Selective and anisotropic reactive ion etch of LPCVD silicon nitride with CHF_3 based gases. *Journal of Vacuum Science & Technology B: Microelectronics and Nanometer Structures*, 2(4):684, 1984.

[95] M. J. Kumar and S. G. Chamberlain. Selective reactive ion etching of PECVD silicon nitride over amorphous silicon in CF_4/H_2 and nitrogen containing CF_4/H_2 plasma gas mixtures. *Solid-State Electronics*, 39(1):33–37, January 1996.

[96] F. R. de Almeida, R. K. Yamamoto, and H. S. Maciel. Reactive ion etching of PECVD silicon nitride in SF_6 plasma. *Journal of Nuclear Materials*, 200(3):371–374, May 1993.

[97] Peter Kaspar, Yogesh Jeyaram, Heinz Jackel, Annette Foelske, Rudiger Kotz, and Sandro Bellini. Silicon nitride hardmask fabrication using a cyclic CHF_3-based reactive ion etching process for vertical profile nanostructures. *Journal of Vacuum Science & Technology B: Microelectronics and Nanometer Structures*, 28(6):1179, 2010.

[98] M. Sheik-Bahae, A.A. Said, T.-H. Wei, D.J. Hagan, and E.W. Van Stryland. Sensitive measurement of optical nonlinearities using a single beam. *IEEE Journal of Quantum Electronics*, 26(4):760–769, April 1990.

[99] P. K. Tien. Light waves in thin films and integrated optics. *Applied optics*, 10(11):2395–413, November 1971.

[100] F. Ladouceur, J. D. Love, and T. J. Senden. Effect of side wall roughness in buried channel waveguides. *IEE Proceedings - Optoelectronics*, 141(4):242–248, 1994.

[101] K. K. Lee, D. R. Lim, L. C. Kimerling, J. Shin, and F. Cerrina. Fabrication of ultralow-loss Si/SiO_2 waveguides by roughness reduction. *Optics Letters*, 26(23):1888–90, December 2001.

[102] T. Baehr-Jones, M. Hochberg, and A. Scherer. Photodetection in silicon beyond the band edge with surface states. *Optics Express*, 16(3):1659–68, February 2008.

[103] Sharee McNab, Nikolaj Moll, and Yurii Vlasov. Ultra-low loss photonic integrated circuit with membrane-type photonic crystal waveguides. *Optics Express*, 11(22):2927–39, November 2003.

[104] G. Tittelbach, B. Richter, and W. Karthe. Comparison of three transmission methods for integrated optical waveguide propagation loss measurement. *Pure and Applied Optics: Journal of the European Optical Society Part A*, 2(6):683–700, November 1993.

[105] Matthew Borselli, Thomas J. Johnson, and Oskar Painter. Accurate measurement of scattering and absorption loss in microphotonic devices. *Optics Letters*, 32(20):2954–6, October 2007.

[106] M. Sheik-Bahae, D. Hagan, and E. Van Stryland. Dispersion and band-gap scaling of the electronic Kerr effect in solids associated with two-photon absorption. *Physical Review Letters*, 65(1):96–99, July 1990.

[107] R. H. Stolen and Chinlon Lin. Self-phase-modulation in silica optical fibers. *Physical Review A*, 17(4):1448–1453, April 1978.

[108] Masaki Asobe, Kenichi Suzuki, Terutoshi Kanamori, and Kenichi Kubodera. Nonlinear refractive index measurement in chalcogenide-glass fibers by self-phase modulation. *Applied Physics Letters*, 60(10):1153, 1992.

[109] Chao-Yi Tai, James Wilkinson, Nicolas Perney, M. Netti, F. Cattaneo, Chris Finlayson, and Jeremy Baumberg. Determination of nonlinear refractive index in a Ta2O5 rib waveguide using self-phase modulation. *Optics Express*, 12(21):5110–6, October 2004.

[110] Eric Dulkeith, Yurii A. Vlasov, Xiaogang Chen, Nicolae C. Panoiu, and Richard M. Osgood. Self-phase-modulation in submicron silicon-on-insulator photonic wires. *Optics Express*, 14(12):5524–34, June 2006.

[111] R. Stolen and J. Bjorkholm. Parametric amplification and frequency conversion in optical fibers. *IEEE Journal of Quantum Electronics*, 18(7):1062–1072, July 1982.

[112] Hiroshi Fukuda, Koji Yamada, Tetsufumi Shoji, Mitsutoshi Takahashi,

Tai Tsuchizawa, Toshifumi Watanabe, Jun-Ichi Takahashi, and Sei-Ichi Itabashi. Four-wave mixing in silicon wire waveguides. *Optics Express*, 13(12):4629–37, June 2005.

[113] Richard L. Espinola, Jerry I. Dadap, Richard M. Osgood, Sharee J. McNab, and Yurii A. Vlasov. C-band wavelength conversion in silicon photonic wire waveguides. *Optics Express*, 13(11):4341–9, May 2005.

[114] Mark A. Foster, Amy C. Turner, Reza Salem, Michal Lipson, and Alexander L. Gaeta. Broad-band continuous-wave parametric wavelength conversion in silicon nanowaveguides. *Optics Express*, 15(20):12949, 2007.

[115] Amy C. Turner-Foster, Mark A. Foster, Reza Salem, Alexander L. Gaeta, and Michal Lipson. Frequency conversion over two-thirds of an octave in silicon nanowaveguides. *Optics Express*, 18(3):1904–8, March 2010.

[116] M. Ferrera, L. Razzari, D. Duchesne, R. Morandotti, Z. Yang, M. Liscidini, J. E. Sipe, S. Chu, B. E. Little, and D. J. Moss. Low-power continuous-wave nonlinear optics in doped silica glass integrated waveguide structures. *Nature Photonics*, 2(12):737–740, November 2008.

[117] Michael R. Lamont, C. M. de Sterke, and Benjamin J. Eggleton. Dispersion engineering of highly nonlinear As_2S_3 waveguides for parametric gain and wavelength conversion. *Optics Express*, 15(15):9458–63, July 2007.

[118] Ying-Hao Kuo, Haisheng Rong, Vanessa Sih, Shengbo Xu, Mario Paniccia, and Oded Cohen. Demonstration of wavelength conversion at 40 Gb/s data rate in silicon waveguides. *Optics Express*, 14(24):11721–6, November 2006.

[119] Benjamin G. Lee, Xiaogang Chen, Aleksandr Biberman, Xiaoping Liu, I-Wei Hsieh, Cheng-Yun Chou, Jerry I. Dadap, Fengnian Xia, William M. J. Green, Lidija Sekaric, Yurii A. Vlasov, Richard M. Osgood, and Keren Bergman. Ultrahigh-Bandwidth Silicon Photonic Nanowire Waveguides for On-Chip Networks. *IEEE Photonics Technology Letters*, 20(6):398–400, 2008.

[120] Yoshitomo Okawachi, Mark A. Foster, Xianpei Chen, Amy C. Turner-Foster, Reza Salem, Michal Lipson, Chris Xu, and Alexander L. Gaeta. Large tunable delays using parametric mixing and phase conjugation in Si nanowaveguides. *Optics Express*, 16(14):10349–57, July 2008.

[121] Jay E. Sharping, Marco Fiorentino, Ayodeji Coker, Prem Kumar, and Robert S. Windeler. Four-wave mixing in microstructure fiber. *Optics letters*, 26(14):1048–50, July 2001.

[122] Jonas Hansryd, Peter A. Andrekson, Mathias Westlund, Jie Li, and Per-Olof Hedekvist. Fiber-based optical parametric amplifiers and their applications. *IEEE Journal of Selected Topics in Quantum Electronics*, 8(3):506–520, May 2002.

[123] Ryan K. W. Lau, Michaël Ménard, Yoshitomo Okawachi, Mark A. Foster, Amy C. Turner-Foster, Reza Salem, Michal Lipson, and Alexander L. Gaeta. Continuous-wave mid-infrared frequency conversion in silicon nanowaveguides. *Optics Letters*, 36(7):1263–5, May 2011.

[124] R. Claps, D. Dimitropoulos, V. Raghunathan, Y. Han, and B. Jalali. Observation of stimulated Raman amplification in silicon waveguides. *Optics Express*, 11(15):1731–9, July 2003.

[125] T. K. Liang and H. K. Tsang. Efficient Raman amplification in silicon-on-insulator waveguides. *Applied Physics Letters*, 85(16):3343, 2004.

[126] L. Pavesi, L. Dal Negro, C. Mazzoleni, G. Franzò, and F. Priolo. Optical gain in silicon nanocrystals. *Nature*, 408(6811):440–4, November 2000.

[127] Sylvain G. Cloutier, Pavel A. Kossyrev, and Jimmy Xu. Optical gain and stimulated emission in periodic nanopatterned crystalline silicon. *Nature Materials*, 4(12):887–91, December 2005.

[128] Ozdal Boyraz and Bahram Jalali. Demonstration of a silicon Raman laser. *Optics Express*, 12(21):5269–73, October 2004.

[129] Haisheng Rong, Ansheng Liu, Richard Jones, Oded Cohen, Dani Hak, Remus Nicolaescu, Alexander Fang, and Mario Paniccia. An all-silicon Raman laser. *Nature*, 433(7023):292–4, January 2005.

[130] Haisheng Rong, Shengbo Xu, Ying-Hao Kuo, Vanessa Sih, Oded Cohen, Omri Raday, and Mario Paniccia. Low-threshold continuous-wave Raman silicon laser. *Nature Photonics*, 1(4):232–237, April 2007.

[131] J. Giordmaine and Robert Miller. Tunable Coherent Parametric Oscillation in $LiNbO_3$ at Optical Frequencies. *Physical Review Letters*, 14(24):973–976, June 1965.

[132] Amy C. Turner, Mark A. Foster, Alexander L. Gaeta, and Michal Lipson. Ultra-low power parametric frequency conversion in a silicon microring resonator. *Optics Express*, 16(7):4881–7, March 2008.

[133] P. P. Absil, J. V. Hryniewicz, B. E. Little, P. S. Cho, R. A. Wilson, L. G. Joneckis, and P. T. Ho. Wavelength conversion in GaAs micro-ring resonators. *Optics Letters*, 25(8):554–6, April 2000.

[134] Anatoliy A. Savchenkov, Andrey B. Matsko, Dmitry Strekalov, Makan Mohageg, Vladimir S. Ilchenko, and Lute Maleki. Low Threshold Optical Oscillations in a Whispering Gallery Mode CaF_2 Resonator. *Physical Review Letters*, 93(24):2–5, December 2004.

[135] T. J. Kippenberg, S. M. Spillane, and K. J. Vahala. Kerr-Nonlinearity Optical Parametric Oscillation in an Ultrahigh-Q Toroid Microcavity. *Physical Review Letters*, 93(8):18–21, August 2004.

[136] Imad H. Agha, Yoshitomo Okawachi, Mark A. Foster, Jay E. Sharping, and Alexander L. Gaeta. Four-wave-mixing parametric oscillations in dispersion-compensated high-Q silica microspheres. *Physical Review A*, 76(4):1–4, October 2007.

[137] Ivan S. Grudinin, Nan Yu, and Lute Maleki. Generation of optical frequency combs with a CaF_2 resonator. *Optics Letters*, 34(7):878, March 2009.

[138] P. Del'Haye, O. Arcizet, A. Schliesser, R. Holzwarth, and T. J. Kippenberg. Full Stabilization of a Microresonator-Based Optical Frequency Comb. *Physical Review Letters*, 101(5):1–4, July 2008.

[139] Jay Sharping, Jun Chen, Xiaoying Li, Prem Kumar, and Robert Windeler. Quantum-correlated twin photons from microstructure fiber. *Optics Express*, 12(14):3086–94, July 2004.

[140] Steven Cundiff and Jun Ye. Colloquium: Femtosecond optical frequency combs. *Reviews of Modern Physics*, 75(1):325–342, March 2003.

[141] Th. Udem, R. Holzwarth, and T. W. Hänsch. Optical frequency metrology. *Nature*, 416(6877):233–7, March 2002.

[142] S. A. Diddams, T. Udem, J. C. Bergquist, E. A. Curtis, R. E. Drullinger, L. Hollberg, W. M. Itano, W. D. Lee, C. W. Oates, K. R. Vogel, and D. J.

Wineland. An optical clock based on a single trapped 199Hg+ ion. *Science*, 293(5531):825–8, August 2001.

[143] Tilo Steinmetz, Tobias Wilken, Constanza Araujo-Hauck, Ronald Holzwarth, Theodor W Hänsch, Luca Pasquini, Antonio Manescau, Sandro D'Odorico, Michael T Murphy, Thomas Kentischer, Wolfgang Schmidt, and Thomas Udem. Laser frequency combs for astronomical observations. *Science*, 321(5894):1335–7, September 2008.

[144] Zhi Jiang, Chen-Bin Huang, Daniel E. Leaird, and Andrew M. Weiner. Optical arbitrary waveform processing of more than 100 spectral comb lines. *Nature Photonics*, 1(8):463–467, August 2007.

[145] T. J. Kippenberg, R. Holzwarth, and S. A. Diddams. Microresonator-Based Optical Frequency Combs. *Science*, 332(6029):555–559, April 2011.

[146] P. Del'Haye, A. Schliesser, O. Arcizet, T. Wilken, R. Holzwarth, and T. J. Kippenberg. Optical frequency comb generation from a monolithic microresonator. *Nature*, 450(7173):1214–7, December 2007.

[147] Anatoliy A. Savchenkov, Andrey B. Matsko, Vladimir S. Ilchenko, Iouri Solomatine, David Seidel, and Lute Maleki. Tunable Optical Frequency Comb with a Crystalline Whispering Gallery Mode Resonator. *Physical Review Letters*, 101(9):1–4, August 2008.

[148] Mark A. Foster, Jacob S. Levy, Onur Kuzucu, Kasturi Saha, Michal Lipson, and Alexander L. Gaeta. Silicon-based monolithic optical frequency comb source. *Optics Express*, 19(15):14233–39, July 2011.

[149] David J. Jones, Scott A. Diddams, Jinendra K. Ranka, Andrew Stentz, Robert S. Windeler, John Hall, and Steven T. Cundiff. Carrier-Envelope Phase Control of Femtosecond Mode-Locked Lasers and Direct Optical Frequency Synthesis. *Science*, 288(5466):635–639, April 2000.

[150] P. Del'Haye, T. Herr, E. Gavartin, R. Holzwarth, and T. J. Kippenberg. Octave Spanning Frequency Comb on a Chip. *arXiv:0912.4890*, 0912.4890, December 2009.

[151] Yoshitomo Okawachi, Kasturi Saha, Jacob S. Levy, Y. Henry Wen, Michal Lipson, and Alexander L. Gaeta. Octave-spanning frequency comb generation in a silicon nitride chip. *arXiv:1107.5555v1*, July 2011.

[152] A. A. Savchenkov, A. B. Matsko, W. Liang, V. S. Ilchenko, D. Seidel, and L. Maleki. Kerr combs with selectable central frequency. *Nature Photonics*, 5(5):293–296, April 2011.

[153] Miloš A. Popović, Tymon Barwicz, Michael R. Watts, Peter T. Rakich, Luciano Socci, Erich P. Ippen, Franz X. Kärtner, and Henry I. Smith. Multistage high-order microring-resonator add-drop filters. *Optics Letters*, 31(17):2571, May 2006.

[154] C. Li, X. Luo, and A. W. Poon. Dual-microring-resonator electro-optic logic switches on a silicon chip. *Semiconductor Science and Technology*, 23(6):064010, June 2008.

[155] J. Van Campenhout, P. Rojo Romeo, P. Regreny, C. Seassal, D. Van Thourhout, S. Verstuyft, L. Di Cioccio, J-M. Fedeli, C. Lagahe, and R. Baets. Electrically pumped InP-based microdisk lasers integrated with a nanophotonic silicon-on-insulator waveguide circuit. *Optics Express*, 15(11):6744–9, May 2007.

[156] Alexander W. Fang, Hyundai Park, Oded Cohen, Richard Jones, Mario Paniccia, and John E. Bowers. Electrically pumped hybrid AlGaInAs-silicon evanescent laser. *Optics Express*, 14(20):9203–10, October 2006.

[157] A. Joshi, B. Kim, and V. Stojanovic. Designing Energy-Efficient Low-Diameter On-Chip Networks with Equalized Interconnects. In *2009 17th IEEE Symposium on High Performance Interconnects*, pages 3–12. IEEE, August 2009.

[158] Haisheng Rong, Shengbo Xu, Oded Cohen, Omri Raday, Mindy Lee, Vanessa Sih, and Mario Paniccia. A cascaded silicon Raman laser. *Nature Photonics*, 2(3):170–174, February 2008.

[159] Jacob S. Levy, Kasturi Saha, Yoshitomo Okawachi, Mark A. Foster, Alexander L. Gaeta, and Michal Lipson. High-performance silicon-based multiple wavelength source. *Optics Letters*, ((accepted)), 2011.

[160] Mark A. Foster, Jacob S. Levy, Onur Kuzucu, Kasturi Saha, Michal Lipson, and Alexander L. Gaeta. A Silicon-Based Monolithic Optical Frequency Comb Source. *arXiv:1102.0326v1*, February 2011.

[161] Sasikanth Manipatruni, Long Chen, and Michal Lipson. Ultra high bandwidth WDM using silicon microring modulators. *Optics Express*, 18(16):16858–67, August 2010.

[162] B. Corcoran, C. Monat, C. Grillet, D. J. Moss, B. J. Eggleton, T. P. White, L. O'Faolain, and T. F. Krauss. Green light emission in silicon through slow-light enhanced third-harmonic generation in photonic-crystal waveguides. *Nature Photonics*, 3(4):206–210, March 2009.

[163] Tal Carmon and Kerry J. Vahala. Visible continuous emission from a silica microphotonic device by third-harmonic generation. *Nature Physics*, 3(6):430–435, May 2007.

[164] Jacob S. Levy, Mark A. Foster, Alexander L. Gaeta, and Michal Lipson. Harmonic generation in silicon nitride ring resonators. *Optics Express*, 19(12):11415–11421, May 2011.

[165] N. Bloembergen, R. Chang, S. Jha, and C. Lee. Optical Second-Harmonic Generation in Reflection from Media with Inversion Symmetry. *Physical Review*, 174(3):813–822, October 1968.

[166] H. W. K. Tom, T. F. Heinz, and Y. R. Shen. Second-Harmonic Reflection from Silicon Surfaces and Its Relation to Structural Symmetry. *Physical Review Letters*, 51(21):1983–1986, November 1983.

[167] J. E. Sipe, D. J. Moss, and H. M. van Driel. Phenomenological theory of optical second- and third-harmonic generation from cubic centrosymmetric crystals. *Physical Review B*, 35(3):1129–1141, January 1987.

[168] Y. R. Shen. Surface properties probed by second-harmonic and sum-frequency generation. *Nature*, 337(6207):519–525, February 1989.

[169] S. Nakagawa, N. Yamada, N. Mikoshiba, and D. E. Mars. Second-harmonic generation from GaAs/AlAs vertical cavity. *Applied Physics Letters*, 66(17):2159, 1995.

[170] H. Cao, D. B. Hall, J. M. Torkelson, and C.-Q. Cao. Large enhancement of second harmonic generation in polymer films by microcavities. *Applied Physics Letters*, 76(5):538, 2000.

[171] D. Gusev, I. Soboleva, M. Martemyanov, T. Dolgova, a. Fedyanin, and O. Aktsipetrov. Enhanced second-harmonic generation in coupled microcavities based on all-silicon photonic crystals. *Physical Review B*, 68(23):1–4, December 2003.

[172] S. Lettieri, S. Di Finizio, P. Maddalena, V. Ballarini, and F. Giorgis. Second-

harmonic generation in amorphous silicon nitride microcavities. *Applied Physics Letters*, 81(25):4706, 2002.

[173] F. Gesuele, S. Lettieri, P. Maddalena, C. Ricciardi, V. Ballarini, and F. Giorgis. Optical harmonic generation in amorphous silicon nitride microcavities. *Journal of Luminescence*, 121(2):274–277, December 2006.

[174] S. Lettieri, F. Gesuele, P. Maddalena, M. Liscidini, L. C. Andreani, C. Ricciardi, V. Ballarini, and F. Giorgis. Second-harmonic generation in hydrogenated amorphous-$Si_{1x}N_x$ doubly resonant microcavities with periodic dielectric mirrors. *Applied Physics Letters*, 87(19):191110, 2005.

[175] Hermann A. Haus and G. A. Reider. Enhancement of surface second harmonic generation with waveguides. *Applied Optics*, 26(21):4576–4580, 1987.

[176] J. Armstrong, N. Bloembergen, J. Ducuing, and P. Pershan. Interactions between Light Waves in a Nonlinear Dielectric. *Physical Review*, 127(6):1918–1939, September 1962.

[177] Martin M. Fejer, G. A. Magel, Dieter H. Jundt, and Robert L. Byer. Quasi-phase-matched second harmonic generation: tuning and tolerances. *IEEE Journal of Quantum Electronics*, 28(11):2631–2654, 1992.

[178] Jinendra K. Ranka, Robert S. Windeler, and Andrew J. Stentz. Optical properties of high-delta air silica microstructure optical fibers. *Optics Letters*, 25(11):796–8, July 2000.

[179] Fiorenzo G. Omenetto, Antoinette J. Taylor, Mark D. Moores, Jesus Arriaga, Jonathan C. Knight, William J. Wadsworth, and Philip St. J. Russell. Simultaneous generation of spectrally distinct third harmonics in a photonic crystal fiber. *Optics Letters*, 26(15):1158, August 2001.

[180] Michael Barth, Nils Nusse, Johannes Stingl, Bernd Lochel, and Oliver Benson. Emission properties of high-Q silicon nitride photonic crystal heterostructure cavities. *Applied Physics Letters*, 93(2):021112, 2008.

[181] Ali Serpenguzel and Selim Tanriseven. Controlled photoluminescence in amorphous-silicon-nitride microcavities. *Applied Physics Letters*, 78(10):1388, 2001.

[182] Vilson R. Almeida, Roberto R. Panepucci, and Michal Lipson. Nanotaper for compact mode conversion. *Optics Letters*, 28(15):1302–4, August 2003.

[183] S. Pereira, Min Xiao, H. Kimble, and J. Hall. Generation of squeezed light by intracavity frequency doubling. *Physical Review A*, 38(9):4931–4934, November 1988.

[184] Nick K. Hon, Kevin K. Tsia, Daniel R. Solli, and Bahram Jalali. Periodically poled silicon. *Applied Physics Letters*, 94(9):091116, 2009.

[185] Jared F. Bauters, Martijn J. R. Heck, Demis John, Daoxin Dai, Ming-chun Tien, Jonathon S. Barton, Arne Leinse, René G. Heideman, Daniel J. Blumenthal, and John E. Bowers. Ultra-low-loss high-aspect-ratio Si_3N_4 waveguides. *Optics Express*, 19(4):3163, February 2011.

[186] Aleksandr Biberman, Kyle Preston, Gilbert Hendry, Nicolás Sherwood-Droz, Johnnie Chan, Jacob S. Levy, Michal Lipson, and Keren Bergman. Photonic network-on-chip architectures using multilayer deposited silicon materials for high-performance chip multiprocessors. *ACM Journal on Emerging Technologies in Computing Systems*, 7(2):1–25, June 2011.

[187] B. E. Little. A VLSI Photonics Platform. In *Optical Fiber Communications Conference, 2003. OFC 2003*, volume 2, pages 444–445 vol. 2, 2003.

[188] L. Razzari, D. Duchesne, M. Ferrera, R. Morandotti, S. Chu, B. E. Little, and D. J. Moss. CMOS-compatible integrated optical hyper-parametric oscillator. *Nature Photonics*, 4(1):41–45, December 2010.

[189] H.T. Philipp, W. Svendsen, K.N. Andersen, J. Hubner, and J. Hedegaard Povlsen. Measurement of optical nonlinearity in silicon rich nitride waveguide ring resonators. *Electronics Letters*, 39(16):1184, 2003.

[190] R. H. Stolen. Raman gain in glass optical waveguides. *Applied Physics Letters*, 22(6):276, 1973.

[191] T. J. Kippenberg, S. M. Spillane, D. K. Armani, and K. J. Vahala. Ultralow-threshold microcavity Raman laser on a microelectronic chip. *Optics letters*, 29(11):1224–6, June 2004.

[192] Masayoshi Tonouchi. Cutting-edge terahertz technology. *Nature Photonics*, 1(2):97–105, February 2007.